

**Ultrathin Porous Nanocrystalline Silicon
Membrane for Electrical Sensing and Nanofluidics**

by

Maryna N. Kavalenka

Submitted in Partial Fulfillment

of the

Requirements for the Degree

Doctor of Philosophy

Supervised by

Professor Philippe M. Fauchet

Department of Electrical and Computer Engineering

Arts, Sciences and Engineering

Edmund J. Hajim School of Engineering and Applied Sciences

University of Rochester

Rochester, New York

2012

Dedication

This work is dedicated to my parents, Nikolay and Ekaterina Kavalenka, my sister Alena Matsuik, and my husband Kyle Richardson.

Curriculum Vitae

The author was born in Dudichi, Kalinkovichi Region in Belarus. She received a Bachelor of Science degree in Microelectronic Engineering from Belarusian State University of Informatics and Radioelectronics, Minks, Belarus in 2005, and a Master of Science degree in Electrical and Computer Engineering from the University of Rochester, Rochester, New York in 2007. At the University of Rochester, she pursued research in silicon membrane technology and its applications in electrical sensing and nanofluidics under the guidance of Professor Philippe M. Fauchet.

Publications and Presentations

M. N. Kavalenka, C. C. Striemer, D. Z. Fang, T. R. Gaborski, J. L. McGrath and P. M. Fauchet, "Ballistic and Non-ballistic Gas Flow through Ultrathin Nanopores", *Nanotechnology*, **23**, 145706, 2012

M. N. Kavalenka, C. C. Striemer, J.-P. S. DesOrmeaux, D. Z. Fang, J. L. McGrath and P. M. Fauchet, "Chemical capacitive sensing using ultrathin flexible nanoporous electrodes", *Sens. Actuators, B: Chemical*, **162**, 22, 2012

M. N. Kavalenka, D. Z. Fang, C. C. Striemer, J. L. McGrath and P. M. Fauchet, "Hybrid Polymer/Ultrathin Porous Nanocrystalline Silicon Membranes System for Flow-through Chemical Vapor and Gas Detection", *MRS Proceedings*, 1190-NN12-03, 2009

M. N. Kavalenka, D. Unuchek, A. Leshok and S. Lazarouk, "Computation of Impact Ionization Coefficients of Charge Carriers in Avalanche Light-Emitting Diodes Based on Porous Silicon", *Proceedings of school-conference for young scientists: Problems of modern physics*, National Academy of Sciences of Belarus, Minsk, 2004 (in Russian)

K. Shome, **M. N. Kavalenka**, D. Z. Fang, and P. M. Fauchet, "Metallized Ultrathin Porous Silicon Membranes for Biological Sensing Using SERS", *Frontiers in Pathogen Detection: from Nanosensors to Systems*, *SPIE*, 7553, 75530F-9, 2010

M. N. Kavalenka, C. C. Striemer, J.-P. S. DesOrmeaux, J. L. McGrath and P. M. Fauchet, "Ultrathin Porous Nanocrystalline Silicon Membrane in Sensor Applications", CEIS Technology Showcase, Rochester, NY, 2011

M. N. Kavalenka, C. C. Striemer, D. Z. Fang, J. L. McGrath and P. M. Fauchet, "Experimental Study of Molecule-Pore Wall Collisions in Carbonized Ultrathin Porous Membranes", MRS Fall, Boston, MA, 2010

M. N. Kavalenka, D. Z. Fang, C. C. Striemer, J. L. McGrath and P. M. Fauchet, "Hybrid Polymer/Ultrathin Porous Nanocrystalline Silicon Membrane for Chemical Vapor and Gas Sensing", North American Membrane Society, Charleston, SC, 2009

M. N. Kavalenka, D. Z. Fang, C. C. Striemer, J. L. McGrath and P. M. Fauchet, "Hybrid Polymer/Ultrathin Porous Nanocrystalline Silicon Membranes System for Flow-through Chemical Vapor and Gas Detection", MRS Spring, San Francisco, CA, 2009

M. N. Kavalenka, D. Z. Fang, J.-P. DesOrmeaux, C. C. Striemer, J. L. McGrath and P. M. Fauchet, "Porous Nanocrystalline Silicon Membranes for Vapor Detection Sensor and Other Applications", EDS IEEE, Rochester, NY, 2009

M. N. Kavalenka, C. C. Striemer, D. Z. Fang, J. L. McGrath and P. M. Fauchet, "Air Permeability of Ultrathin Porous Nanocrystalline Silicon Membranes", Gordon Research Conference "Membranes: Materials and Processes", New London, NH, 2008

Acknowledgments

I would like to thank my advisor, Prof. Philippe Fauchet, for all of his guidance, encouragement, patience and expertise. His influence is apparent throughout the thesis, and without him the project would not have been possible. Special thanks also to Prof. James McGrath, who was instrumental in shaping many key ideas in the thesis and provided invaluable expertise and support. I am also indebted to Dr. Christopher Striemer for his assistance at various critical stages in the project and for many helpful discussions. I also want to thank the other members of my proposal and defense committee, Prof. Mark Bocko, Prof. Thomas Jones and Prof. Eldred Chimowitz, all of whom provided much needed criticism and commentary that helped to improve the thesis. Thanks to my colleagues in the Fauchet Research Group (past and present) for their companionship and help during rough points in my research: Krishanu Shome, Josh Winans, Sean Anderson, Adam Heiniger, Mikhail Haurylau, David Fang, Jeffrey Clarkson, Mindy Lee, Han Yoo, Huimin Ouyang, Hui Chen, Jidong Zhang, Wei Sun, Elisa Guillermain, Sudeshna Pal, Halina Krzyzanowska,

Jonathan Lee, Yujing Fu, Shih Kai Ni, Chengzhu Qi. Most of the work was done while I was a member of the Nanomembrane Research Group and in collaboration with SiMPore Inc, and I want to thank especially Jessica Synder, Jon-Paul DesOrmeaux, Nakul Nataraj and Thomas Gaborski for their help and support. None of this work would have been possible without the efforts of Vicki Heberling, Brian McIntyre, Barbara Dick and the staff of the University of Rochester.

I thank all my wonderful friends in Rochester and elsewhere. Most importantly, I want to thank my parents, Nikolay and Ekaterina Kavalenka, my sister, Alena Matsiuk, and my husband, Kyle Richardson, for their love and unconditional support.

Abstract

Membranes made of an ultrathin porous nanocrystalline silicon (pnc-Si) film are well suited for many applications due to their key attributes, including thinness (15-30 nm), pore diameters (5-80 nm) and porosity (0.5-15 %). This thesis is an investigation into the unique properties of pnc-Si material in the context of gas transport, sensing and nanofluidics. The first part of the thesis investigates the flow properties of the material, and shows that membranes based on pnc-Si exhibit gas permeances that are several orders of magnitude higher than in other similar membranes. The components of the flow due to ballistic transport and transport after collision with the pore walls are quantified as a function of pore diameter. In addition, we demonstrate that changing the pore interior from silicon to carbon leads to flow enhancement resulting from a change in the nature of the molecule-pore wall interactions. Integrating the pnc-Si material into nanoscale devices is considered next. A novel approach to the fabrication of a capacitive sensor for organic vapor detection using a pnc-Si membrane metallized with gold as a porous electrode is presented. We show that the ultrathin

nature of the pnc-Si allows for fast analyte vapor permeation to the receptor material. Finally, we describe a technique for effectively depositing gold electrodes on different sides of the membrane that is used to fabricate an ultrathin electroosmotic pump. These metallized pumps are shown to achieve significantly higher flow rates compared to bare pnc-Si membranes when low voltages are applied directly across the membrane.

Contents

Dedication	ii
Curriculum Vitae	iii
Publications and Presentations	iv
Acknowledgments	vi
Abstract	viii
List of Figures	xiii
Foreword	1
1 Background and Introduction	3
1.1 Introduction to Membrane Technology	3
1.2 Porous Membranes Fabrication Techniques	7
1.3 Porous Nanocrystalline Silicon Membrane	11
1.4 Thesis Outline	13
2 Fabrication and Characterization of Porous Nanocrystalline Silicon Membrane (Pnc-Si)	14
2.1 Pnc-Si Membrane Fabrication	15
2.1.1 Photolithography	16
2.1.2 RF Magnetron Sputtering	17

2.1.3	Rapid Thermal Annealing	19
2.1.4	Chemical Etching	20
2.2	Pnc-Si Membrane Pore Morphology	22
2.3	Carbonization	23
2.4	E-beam Metallization	25
2.5	Characterization of Pnc-Si Membrane	27
2.5.1	Transmission Electron Microscopy	28
2.5.2	Scanning Electron Microscopy	28
2.5.3	Optical Profilometry Technique	30
2.5.4	Pore Size Distribution Calculation	30
2.6	Conclusions	32
3	Gas Flow through Pnc-Si Membrane	34
3.1	Background	35
3.2	Permeation Measurement Setup	41
3.3	Pnc-Si Membrane Performance	43
3.4	Knudsen Diffusion in Pnc-Si	45
3.4.1	Theoretical and Experimental Pnc-Si Gas Permeance	45
3.4.2	Molar Mass and Pressure Dependencies of Permeance	46
3.5	Ballistic and Non-Ballistic Gas Flow	51
3.6	Flow Enhancement in Carbonized Pnc-Si	56
3.7	Conclusions	58
4	Chemical Capacitive Sensing Using Pnc-Si Membrane	59
4.1	Electrical Sensors Background	60
4.2	Pnc-Si Membrane Capacitive Sensor	66
4.2.1	Pnc-Si Membrane as a Porous Electrode	66
4.2.2	Pnc-Si Membrane Capacitive Sensor Fabrication	69
4.3	Mechanical Stability of Pnc-Si Membrane	71
4.4	Pnc-Si deflection during PDMS swelling	73
4.5	Chemical Capacitive Sensing	74
4.5.1	Capacitance Measurement Setup	74

4.5.2	Detection of Different Solvent Vapors	76
4.5.3	Solvent Vapor Concentration Detection	78
4.6	Conclusions	79
5	Pnc-Si Membrane in Low Voltage Electroosmosis	80
5.1	Background of Electroosmotic Pumps	81
5.1.1	Fundamentals of Electroosmotic Flow	81
5.1.2	Electroosmotic Pumps	86
5.2	Pnc-Si Membranes as Electroosmotic Pumps	88
5.2.1	Pnc-Si Electrodes Fabrication by Glancing Angle Deposition .	89
5.2.2	Optimization of Electrode Deposition Parameters	92
5.2.3	Silver-Silver Chloride Electrodes	96
5.3	Volumetric Flow Rate Measurement Setup	97
5.4	Pnc-Si EO Pump Performance Evaluation	102
5.5	Conclusions	108
6	Conclusions and Future Outlook	109
6.1	Gas Flow through Carbonized Pnc-Si Membranes	110
6.2	Pnc-Si Based Capacitive Sensor Performance	110
6.3	Pnc-Si Electroosmotic Pump Optimization	111
	Bibliography	113

List of Figures

1.1	A diagram of the membrane characteristics that influence on the performance.	4
1.2	Membrane classification based on the pore size: molecular sieves, nanofiltration, ultrafiltration, microfiltration membranes.	5
1.3	Comparison of sponge- and sieve-like porous membrane geometries: a) conventional sponge-like polymeric membrane has significant resistance to fluid flow; b) ultrathin sieve-like porous nanocrystalline silicon (pnc-Si) membrane has almost no resistance to the flow.	6
1.4	SEM image of polyethylene terephthalate track-etched membrane. . .	7
1.5	SEM images of AAO membrane surface (a, b) and cross section (c, d). Scale bars: a) 1 μm ; b) 200 nm; c) 50 μm ; d) 2 μm	9
1.6	Cross-sectional SEM images of CNT membranes fabricated by inserting CNTs into a polymeric (a) or silicon nitride matrix (b), and by collapsing vertically grown CNT arrays into dense membranes by capillary forces due to solvent evaporation (c). Scale bar in (a) is 2.5 μm	10
1.7	SEM images of sieve-like silicon nitride membranes fabricated using: a) focused ion beam drilling (scale bar is 50 nm); b) laser interference lithography (scale bar is 200 nm).	11
1.8	a) SEM image of the surface of 15 nm thick porous nanocrystalline silicon membrane; b) SEM image of the pnc-Si cross section imaged on the surface of metallized silicon wafer reveals cylindrical nature of the pores.	12

2.1	Porous nanocrystalline silicon membrane fabrication steps.	15
2.2	Schematic of the sputtering process.	17
2.3	AJA International ATC-2000-V RF magnetron sputtering tool.	18
2.4	TEM images of as-deposited 15 nm thick amorphous silicon (a) and RTP treated 15 nm a-Si (pnc-Si) (b). The a-Si film (a) has no voids and crystalline features. In pnc-Si (b) the circular white areas are open pores, the surrounding areas correspond to nanocrystalline silicon and nanocrystals.	20
2.5	Pnc-Si chips of different shapes with different pnc-Si membrane geometries: a) pnc-Si chips on a 4-inch silicon wafer; b) round pnc-Si chip with two membrane slits; c) square chips with five pnc-Si membrane slits.	21
2.6	Bright filed TEM images of 15 nm and 30 nm thick pnc-Si membranes.	22
2.7	TEM images of pnc-Si membrane before and after rapid thermal carbonization in acetylene at 700 °C for 5 minutes.	23
2.8	High resolution TEM image of the carbon coated pore in carbonized pnc-Si membrane.	24
2.9	CHA e-beam evaporation tool.	25
2.10	TEM micrograph of the 30 nm thick pnc-Si membrane coated on one side (a) and both sides (b) with 15 nm Au/Ti film.	26
2.11	SEM micrographs of pnc-Si membrane surface next to the broken edge (a) and the cross section of the pnc-Si membrane used to determine membrane thickness (b).	29
2.12	Pore processing using TEM image: a) original pnc-Si TEM image; b) black and white image after background correction and applying a threshold algorithm; c) background corrected TEM image with outlined pores; d) pore distribution histogram.	31
2.13	Histograms and TEM images from three different positions (from a set of ten) on the same pnc-Si membrane used for standard error calculations. The calculated standard error for the porosity value is 2 % and for the average pore diameter is less than 1 %.	32

3.1	Gas flow regimes as functions of system dimensions and pressure.	36
3.2	Schematic of specular and diffusive reflections.	39
3.3	Schematic of the gas permeance measurement setup.	42
3.4	Measured N ₂ permeances of pnc-Si membrane, polycarbonate track-etched membrane and reported permeance of three CNT membranes. The pore sizes are indicated in the figure. Experimental values for TE membranes agree with data provided by the manufacturer.	44
3.5	Theoretical permeance pore-by-pore calculation: a) TEM image of pnc-Si membrane and the same image with outlined pore edges to find pore statistics, including pore diameters, porosity and pore areas. The image processing is done in MATLAB; b) Pore-by-pore calculation of theoretical gas flow rate through a typical membrane using Equation 3.6 is used to calculate the theoretical permeance of the membrane.	47
3.6	Experimental and theoretical N ₂ permeance of pnc-Si membranes with different porosities and pore size distributions. The theoretical value for each membrane is calculated by summing the flow rates through individual pores and using the pore distribution histogram. The inset is a typical pore size distribution histogram obtained from TEM measurements.	48
3.7	a) Measured N ₂ , He and CO ₂ permeance as a function of molar mass M . Lines represent measurements on 22 different pnc-Si membranes, the average slope of fitted lines is -0.45 ± 0.05 . The line of slope $-1/2$ is a guide for the eye. b) The experimental selectivity α of 22 membranes expressed as the ratio of single gas permeances measured under identical conditions for each of the three gas pairs, compared to the theoretical selectivity coefficients $\alpha = \sqrt{\frac{M_{gas2}}{M_{gas1}}}$ (0.798 for CO ₂ /N ₂ pair, 0.378 for N ₂ /He, 0.302 for CO ₂ /He).	49
3.8	N ₂ permeance of the same pnc-Si membrane measured at different pressures. Permeance is independent of the pressure suggesting a negligible contribution of viscous flow.	50
3.9	Ballistic flow component W_{ss} for pores of different diameters and lengths.	52

3.10	Experimental P of pnc-Si membranes from five different wafers before and after carbonization compared to theoretical Knudsen predictions. Initial wafer porosities and average pore diameters from left to right are: 1) 2.5% (25.5 nm); 2) 2.87% (27.8 nm); 3) 3.25% (18.4 nm); 4) 4.97% (23.7 nm); 5) 5.09% (22.9 nm). The corresponding porosities and average pore diameters after the membranes were carbonized are: 1) 1.34% (20.5 nm); 2) 1.3% (21.3 nm); 3) 1.91% (17.1 nm); 4) 2.86% (18.5 nm); 5) 2.87% (20.7 nm).	54
3.11	Experimental P_{norm} of 15 nm thick pnc-Si membranes plotted against mean pore diameter. The dashed line is added to guide the eye. . . .	55
3.12	Experimental P_{norm} of 23.5 nm thick pnc-Si and c-pnc-Si membranes plotted against mean pore diameter. The wall component of P_{norm} is found by subtracting the calculated W_{ss} component from the total measured P_{norm} . The error in the wall components of P_{norm} due to the pore size distribution is less than 0.5%. The dashed lines are least squares fits.	57
4.1	Cross-sectional and top schematics of the parallel-plate capacitive sensor geometry.	63
4.2	Cross-sectional and top images of interdigitated electrodes based capacitive sensor.	65
4.3	Schematic of the pnc-Si membrane based chemical capacitive sensor. .	66
4.4	TEM images of the same 15 nm thick pnc-Si membrane before and after metallization with 15 nm Ti/Au bilayer demonstrate that pores have not been occluded.	67
4.5	TEM images of the same 15 nm pnc-Si membrane with no metal, 13 nm, and 20 nm metal layers deposited on top. The image shows how porosity and average pore diameter of pnc-Si membranes change with the deposited metal thickness.	68
4.6	Fabrication steps of chemical capacitive sensor based on pnc-Si membrane: metal deposition, PDMS spin-coating, bonding and PDMS curing.	70

4.7	TEM images of the same pnc-Si membrane before and after repeatable stretching at 15 psi. After the imaging, the membrane burst pressure was measured to be 16 psi. The images show that the positions of the nanocrystals and the pores stay unchanged after stretching.	71
4.8	3D optical profilometry images of a pnc-Si/PDMS/Si structure taken from well-side of the pnc-Si membrane: a) before exposure to xylene vapor; b) immediately after exposure to xylene vapor; c) approximately 2 minutes after the xylene vapor is removed. The wall-like area around the membrane window is an artifact of the imaging as the optical profiler picks up the signal reflected not only from the square membrane area but also from the walls of the silicon well which was etched to expose the freestanding pnc-Si membrane. The results show that xylene vapor permeates through the membrane and reversibly changes PDMS thickness.	73
4.9	Capacitance measurement setup.	75
4.10	Capacitive response of the sensor upon exposure to hexane, toluene and acetone vapors.	77
4.11	Capacitive response of the sensor upon exposure to 100, 200, 300, 400 ppm xylene concentrations.	78
5.1	Fraction of positive, negative and neutral sites on SiO ₂ surface in water at different pH values.	82
5.2	Schematic of the electrical double layer (EDL) formed by a negatively charged surface and electrokinetic potential ψ distribution. ψ_0 is surface potential, ζ is zeta potential, y is distance from the surface, λ_D is the Debye length.	84
5.3	Velocity profile of the electroosmotic flow in a channel with negatively charged surface.	85
5.4	Examples of pump geometries: a) porous anodic alumina membrane pump; b) pump based on porous glass substrate composed of silica and borosilicate particles; c) microfabricated pump.	87

5.5	Schematic of the pnc-Si membrane based electroosmotic pump.	89
5.6	a) Schematic of the glancing angle deposition technique showing the partial pnc-Si pore coverage due to directional metal vapor flux; b) wafer positioning during glancing angle deposition.	90
5.7	TEM images of pnc-Si with gold deposited on one side at: a) normal incidence and b) glancing incidence. The metal film deposited at the normal incidence conformally coats the pores, as seen in TEM image of (a). The gold film deposited at glancing incidence coats only one side of the pores as seen in TEM image of (b).	91
5.8	Schematic of material evaporation from point source and surface source.	92
5.9	SEM images of the 15 nm and 25 nm metal films deposited on 30 nm thick pnc-Si membrane at different angles α and β . The corresponding angles, metal film thickness t and measured resistance R magnitude are inserted in the images.	93
5.10	SEM images of gold films of different thicknesses deposited on 30 nm thick pnc-Si membrane at $\alpha=65^\circ$ and $\beta=90^\circ$: a) 21 nm; b) 19 nm; c) 15 nm. Some of the dark areas in (b) and (c) are bare pnc-Si membrane areas with pores, which are not covered with metal.	94
5.11	Cross-sectional SEM images of the 30 nm thick pnc-Si with metal layers deposited at the glancing angle on both sides.	95
5.12	Charge transfer reactions occurring at silver-silver chloride electrodes.	96
5.13	Schematic of the experimental setup used to test pnc-Si EO pump.	98
5.14	Image of the NaCl solution droplet on top of the bare pnc-Si membrane pump with attached Ag/AgCl electrodes. The silicone seal can be seen around the edges of the pnc-Si membrane.	99
5.15	Images of the NaCl solution droplet on top of the metallized with gold on both sides pnc-Si membrane pump with attached Ag/AgCl electrodes: a) before pumping; b) after pumping.	100
5.16	Side view images of the NaCl droplet on a metallized pnc-Si pump before (a) and after (b) pumping, showing the droplet height change.	101

- 5.17 Four types of EO pumps built on as-prepared and metallized pnc-Si membranes: a) bare pnc-Si membrane, Ag/AgCl electrodes attached to silicon surfaces; b) pnc-Si with top surface covered with gold, Ag/AgCl electrodes attached to gold and bottom silicon surface; c) both pnc-Si membrane surfaces covered with gold, Ag/AgCl electrodes attached to gold surfaces; d) both pnc-Si membrane surfaces covered with gold, Ag/AgCl electrodes attached to the top gold and bottom silicon surface. 103
- 5.18 Average volumetric flow rates of different pnc-Si EO pumps at different voltages. The samples include a bare pnc-Si membrane, a pnc-Si membrane with only the top surface metallized with gold and a pnc-Si membrane with both surfaces metallized with gold. Each of the pumps has Ag/AgCl electrodes attached to both sides as shown in Figure 5.17. The error bars indicate the maximum and minimum values measured. 104
- 5.19 Average volumetric flow rates (shown in Figure 5.18) normalized by porosity for different pnc-Si EO pumps at different voltages. 105

Foreword

This work was done in a collaboration with the Nanomembrane Research Group led by Prof. Philippe M. Fauchet and Prof. James L. McGrath, and SiMPore Inc. Dr. Christopher Striemer is the inventor of the porous nanocrystalline silicon membrane. Membranes used in this work were fabricated by SiMPore, John-Paul DesOrmeaux, Dr. David Fang and Charles Chan. Dr. Michael Bindschadler developed the pore processing software. The scanning electron microscopy was performed in part by Krishanu Shome. The transmission electron microscopy was performed in part by Dr. David Fang. The development and evaluation of the research have been discussed with colleagues Prof. P. M. Fauchet, Prof. J. L. McGrath, Dr. C. C. Striemer, Dr. T. R. Gaborski, J.-P. S. DesOrmeaux, Dr. D. Z. Fang, Dr. J. L. Snyder, Chengzhu Qi in numerous Nanomembrane Group Meetings. Other contributions from colleagues are listed below.

Chapter 1 is an academic literature review and an introduction to the pnc-Si membrane. Chapter 2 includes descriptions and theoretical backgrounds of processes used for pnc-Si membrane fabrication, and techniques used for membrane characterization

and modification. Chapter 3 is based on the article "Ballistic and non-ballistic gas flow through ultrathin nanopores" published in *Nanotechnology* by M. N. Kavalenka, C. C. Striemer, D. Z. Fang, T. R. Gaborski, J. L. McGrath and P. M. Fauchet. We acknowledge Prof. M. Anthamatten for useful discussions. The experiments and analysis of the results were performed by the author. Chapter 4 is based on the article "Chemical capacitive sensing using ultrathin flexible nanoporous electrodes" published in *Sensors and Actuators, B: Chemical* by M. N. Kavalenka, C. C. Striemer, J.-P. S. DesOrmeaux, D. Z. Fang, J. L. McGrath and P. M. Fauchet. The sensor fabrication, experiments and results analysis were performed by the author. Chapter 5 is unpublished work. The pnc-Si based pumps fabrication and optimization was performed by the author. The EO flow measurements were performed by the author with the help of Jirachai Getpreecharsawas from the group of Prof. David Borkholder at the Rochester Institute of Technology.

Chapter 1

Background and Introduction

1.1 Introduction to Membrane Technology

Membrane structures appear throughout nature, and come in many different shapes and sizes. Cells and intracellular components, for example, are surrounded by highly selective plasma membranes that protect them from the outside environment, and provide means of communication by exchanging molecules and ions through channels in the membrane. Attempts to understand the mechanisms that control transport and separation of species in the cellular membranes have led to the development of new nanoscale devices and applications that aim to mimic these processes. Implementing such processes, including forms of selective transport, molecular or ion exchange, and fluid flow control, requires having an effective artificial porous membrane that can be crafted for these purposes. It is for this reason that membrane technology and theory is essential for fields as diverse as general science, medicine, engineering and

industrial domains, which rely on this technology.

By definition, a membrane is a physical barrier that separates two fluid volumes and selectively controls the transport of molecules between them. The primary performance goals of the porous membrane include achieving high rates of mass transport with low energy input, selectivity over molecular species in a mix, mechanical and chemical stability, and biocompatibility. The membrane properties that lead to better performance are high porosity, small thickness, controlled pore morphology and surface properties. A schematic diagram of the key membrane characteristics and their influence on membrane performance are summarized in Figure 1.1 [1].

Porous membranes are classified by the material they are made of (biological, organic, inorganic), their structure morphology (sponge- or seive-like structures), and pore size. Membranes are divided into the following groups by the average pore

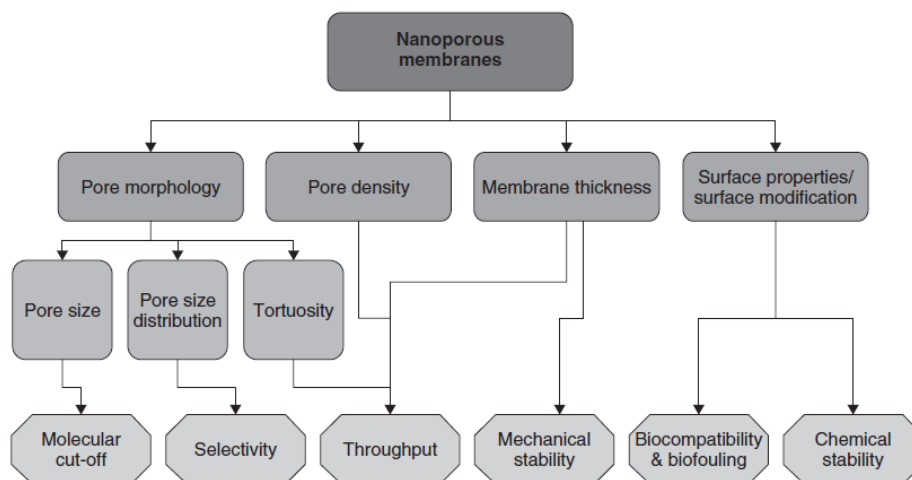


Figure 1.1: A diagram of the membrane characteristics that influence on the performance [1].

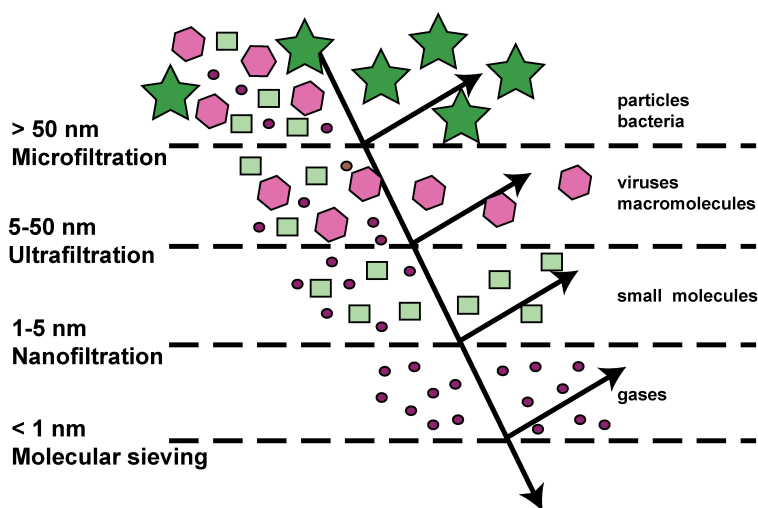


Figure 1.2: Membrane classification based on the pore size: molecular sieves, nanofiltration, ultrafiltration, microfiltration membranes.

diameter: microfiltration membranes (with pore diameter $d > 50$ nm); ultrafiltration membranes ($5 \text{ nm} < d < 50$ nm); nanofiltration membranes ($1 \text{ nm} < d < 5$ nm); and molecular sieves ($d < 1$ nm) [2]. Figure 1.2 presents this classification and the use of different membranes for the separation of particles and molecules of different sizes.

Most of the porous membranes have a sponge-like structure, for example, polymeric membranes fabricated using a phase-inversion technique [2]. Such geometry adds additional resistance to the flow and increases fouling of the material inside the membrane. Another class of membranes that has a straight and uniform pore structure is known as sieve-like membranes. Sieve-like membranes include commercially available polycarbonate track-etched membranes [3] and anodic alumina membranes [4], carbon nanotube based membranes [5], and microfabricated ultrathin membranes [6, 7].

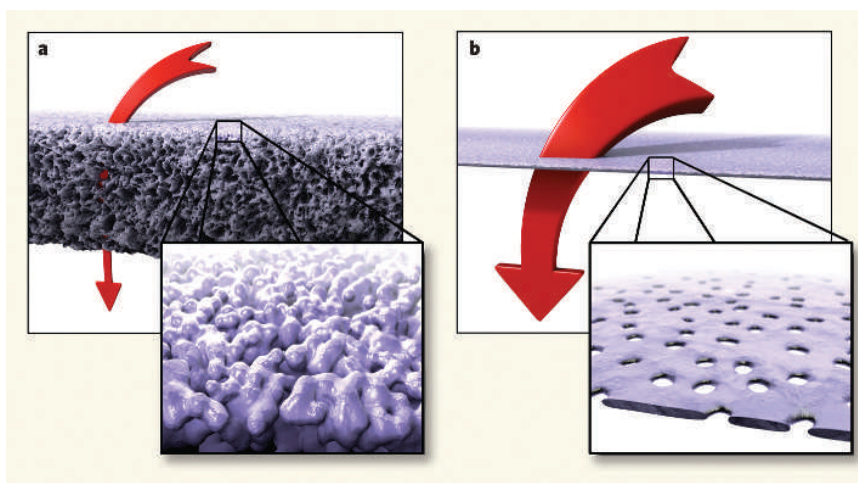


Figure 1.3: Comparison of sponge- and sieve-like porous membrane geometries: a) conventional sponge-like polymeric membrane has significant resistance to fluid flow; b) ultrathin sieve-like porous nanocrystalline silicon (pnc-Si) membrane has almost no resistance to the flow [8, 9].

Membrane technology is a rapidly emerging interdisciplinary field that has inherited many techniques from semiconductor manufacturing, materials science, chemistry and engineering. Using semiconductor processing techniques allows for the fabrication of ultrathin nanosieve membranes with very little resistance to the flow since the permeation rate through the membrane is inversely proportional to its thickness. The ultrathin nanosieve membrane is compared to the sponge-like membrane in Figure 1.3 [8, 9].

Porous membranes have a broad range of applications. Nanoengineered porous membranes are found in lab-on-chip devices, separations/filtrations, nanoelectromechanical and nanofluidic systems applications [5, 6, 10, 11], including bio- and chemical sensors [12, 13], electrochemical pumps [14, 15], nanofluidic transistors [16], single

molecule detection [17, 18], DNA sequencing [19], nanoparticle arrays fabrication [20], protein purification and separation [21], blood filtration in dialysis [22, 23, 24], water purification and desalination, and gas separations [2, 25].

1.2 Porous Membranes Fabrication Techniques

The most popular types of sieve membranes are track-etched (TE) and anodic aluminum oxide (AAO) membranes, both of which are commercially available. TE membrane fabrication consists of two steps. First, a dense polymer film is irradiated with high-energy ions. The ions pass through the film, leaving behind tracks of damaged polymer chains. A chemical etch then removes the polymer along the tracks, forming through pores. The exposure time of the membrane to the ion bombardment determines the number of pores, and the etch duration controls the size of the pores. Heavy ions such as argon or xenon are used to track polymer films. Polycarbonate,

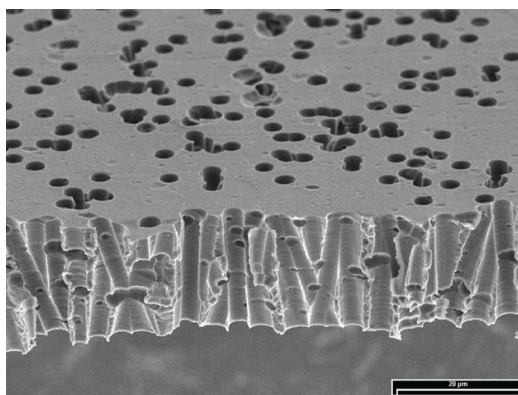


Figure 1.4: SEM image of polyethylene terephthalate track-etched membrane [25]. Scale bar is 20 μm

polyester or polyethylene terephthalate are used as base polymer materials [2, 25, 26].

TE membranes have a narrow pore size distribution, and typically are 10 to 100 μm thick with pore sizes from 10 nm to tens of microns, as shown in Figure 1.4 [25]. Although these membranes are widely used and commercially available [3, 27], they have several disadvantages including having low chemical and thermal stability. For example, they can withstand temperatures only up to 150 $^{\circ}\text{C}$. In addition, in order to minimize pore overlapping, which happens when the ion tracks are too close to each other as can be seen in Figure 1.4, the membranes are made with low porosities ranging from 5 to 10 %.

Recently, a TE membrane fabrication technique was used to make pores in silicon nitride membranes. Bismuth ions at an energy of 710 MeV and 170 MeV xenon ions were used to irradiate silicon nitride film due to its high radiation resistance. The resulting freestanding membrane is 200-300 nm thick with pore diameters 3-20 nm [26, 28].

The pores in an anodized aluminum oxide Al_2O_3 (AAO) membrane are formed by anodizing aluminum in acidic solutions. The cylindrical pores in the AAO membrane self-organize into a highly ordered uniform array that has a honeycomb structure shown in Figure 1.5 [4]. Solutions of sulfuric (H_2SO_4), phosphoric (H_3PO_4) or oxalic acid ($\text{H}_2\text{C}_2\text{O}_4$) are used for anodization [29]. The pore dimensions are defined by such anodization conditions as voltage, time, electrolyte concentration and temperature [4].

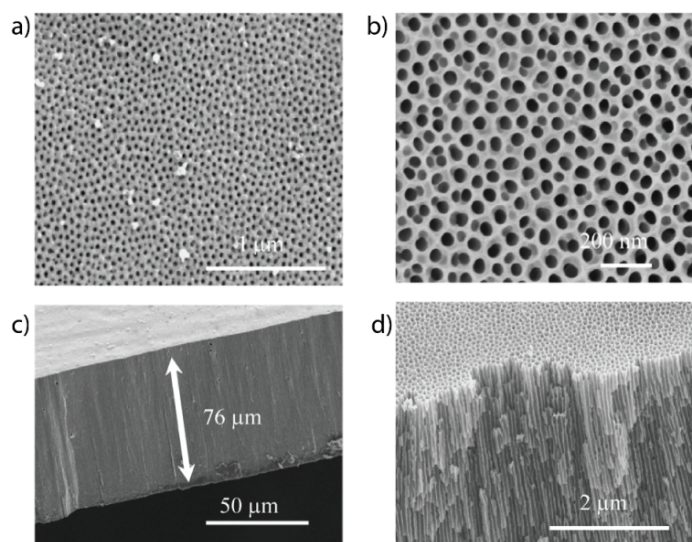


Figure 1.5: SEM images of AAO membrane surface (a, b) and cross section (c, d). Scale bars: a) $1\ \mu\text{m}$; b) $200\ \text{nm}$; c) $50\ \mu\text{m}$; d) $2\ \mu\text{m}$ [4].

AAO membrane porosity can reach up to 50 %, pore diameters range from 20 to 200 nanometers, and the typical membrane thickness is $60\ \mu\text{m}$ [2, 27]. Unlike polymeric TE membranes, AAO membranes have good chemical and temperature stability, but they are brittle which limits their use in many applications.

The thickness of AAO membranes is an important limitation for achieving high permeability rates. Recently, AAO membranes with thickness $0.7\text{-}1.0\ \mu\text{m}$ and narrow pore distribution $20\text{-}30\ \text{nm}$ have been fabricated by depositing and anodizing aluminum on top of the silicon wafer, followed by the removal of silicon [30].

Carbon nanotube (CNT) membranes are a recently developed type of sieve membrane in which carbon nanotubes serve as pores [33]. CNT membranes are fabricated either by inserting CNTs into a polymeric or silicon nitride matrix [5, 31, 34], or by

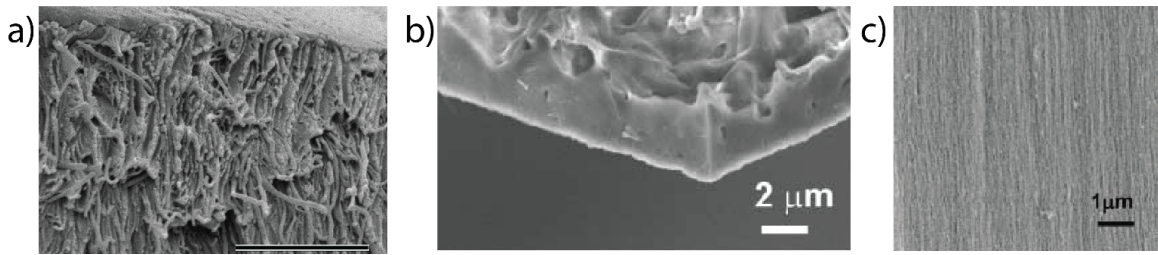


Figure 1.6: Cross-sectional SEM images of CNT membranes fabricated by inserting CNTs into a polymeric (a) [5] or silicon nitride matrix (b) [31], and by collapsing vertically grown CNT arrays into dense membranes by capillary forces due to solvent evaporation (c) [32]. Scale bar in (a) is $2.5 \mu\text{m}$.

collapsing vertically grown CNT arrays into dense membranes by capillary forces due to solvent evaporation [32] as shown in Figure 1.6. Their thicknesses range from a few microns to a few hundred microns. CNT membranes have improved gas and water transport properties due to low surface friction [11].

A number of current semiconductor manufacturing techniques including thin film deposition, photolithography and etching techniques are used to create freestanding ultrathin nanoseive membranes with uniform cylindrical pores from various materials. Nanometer-size pores can be created one by one in ultrathin silicon or silicon nitride films by focused ion beam (FIB) drilling [6], electron beam (e-beam) lithography followed by reactive ion etching (RIE), or e-beam drilling in a transmission electron microscope (TEM) [35, 36]. Tong *et al.* reported a 10 nm thick silicon nitride membrane with 25 nm diameter pores prepared by FIB drilling [6]. Laser interference lithography (LIL) is used as the technique to create a nanopore pattern in silicon nitride film [7]. SEM images of the membranes fabricated using FIB and LIL are

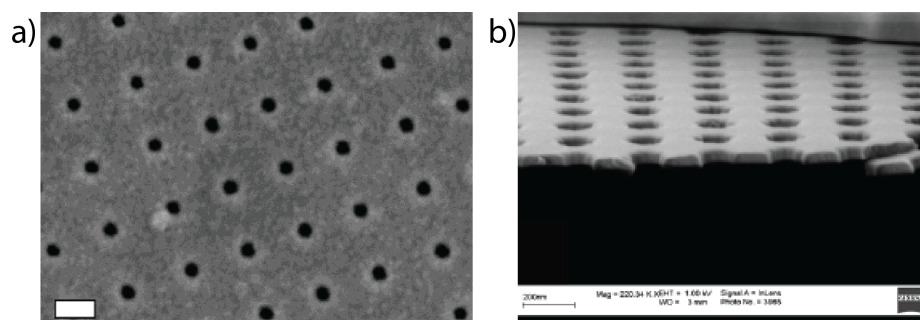


Figure 1.7: SEM images of sieve-like silicon nitride membranes fabricated using: a) focused ion beam drilling (scale bar is 50 nm) [6]; b) laser interference lithography (scale bar is 200 nm) [7].

shown in Figure 1.7 [6, 7]. Although porous membranes fabricated using these techniques possess many beneficial properties such as controlled porosity, narrow pore size distribution, repeatability and easy integration into lab-on-chip devices, they cannot be easily scaled up for mass fabrication due to time consuming processing steps and high costs.

1.3 Porous Nanocrystalline Silicon Membrane

Porous nanocrystalline silicon (pnc-Si) is a novel membrane material in which nanopores are produced by crystallizing a thin amorphous silicon film at a high temperature [9]. This is a bottom-up approach, which is distinct from other thin nanoengineered membranes where pores are formed using conventional lithographic techniques. Pnc-Si membranes satisfy all of the requirements necessary for good performance since they have high porosity, narrow pore size distribution and small

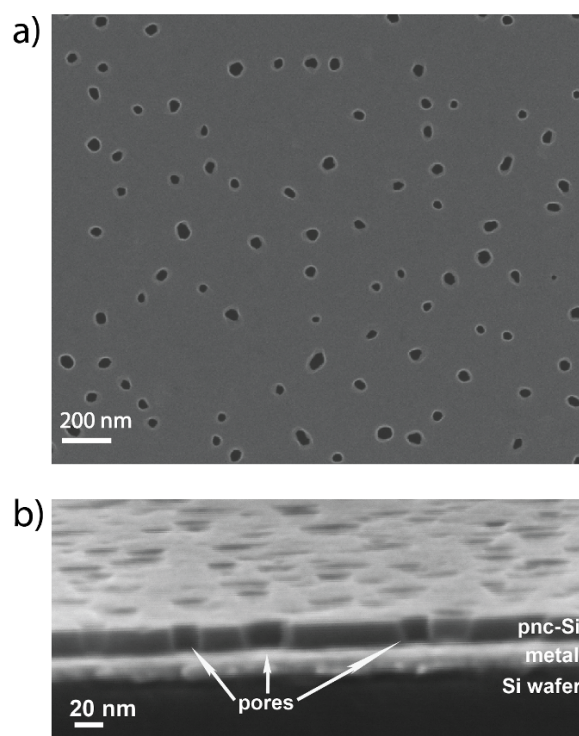


Figure 1.8: a) SEM image of the surface of 15 nm thick porous nanocrystalline silicon membrane; b) SEM image of the pnc-Si cross section imaged on the surface of metallized silicon wafer reveals cylindrical nature of the pores.

thickness. Pnc-Si membranes typically are 15-30 nm thick with pore diameters ranging from 5 to 80 nm and porosity from 0.1 to 15 %. They have been shown to exhibit hydraulic permeability orders of magnitude higher than existing similar membranes [37], and have demonstrated precise separations of nanoparticles and proteins [37, 38]. They have also been successfully used for chemical sensing [12, 39] and as cell culture substrates [40]. SEM images of a 15 nm thick pnc-Si surface and cross section are shown in Figure 1.8 [41]. The use of semiconductor manufacturing techniques for membrane fabrication allows for easy scalability.

1.4 Thesis Outline

This thesis is organized as follows. In Chapter 2, the details of porous nanocrystalline silicon (pnc-Si) membrane fabrication, surface modification techniques including carbonization and metalization, and methods used for characterizing the pnc-Si membrane and devices based on it are discussed. In Chapter 3, the physical dimensions of the molecularly thin pnc-Si membranes, and their dependence on the manufacturing parameters, are exploited to observe the components of gas flow through ultrathin nanopores and their dependence on the pore surface. The performance of the pnc-Si membrane is investigated and found to be several orders of magnitude higher than other membranes. The thinness and high permeation rates of these membranes are advantageous for many applications, including sensing and nanofluidics. Pnc-Si membranes metallized with gold are used as flexible conductive electrodes in a chemical capacitive vapor sensor for solvent vapor detection as discussed in Chapter 4. The mechanical stability and elasticity of the pnc-Si are experimentally tested. Optical and electrical techniques are used to characterize the sensor. In Chapter 5 a novel technique for depositing electrically isolated electrodes on the pnc-Si membrane is developed, and used for a low voltage electroosmotic pump fabrication. Conclusions and comments on future research are presented in Chapter 6.

Chapter 2

Fabrication and Characterization of Porous Nanocrystalline Silicon Membrane (Pnc-Si)

This chapter focuses on the fabrication and characterization of the porous nanocrystalline silicon membrane. Semiconductor fabrication techniques used for membrane manufacturing including photolithography, sputtering, annealing and wet chemical etching are described in Section 2.1. The relation between the membrane's pore morphology and fabrication parameters are described in Section 2.2. Surface modification techniques including carbonization and metallization are described in Sections 2.3 and 2.4. In Section 2.5 the methods used for characterizing the membrane and membrane-based devices are summarized. The chapter is concluded in Section 2.6.

2.1 Pnc-Si Membrane Fabrication

Porous nanocrystalline silicon (pnc-Si) membranes that are fabricated using standard semiconductor processing techniques are typically 15 or 30 nm thick with pore diameters ranging from 5 to 80 nm and porosities ranging from 0.1 to 15 %. Silicon wafers used for pnc-Si fabrication have the following characteristics: a 4-inch diameter, 200 μm thickness, $\langle 100 \rangle$ orientation, and are double-polished and n-type doped. The steps in the pnc-Si fabrication process are schematically outlined in Figure 2.1 [9, 42] and further described in the following subsections.

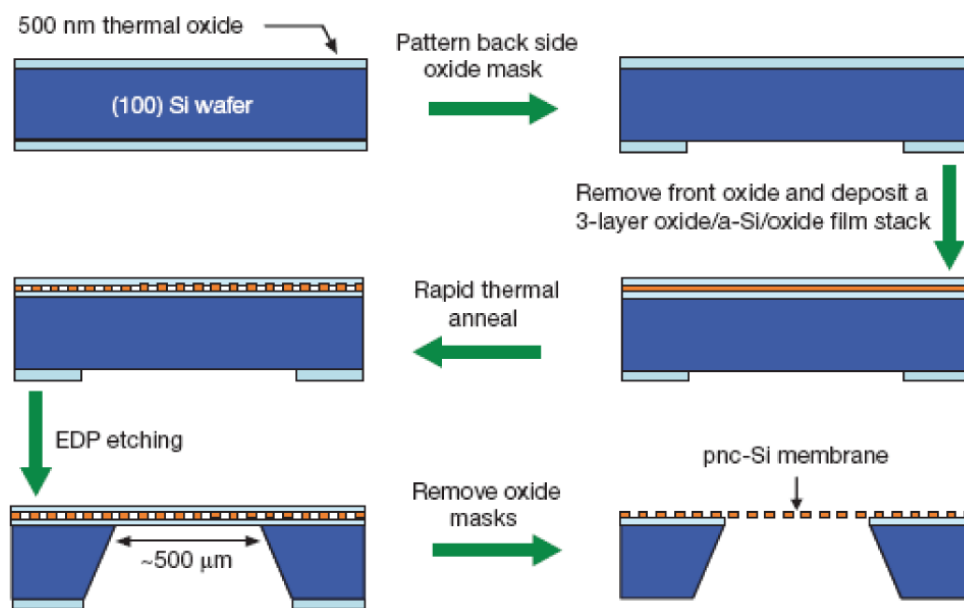


Figure 2.1: Porous nanocrystalline silicon membrane fabrication steps [9].

2.1.1 Photolithography

Photolithography is used to define the active area and the shape of the pnc-Si membrane chip by providing a patterned silicon dioxide (SiO_2) mask on the backside of the silicon wafer. This single photolithographic step consists of several subprocedures, including wafer cleaning, oxide deposition, photoresist application, exposure and developing, oxide etching and photoresist removal.

Since photolithography is sensitive to contamination, a silicon wafer is first cleaned using a standard RCA clean. RCA clean consists of a series of aqueous chemical baths (standard cleans SC-1 and SC-2) in which the silicon wafer is immersed for short periods of time. The SC-1 clean is a 15:1:3 mixture of deionized water/ ammonium hydroxide (NH_4OH)/ hydrogen peroxide (H_2O_2) at 75°C in which the wafer is immersed for 10 minutes. SC-1 chemistry removes organic contaminants and surface impurities. A brief 20 second dip in 50:1 aqueous solution of hydrofluoric acid (HF) is used after the SC-1 step for native silicon oxide layer removal. The second stage of the RCA clean SC-2 (10 minutes soak in 15:1:3 mixture of deionized water/ hydrochloric acid (HCl)/ H_2O_2 heated at 75°C) removes metal contaminants [43].

Following the RCA clean, a 100 nm thick dry thermal oxide is grown on both sides of the wafer in a tube furnace. The oxide layer on the backside of the wafer is then patterned using standard photolithographic techniques. First, hexamethyldisilazane (HDMS) and positive photoresist (Shipley 1813) layers are spun and baked on the

backside of the oxidized wafer. HDMS is used to promote better photoresist adhesion to the wafer. Subsequently, the photoresist is exposed to UV light through a patterned transparency mask and developed. The pattern in the SiO_2 layer is etched and the front oxide is removed during the same step using a 1:10 aqueous HF solution. Finally, the photoresist is removed and the wafer is RCA cleaned again.

2.1.2 RF Magnetron Sputtering

Thin films for pnc-Si membrane formation are deposited on a pre-patterned silicon wafer using RF magnetron sputtering. Sputtering is a type of physical vapor deposition (PVD), which is best suited for thin film deposition since it has better

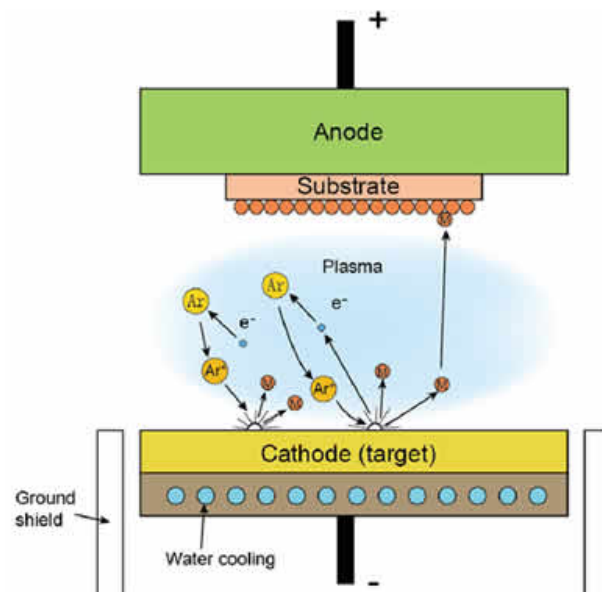


Figure 2.2: Schematic of the sputtering process [44].

film uniformity, lower deposition temperature, and allows co-sputtering from different targets.

The sputtering process starts by bombarding the target containing the material to be deposited with high energy gas ions accelerated in the electric field. An inert gas, such as argon, is introduced inside the vacuum chamber and used for plasma formation. After the collision with argon ions, atoms near the surface of the target become volatile, and are deposited on the substrate located near the target. The thickness of the film depends on the sputtering time. RF power supply is used when sputtering the insulators and semiconductors to prevent charge build-up. The magnetic field in the target area confines the plasma near the target to increase the probability of gas ionization and decrease the possibility of thin film damage [45]. The basic schematic

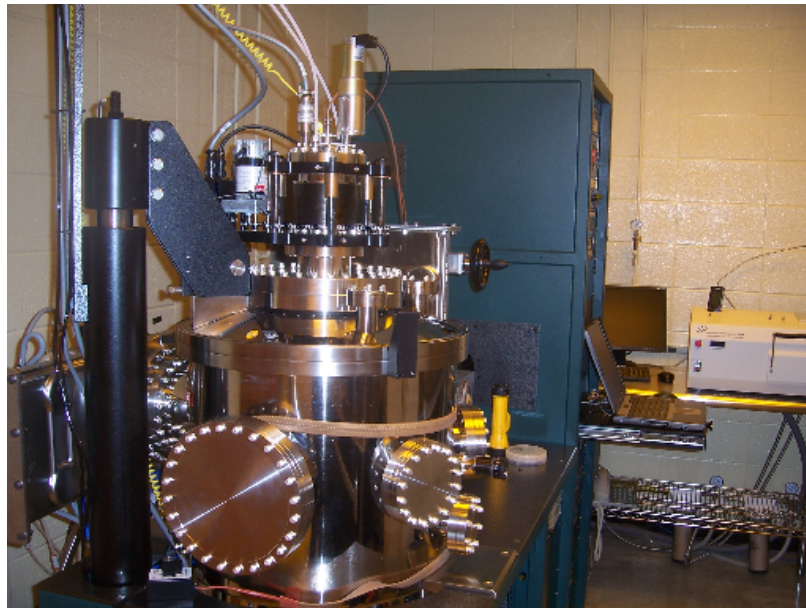


Figure 2.3: AJA International ATC-2000-V RF magnetron sputtering tool.

of the sputtering process is illustrated in Figure 2.2.

An AJA International ATC-2000-V RF magnetron sputtering tool (Figure 2.3) is used to deposit a three layer film stack that forms the base of the pnc-Si membrane. The structure deposited on the front surface of the patterned silicon wafer consists of three layers (20 nm SiO_2 /15-30 nm amorphous Si/20 nm SiO_2). Both protective oxide and amorphous silicon layer thicknesses influence the pnc-Si pore morphology, and this is later described in Section 2.2.

2.1.3 Rapid Thermal Annealing

The three layer film stack deposited in the previous step ($\text{SiO}_2/\text{a-Si}/\text{SiO}_2$) is treated at high temperature in a rapid thermal processing (RTP) chamber to induce amorphous silicon crystallization. The voids in the silicon film formed due to silicon phase transformation during annealing later become the open pores in the membrane. RTP annealing results in porous nanocrystalline silicon (pnc-Si) material formation.

A Surface Science Integration Solaris 150 rapid thermal processor (RTP) is used for annealing. RTP temperatures range from 700 to 1100 °C. The final annealing temperature greatly influences the pnc-Si pore formation. Pores start to form in 15 nm a-Si film when annealed at approximately 700 – 750 °C. Annealing at higher temperatures (900 – 1100 °C) yields higher pore densities [42]. Transmission Electron

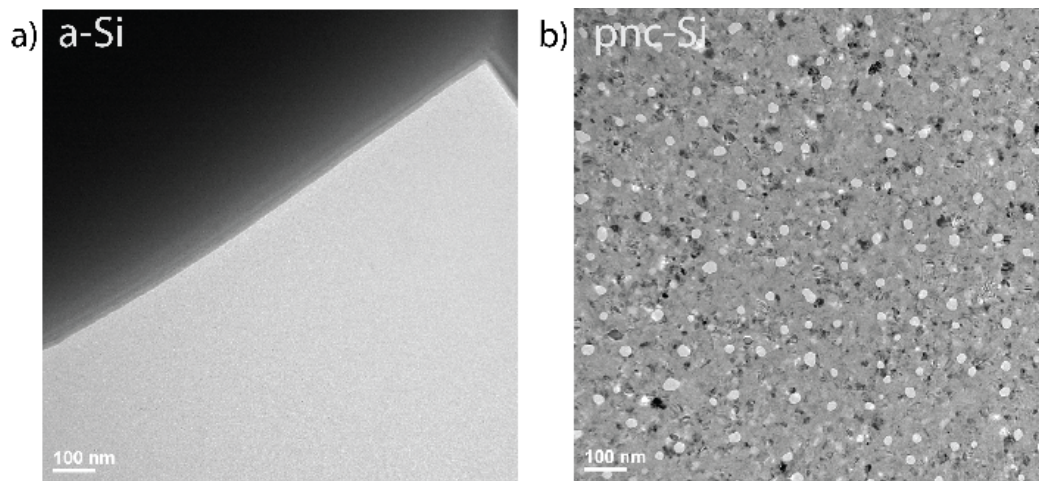


Figure 2.4: TEM images of as-deposited 15 nm thick amorphous silicon (a) and RTP treated 15 nm a-Si (pnc-Si) (b). The a-Si film (a) has no voids and crystalline features. In pnc-Si (b) the circular white areas are open pores, the surrounding areas correspond to nanocrystalline silicon and nanocrystals.

Microscopy (TEM) images of the as-deposited amorphous (a-Si) and RTP annealed a-Si are compared in Figure 2.4. The amorphous film has no voids or crystalline features in it (Figure 2.4(a)). In the pnc-Si TEM image (Figure 2.4(b)) the circular white areas are the open pores in the membrane, and the surrounding areas correspond to nanocrystalline silicon and nanocrystals.

2.1.4 Chemical Etching

After high temperature annealing, the patterned wafer backside is etched in an anisotropic etchant. The most commonly used anisotropic etchants are KOH (potassium hydroxide) and EDP (ethylenediamine pyrocatechol). EDP is a mixture of ethylene diamine ($\text{NH}_2(\text{CH}_2)_2\text{NH}_2$), pyrocatechol ($\text{C}_6\text{H}_4(\text{OH})_2$) and water. The main

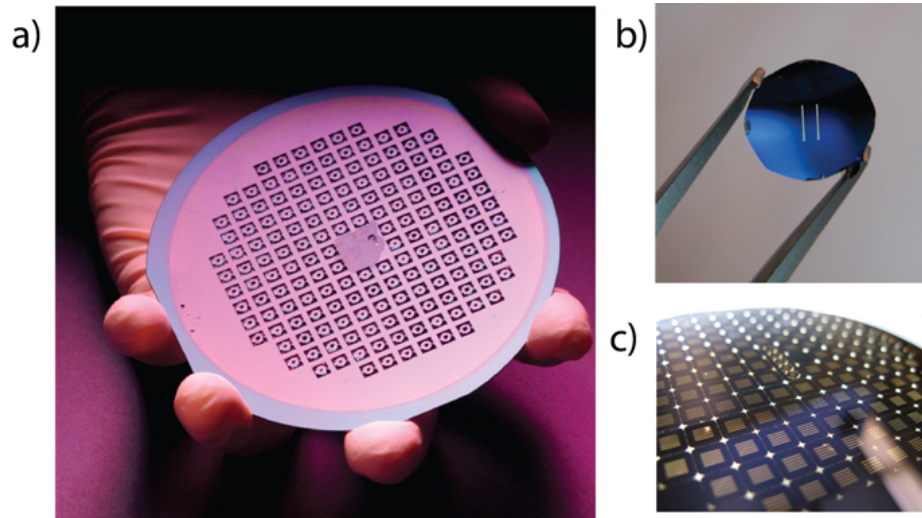


Figure 2.5: Pnc-Si chips of different shapes with different pnc-Si membrane geometries: a) pnc-Si chips on a 4-inch silicon wafer; b) round pnc-Si chip with two membrane slits; c) square chips with five pnc-Si membrane slits.

disadvantage of the KOH etch is that its 400:1 etching selectivity between Si and SiO_2 does not allow SiO_2 to be used as a masking layer in many applications. KOH etches SiO_2 at a rate of 1.4-3 nm/min. In contrast, the ratio of etch rates in EDP for Si and SiO_2 is approximately 5000:1, corresponding to Si and SiO_2 etch rates of 1 $\mu\text{m}/\text{min}$ and 0.2 nm/min [46]. Therefore the EDP etch is preferred over KOH for pnc-Si backside etching, since SiO_2 layers are used as a mask for backside etch and as an etch stop in pnc-Si fabrication. EDP removes silicon along the (111) crystal planes until the first SiO_2 layer of the film stack is reached, creating a freestanding structure on silicon support.

Lastly, the three layer membrane is exposed to a buffered oxide etchant (BOE) to

remove the protective SiO_2 layers, leaving only the freely suspended ultrathin pnc-Si membrane. The fabricated pnc-Si membrane chips of different shapes and with different membrane geometries are depicted in Figure 2.5.

2.2 Pnc-Si Membrane Pore Morphology

Fabrication parameters such as annealing conditions, silicon layer thickness and the application of the substrate bias during sputtering affect the membrane's pore morphology, density and size. By changing the annealing temperature from 700°C to 1000°C , the average pore diameter changes from 9.4 to 22.2 nm and the porosity from 0.5 to 6.6 %. A typical ramp rate of the annealing temperature used for pnc-Si fabrication is $50 - 100^\circ\text{C/s}$, and lower ramp rates result in irregularly shaped pores and wider pore size distributions [9, 42].

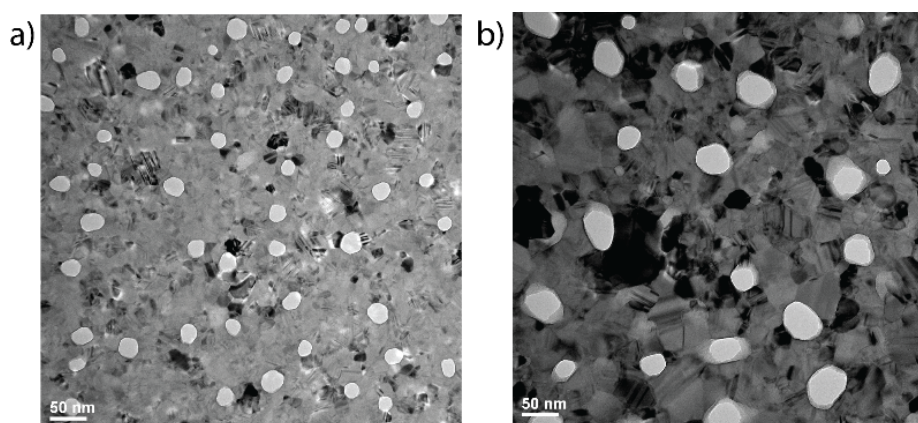


Figure 2.6: Bright filed TEM images of 15 nm (a) and 30 nm thick (b) pnc-Si membranes.

Increasing the thickness of the silicon layer leads to significant increase in pore sizes. TEM images of 15 nm and 30 nm thick pnc-Si membranes fabricated at similar conditions are shown in Figure 2.6.

2.3 Carbonization

Carbonization of porous template materials is typically done using chemical vapor deposition (CVD) [47, 48, 49, 50]. CVD is a process in which a solid film is formed from a gaseous phase by a chemical reaction, and is used to deposit a wide range of materials. During the CVD process, a porous substrate is placed in a furnace with hydrocarbon gas (propylene, ethylene, pyrene, acetylene) flowing through it. The thermal decomposition (pyrolysis) of hydrocarbon gas leads to a carbon film growth on the substrate surface. Carbon films synthesized using CVD are partially

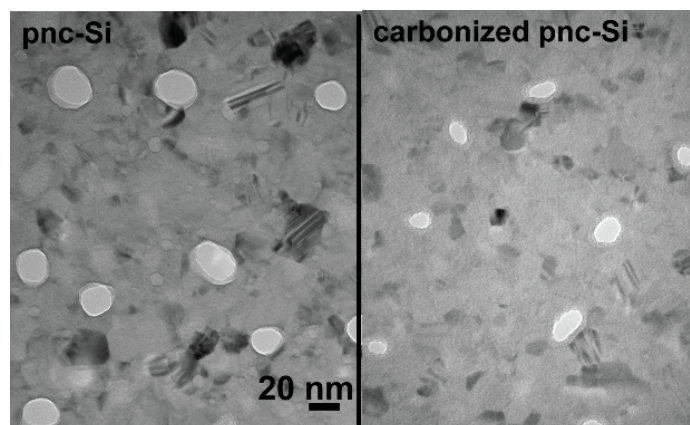


Figure 2.7: TEM images of pnc-Si membrane before and after rapid thermal carbonization in acetylene at 700 °C for 5 minutes.

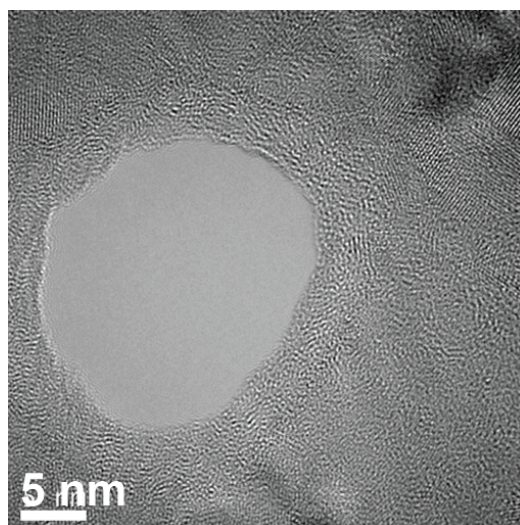


Figure 2.8: High resolution TEM image of the carbon coated pore in carbonized pnc-Si membrane.

amorphous [49]. Annealing at high temperatures was reported to improve the ordering of the carbon walls [48, 51].

Rapid thermal carbonization is used for depositing carbon on pnc-Si membranes [52, 53]. Carbonization is carried out in a rapid thermal processor described in Section 2.1.3. During carbonization the pnc-Si membranes are placed inside a graphite susceptor coated with silicon carbide (SiC). Acetylene (C_2H_2) is introduced into the RTP chamber using mass flow controllers for 5 minutes at $700^\circ C$. Argon flush is performed for 5 minutes before and after every carbonization run to remove residual gases from the chamber. The thickness of the carbon layer depends on carbonization temperature and duration. TEM images of the same pnc-Si membrane before and after carbonization are illustrated in Figure 2.7. Carbonization creates a conformal

carbon layer on both sides of the membrane as well as inside the pores. The carbon ring coating pnc-Si pore is shown in high resolution TEM image in Figure 2.8.

2.4 E-beam Metallization

The evaporation is a physical vapor deposition (PVD) method for thin film deposition in a vacuum. During this process, the source material is heated up until it evaporates or sublimates. Evaporation is achieved by resistance heating or electron beam (e-beam) bombardment heating. E-beam heating is preferred in most cases to prevent contamination from the evaporation of the filament material and to increase



Figure 2.9: CHA e-beam evaporation tool.

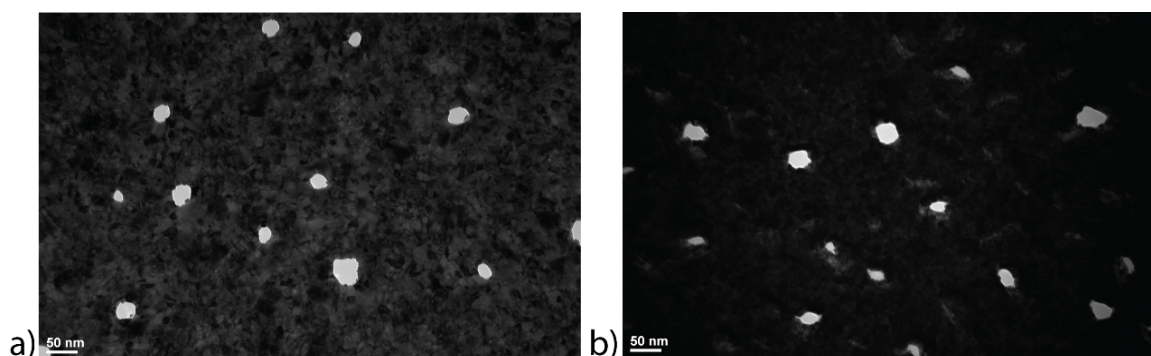


Figure 2.10: TEM micrograph of the 30 nm thick pnc-Si membrane coated on one side (a) and both sides (b) with 15 nm Au/Ti film.

deposition rates. A high current is passed through a wire filament that heats it up to high temperatures and causes a stream of electrons to be emitted from the surface of the filament. The emitted electron beam is directed by a strong magnetic field towards the surface of the evaporation material and is accelerated to high kinetic energies by acceleration voltages on the order of 10 kV. When the beam of electrons hits the surface of the evaporation material contained in a water-cooled crucible, the material melts and vaporizes by produced thermal energy. The vapor is then transferred from the source to the substrate where it condenses and forms a thin film. The main disadvantage of the e-beam evaporation is that it can cause radiation damage to the devices built on the silicon wafer.

The metallization of the pnc-Si membranes with gold (Au) is performed by e-beam evaporation in a CHA e-beam evaporator (Figure 2.9) at base pressures of $10^{-6} - 10^{-7}$ torr. The tool has multiple sockets available for crucibles so that the sequential evaporation of different materials can be performed. Since poor gold adhesion to

silicon requires an adhesion layer, a 3-10 nm layer of titanium (Ti) is deposited first [54]. The 10-15 nm gold layer is deposited next in the same run without breaking the vacuum to prevent Ti layer oxidation. The deposition rates of Au and Ti are 0.5-1 Å/s and 1-4 Å/s, respectively. Deposition rates and film thicknesses are measured by a frequency shift of a quartz crystal microbalance placed inside the chamber during evaporation. Gold films are used in this work to reduce contact resistance problems, caused by the oxidation of other materials at these thicknesses.

The TEM micrographs of a 30 nm thick pnc-Si membrane coated on one side with a 15 nm thick Au/Ti bilayer, and a pnc-Si membrane metallized on both sides are illustrated in Figure 2.10. The total thickness of the membrane metallized on both sides is approximately 60 nm. The pores are not occluded after the metallization. The metallization influence on the pore size distribution is further discussed in Chapter 4.

2.5 Characterization of Pnc-Si Membrane

Such membrane characteristics as porosity, pore geometry and pore size are of chief concern when studying porous materials. The use of transmission electron microscopy (TEM) for pore characterization in pnc-Si membranes is possible due to their thinness (Section 2.5.1). Other methods used to characterize the structure of pnc-Si and pnc-Si based devices are Scanning Electron Microscopy (Section 2.5.2) and Optical Profilometry (Section 2.5.3). A custom image processing technique used to extract

the pore size distributions from TEM images is reviewed in Section 2.5.4.

2.5.1 Transmission Electron Microscopy

Transmission Electron Microscopy (TEM) is an important tool for studying material properties, and is performed by sending a beam of electrons through an ultrathin material in order to form an image. TEM directly captures the crystal structure and defects of the material. The as-prepared and modified pnc-Si membranes are analyzed using a Hitachi 7650 Transmission Electron Microscope at 80 keV (Figure 2.7). The high resolution images of carbonized pnc-Si are taken using a FEI Tecnai F20 TEM (Figure 2.8). The bright field TEM mode is used to obtain images. The nearly circular white areas in TEM images are the open pores. Silicon nanocrystals in the images have different brightness as they differ in crystallographic orientation and thus diffract the incoming electron beam differently. Darker nanocrystals have crystal plane alignment satisfying the Bragg condition [55].

2.5.2 Scanning Electron Microscopy

Scanning Electron Microscopy (SEM) is another electron microscopy technique that is used to obtain information about the pnc-Si membrane structure. Images of both the membrane surface and the cross sections are analyzed. SEM captures the material surface by scanning it with a high-energy beam of electrons. The microscope

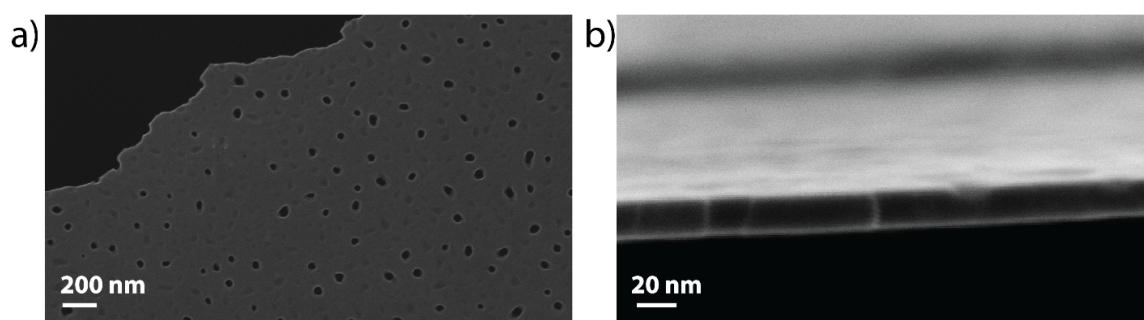


Figure 2.11: SEM micrographs of pnc-Si membrane surface next to the broken edge (a) and the cross section of the pnc-Si membrane used to determine membrane thickness (b).

used to image pnc-Si membranes is a Zeiss Supra 40VP. SEM images reveal open pores and surface nonuniformities (Figure 2.11(a)). We use SEM to observe the pore wall morphology from the rim of a cracked membrane.

Cross-sectional SEM (CS-SEM) micrographs of the pnc-Si membrane in Figures 1.8(b) and 2.11(b) reveal the uniform cylindrical structure of the pore walls [41]. The pnc-Si cross section is realized by breaking the freestanding pnc-Si membrane out of the supporting chip on the metallized silicon wafer surface. The ultrathin membrane adheres strongly to the wafer surface, so cleaving the wafer fractures the pnc-Si membrane. The metallized surface is used to reduce pnc-Si charging during imaging. CS-SEM images are also used for measuring the thickness of pnc-Si membranes before and after the surface modifications.

2.5.3 Optical Profilometry Technique

Optical profilometry is a non-destructive white light interferometry technique that uses the interference of light as a tool to determine the desired information about the surface of an object. White light first passes through a beam splitter and impinges on the sample surface and a reference mirror. Reflected light from both surfaces is then recombined to produce an interference fringe pattern. A series of algorithms are used to process the information, mapping the height of the surface at each point. The result is a surface profile and height variation of the sample with a subnanometer resolution [56]. In this work a Veeco Wyko NT-1100 dynamic optical profilometer is used.

2.5.4 Pore Size Distribution Calculation

A custom image processing program written in MATLAB [57] is used to directly extract pore sizes and distributions from bright-field TEM images (Figure 2.12) [37, 41]. Initially, a background correction is performed on the TEM image for each pixel by subtracting the average value from a surrounding region of a chosen size. Further, a threshold algorithm is applied to the TEM image to create a black and white image (Figure 2.12(b)). The pores are then identified and outlined (Figure 2.12(c)), and statistical information is calculated, including the diameters of the pores, the pore areas, porosity, and the average pore diameter. The area of the pores which

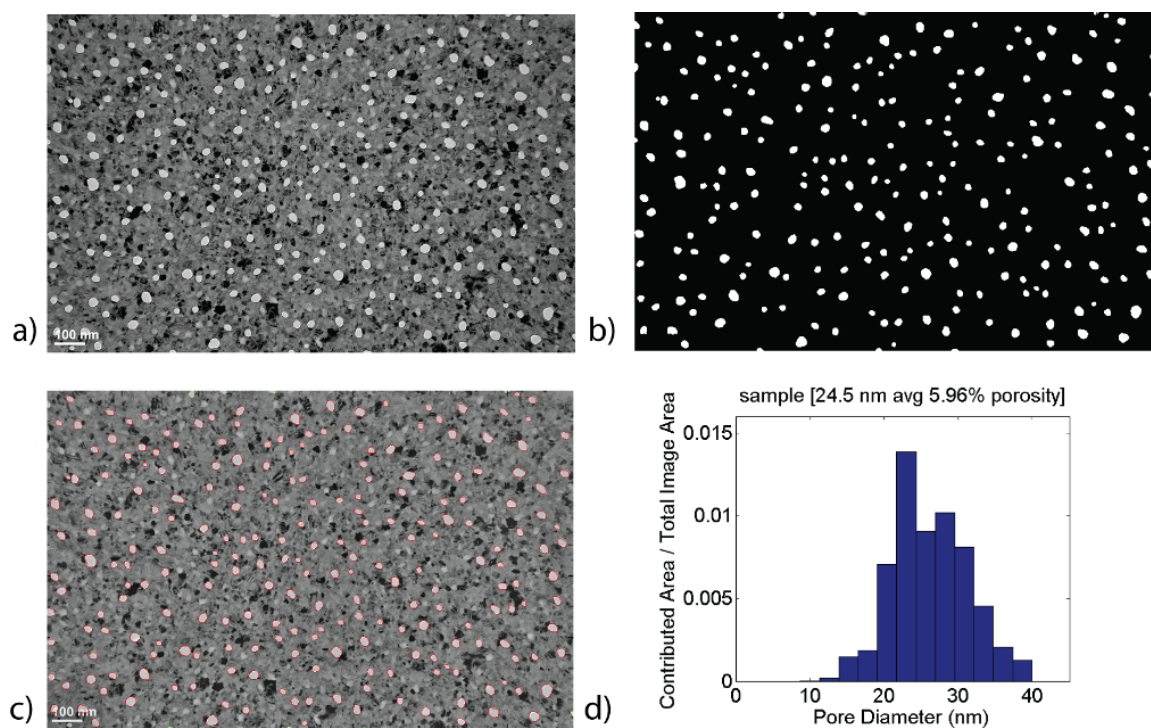


Figure 2.12: Pore processing using TEM image: a) original pnc-Si TEM image; b) black and white image after background correction and applying a threshold algorithm; c) background corrected TEM image with outlined pores; d) pore distribution histogram.

cross the image boundary is included in the porosity calculations, however the areas and diameters are not included in the overall pores statistics. Pore distributions are typically plotted as histograms of the contributed area for each pore diameter (Figure 2.12(d)).

Using a set of ten TEM images (with membrane area $1.7 \mu\text{m}^2$ each) from random areas of the same pnc-Si membrane, the standard errors are calculated. The standard error for the porosity value is 2 % and for the average pore diameter is less than 1 %. These errors are inconsequential and the statistics from one location can be assumed

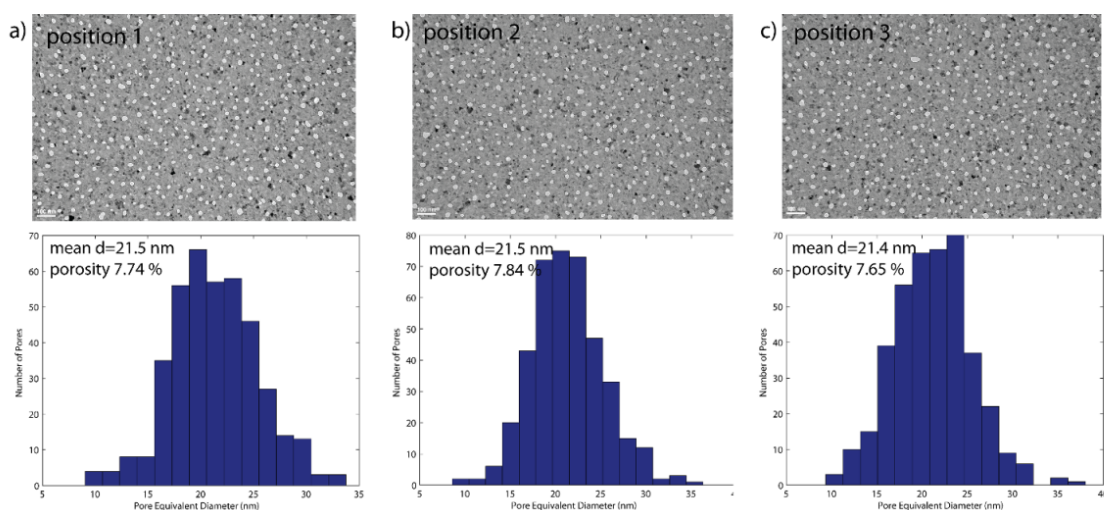


Figure 2.13: Histograms and TEM images from three different positions (from a set of ten) on the same pnc-Si membrane used for standard error calculations. The calculated standard error for the porosity value is 2 % and for the average pore diameter is less than 1 %.

representative for the entire film [41]. An example of the histograms from three different positions on the same wafer is illustrated in Figure 2.13.

2.6 Conclusions

The fabrication process of porous nanocrystalline silicon membranes of typical thicknesses 15 nm or 30 nm, pore diameters ranging from 5 to 80 nm and porosities up to 15 % has been described in this chapter. Pnc-Si membranes with different pore sizes and porosities can be fabricated by changing such manufacturing parameters as annealing conditions and amorphous silicon layer thickness. Rapid thermal carbonization and e-beam evaporation techniques have been used to deposit thin carbon

and metal films on pnc-Si membranes. Transmission electron microscopy, scanning electron microscopy, optical profilometry and image processing software used to determine pnc-Si membranes characteristics and characterize devices built using them have been discussed.

Chapter 3

Gas Flow through Pnc-Si Membrane

A first step in designing nanomaterials and devices for separation and microfluidics applications is understanding how fluid transport works for the particular material, and the interaction between fluid and the pore surface material. This chapter explores how ultrathin pnc-Si membranes achieve high gas transport, and discusses the physics involved.

An introduction to gas transport theory and a review of existing gas flow studies in porous materials are presented in Section 3.1. The permeation measurement setup and performance evaluation of the pnc-Si membrane compared to the existing sieve-like membranes are described in Sections 3.2 and 3.3. In Section 3.4 the dominant gas transport mechanism through the pnc-Si membrane is determined. Gas flow properties of the membrane are studied in Section 3.5 to explore the relative contributions of ballistic flow and wall collisions in membranes with different pore sizes. In Section 3.6

gas flow through carbonized pnc-Si and untreated pnc-Si is compared in order to test whether carbon walls favor specular reflections, as opposed to diffusive reflections in pnc-Si. The conclusions are presented in Section 3.7.

3.1 Background

Many factors are responsible for determining the gas transport mechanism that occurs in a particular porous membrane. Included among these factors are pressure, temperature, material surface and geometrical properties of the pores, as well as the characteristics of the flowing gases. Viscous, free molecular, and the transitional mechanism between viscous and free molecular are known gas transport mechanisms. These mechanisms are characterized by the density of the gas particles flowing through a pore or what is called the degree of rarefaction. The average distance traveled by the molecules between collisions is known as the mean free path λ between gas molecules. At standard conditions, λ is approximately 70 nm for air, 66 nm for nitrogen, 195 nm for helium, and 44 nm for carbon dioxide [58]. The molecular density can be influenced by external stimuli, such as pressure, which can change λ and thus densify or rarefy the gas inside the pore so that different flow regimes can be observed in the same size pores. Different flow regimes can also be observed by changing the pore size at ambient conditions and thus changing the molecular density inside the pore. When a pore opening is much bigger than λ , the flow through such a pore is a continuum

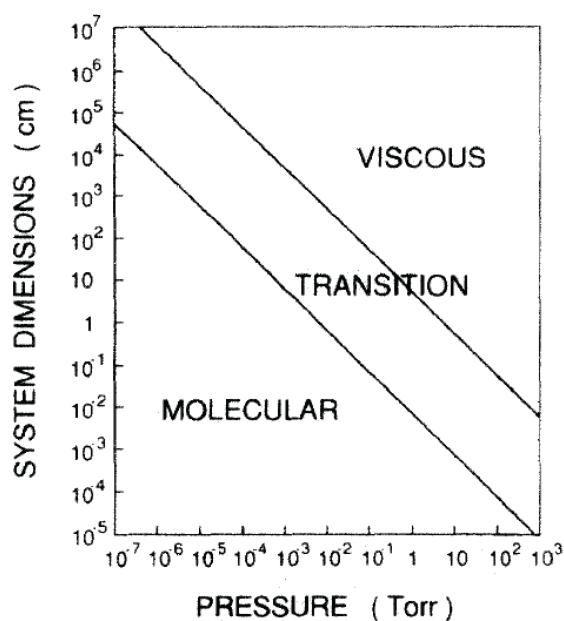


Figure 3.1: Gas flow regimes as functions of system dimensions and pressure [59].

and considered viscous. As the pore dimensions become smaller than λ , the flow is characterized as molecular. Gas flow regimes are illustrated in Figure 3.1.

The criteria for distinguishing between gas flow regimes in the pore are based on the magnitude of the non-dimensional parameter Knudsen number K_n . A Knudsen number is defined as the ratio of the mean free path λ over a characteristic geometric dimension of the system (for example, for a pore diameter d , $K_n = \lambda/d$). For Knudsen numbers $K_n > 1$, a free molecular flow (or Knudsen diffusion) occurs. Transient and viscous flows take place when $0.01 < K_n < 1$ and $K_n < 0.01$, respectively [58, 59].

The kinetic theory of gases is essential for understanding gas transport phenomena in membranes. The theory is based on two fundamental assumptions, namely that gases are made of large number of particles, and that gases are in constant motion

related to their macroscopic properties (temperature, pressure, volume). According to the theory, rapidly moving gas molecules collide with the walls of the enclosing container and exert pressure on them. The ideal gas law, which describes the behavior of gases, is

$$pV = nRT, \quad (3.1)$$

where p is pressure, V is volume, n is number of moles, R is the universal gas constant and T is temperature. Due to gas volume dependence on p and T , comparing gas permeation rates requires that the volume is given at a standard reference point. Standard ambient temperature and pressure (SATP) conditions are a temperature of 25 °C and a pressure of 1 atm. One mole of an ideal gas at SATP occupies $V/n = RT/p=24.8$ liters. At standard conditions (STP) of 0 °C and 1 atm, one mole of ideal gas occupies 22.4 liters.

In the Knudsen diffusion regime, λ exceeds the pore diameter d so that the gas flow is limited by molecular collisions with the channel walls and not by the intermolecular collisions [60, 61]. The analysis of the flow is therefore primarily a geometric problem of determining the restrictive effect of the channel walls on a free flight of a gas molecule. In 1932, Clausing [62] formalized the concept of a transmission probability W as the fraction of incoming gas molecules that pass through a pore without being reflected back. The integral equation that calculates W considers all possible molecule trajectories and decouples the flow into two probabilities: i) the probability

that a molecule will pass the pore without encountering the pore wall, W_{ss} (ballistic component), and ii) the probability of transport through the pore after some collision with the wall, W_{wall} (wall collision component) [62, 63]. The integral equation for W is discussed in Section 3.5. For the ballistic component to become significant, the pore length must become comparable or smaller than the pore diameter. The W values are tabulated for different channel geometries but for many purposes the simple formula is required. The integral equation is approximated for short and long channels, and for a short tube-shaped channel of length L and radius r is given by [58, 61, 62, 7]

$$W = (1 + L/2r)^{-1}. \quad (3.2)$$

The way gas molecules scatter from the wall surface is a fundamental characteristic of Knudsen analysis [64]. The wall collisions are assumed to be diffusive in Knudsen regime, meaning that the angle of reflection of the gas molecule is independent relative to the angle of incidence and is governed by the cosine law. The cosine law defines the probability ds of a molecule that leaves the surface in the solid angle $d\omega$ to form angle θ with the surface normal by Equation 3.3 [65]

$$ds = \frac{d\omega}{\pi} \cos\theta. \quad (3.3)$$

In contrast to diffusive reflections, in specular reflections the angle of incidence of the

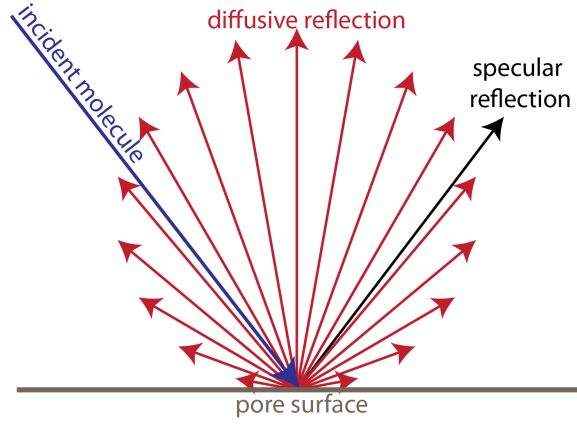


Figure 3.2: Schematic of specular and diffusive reflections.

molecule is equal to the angle of reflection. The concepts of diffusive and specular reflections are illustrated in Figure 3.2.

The interaction between the gas molecules and the channel wall surface in terms of the momentum exchange was formulated by Maxwell for his wall slip boundary condition [66]. The concept of a molecule-wall interaction can be quantitatively described as a function of incident and reflected tangential momentum and is given by the tangential momentum accommodation coefficient σ (TMAC)

$$\sigma = \frac{\tau_i - \tau_r}{\tau_i - \tau_w}, \quad (3.4)$$

where τ_i and τ_r are the tangential momentum of incoming and reflected molecules. The tangential momentum of reemitted molecules τ_w corresponds to that of the wall surface that the molecules impinge on ($\tau_w = 0$ for stationary surfaces). In the case of specular reflections, $\sigma = 0$ and the tangential velocity of the molecules is not

changed. The diffusive reflections ($\sigma = 1$) are a result of complete momentum transfer (or accommodation) during the impact. The tangential velocity is zero after such reflections, indicating that the molecules have lost all information about their pre-collision state [10, 67, 68, 69]. The TMAC value depends on such factors as the nature and pressure of the gas, the material of the wall surface, surface cleanliness, roughness and temperature. These parameters are not completely established since the required experiments and computations are difficult to carry out. Each gas-surface pair has a value of TMAC determined experimentally or by molecular dynamics (MD) simulations [70]. Measuring and analyzing the gas flow through microchannels is one of the experimental methods to find TMAC values [71, 72].

The transport of gases through capillaries of different sizes has been the subject of study for more than a century. The relationships between flow rates and capillary diameters were first established in the pioneering work of Knudsen, Clausen and others [58, 62, 64, 73]. Nanoengineered membranes offer an outstanding opportunity to experimentally verify theoretically predicted transport phenomena. A detailed study of Knudsen diffusion has been done on electrochemically etched silicon nanochannels by Gruener *et al.* for a wide range of Knudsen numbers ($10^2 - 10^7$) and temperatures (40 - 300 K) [74]. Unnikrishnan *et al.* used a nanofabricated membrane to show that gas flux in the transition regime behaves as a linear addition of viscous and Knudsen flows [7], and the conductance of a single nanopore was measured by Savard *et al.* [75].

Nanofabrication techniques also provide means to investigate the nature of molecule-pore wall interactions. Carbon nanotube (CNT) [33] membranes experience enhanced flow relative to the predictions of the Knudsen model [5, 31, 32, 34]. This enhancement has been explained by MD simulations which suggest that fast transport arises due to nearly specular molecular collisions with smooth CNT walls [68, 70, 76, 77, 78], as opposed to diffusive collisions with pore walls in other materials [6, 74]. Depositing carbon on the walls of a template porous membrane and annealing it at a high temperature has been studied as an alternative to CNTs [11, 48, 49, 51, 79, 80]. Cooper *et al.* reported a TMAC value of 0.52 ± 0.1 estimated from transport studies of three gases (argon, nitrogen and oxygen) through carbonized porous alumina membranes with pore diameters 200 nm [79]. TMAC values predicted for CNT are of the order of 10^{-3} [11, 78, 80].

3.2 Permeation Measurement Setup

Experimental measurements of the gas permeance of nitrogen, helium and carbon dioxide are performed using a custom device featuring pnc-Si membranes as in-line filters. A simplified schematic of the setup is illustrated in Figure 3.3. The pnc-Si membrane chips are sealed into a permeation testing block by an O-ring that prevents leaks. N_2 , He or CO_2 are used to pressurize the system upstream of the membrane to a gauge pressure 1 psi while a valve connected to the membrane holder remains

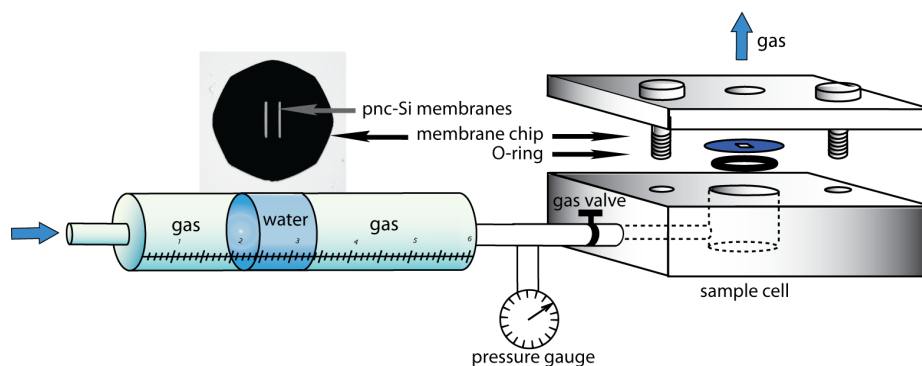


Figure 3.3: Schematic of the gas permeance measurement setup.

closed. The outlet of the setup is open to the atmosphere. In these experiments, a plug of water separates pressurized gas in the ends of a calibrated glass tube (a U-tube with a 1/4 inch inner diameter is used). The space between the water plug and the membrane is filled with the gas of interest. Opening a gas valve allows gas to pass through the membrane. Volumetric flow rates are measured by recording the steady displacement of the water plug through the graduated U-tube for 0.5-5 minutes. A gauge pressure sensor monitors the pressure upstream of the membrane and ensures that this pressure remains ~ 1 psi throughout the experiment. Control experiments with broken membranes give flow rate values at least one order higher than those measured for pnc-Si and control experiments with solid silicon frames without membranes detect no leaks.

The procedure for filling the space between the water plug and the membrane, including an additional plastic tube with two gas valves used for it, is not illustrated in the simplified schematic of Figure 3.3 and is described below. The plastic tube is

connected to different sides of the U-tube through two valves. When all three gas valves are open, the source gas (N_2 , He or CO_2) flows through the setup and an unsealed sample cell to make sure there is no residual air. After all the valves are closed, and the chambers and tubing are filled with the source gas, the pnc-Si membrane is sealed into a sample cell. The procedure is repeated with the pnc-Si membrane in place to push out the air contained between the gas valve shown in Figure 3.3 and the membrane chip. The volume of this air is negligible compared with the volume of the source gas contained in the rest of the setup. The duration of the second step is 5-10 minutes, as the flow rates through membrane chip are slower than through the unsealed sample cell.

The setup is used to test the gas flow rates of commercially available polycarbonate track etch membranes, and the measured values are in agreement with data provided by the manufacturer [3].

3.3 Pnc-Si Membrane Performance

The performance and efficiency of any porous membrane is determined by the fluid permeation rate through it. The permeance P is calculated from the measured volumetric flow (measured gas volume V passed through the membrane per time t)

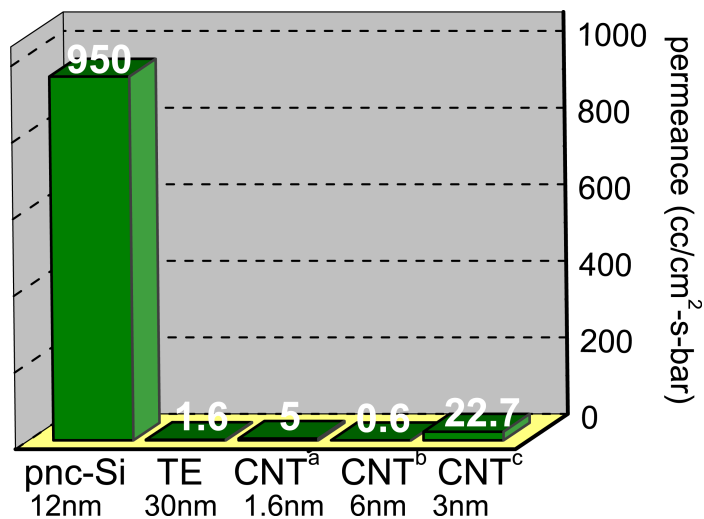


Figure 3.4: Measured N_2 permeances of pnc-Si membrane, polycarbonate track-etched membrane and reported permeance of three CNT membranes (a-[31], b-[5], c-[32]). The pore sizes are indicated in the figure. Experimental values for TE membranes agree with data provided by the manufacturer.

normalized to the membrane area A and the pressure drop Δp

$$P = \frac{V}{At\Delta p}. \quad (3.5)$$

In Figure 3.4 the measured N_2 permeance of pnc-Si membrane with an average pore diameter of 12 nm is compared to the published permeances of CNT membranes [5, 31, 32] and to our measurements of commercially available polycarbonate track-etched membranes [3]. The gas permeance of the ultrathin pnc-Si membrane is several orders of magnitude higher than that of other materials, consistent with permeance measurements in liquids [37].

3.4 Knudsen Diffusion in Pnc-Si

To verify that Knudsen diffusion is the dominant transport mechanism through pnc-Si, N_2 permeance for a large number of pnc-Si membranes with different pore distributions and porosities is measured. In Subsection 3.4.1 the experimental results are compared to theoretically calculated values predicted for each membrane. Additionally, the experimental analysis of the molar mass and pressure Knudsen scaling predictions of the pnc-Si gas permeance is performed in Subsection 3.4.2.

3.4.1 Theoretical and Experimental Pnc-Si Gas Permeance

The expected molecular flow through a single pore is [60, 6]

$$n = \Delta p A_p / \sqrt{2\pi MRT} (1 + L/2r)^{-1}, \quad (3.6)$$

where Δp is the differential pressure in Pa, A_p is the pore area, M is the gas molar mass, R is universal gas constant, T is temperature, L is the length and r is the pore radius. The flow in the molecular regime is defined in Equation 3.6 as the rate at which molecules enter an opening of an area A_p with an adjustment for the restrictions caused by the pore walls. The confining effect of the pore walls on the free flight of the molecules through A_p is introduced by the Clausing factor W (approximated transmission probability) for a short tube-shaped pore: $W = (1 + L/2r)^{-1}$ [7, 58, 61,

62].

To determine the theoretical permeance (P) of a particular membrane, a transmission electron microscope (TEM) image of that membrane is first processed to extract pore size histograms as described in Section 2.5.4. TEM images of pnc-Si before and after pore processing in MATLAB are shown in Figure 3.5(a) [57, 41]. A typical pore size distribution is illustrated in the inset of Figure 3.6. The molecular flow through each pore in the image is calculated using Equation 3.6. The permeance is then calculated by summing the flow rates through the individual pores and normalizing the sum by the pressure drop and the active area of the membrane.

Both experimental and theoretical permeance values for pnc-Si membranes with porosities ranging from 0.1% to 15% and different pore distributions are illustrated in Figure 3.6. The cutoff pore diameters for the tested membranes ranged from 25 nm to 55 nm. Plotting the permeance values as a function of porosity for the tested membranes demonstrates excellent agreement between Knudsen theory and experimental results for individual pnc-Si membranes.

3.4.2 Molar Mass and Pressure Dependencies of Permeance

To further investigate the transport mechanism, the Knudsen scaling prediction that permeance increases with the inverse square root of the molar mass $\frac{1}{\sqrt{M}}$ of the penetrating gas [6, 34] is tested. The solid lines in Figure 3.7(a) connect experimental

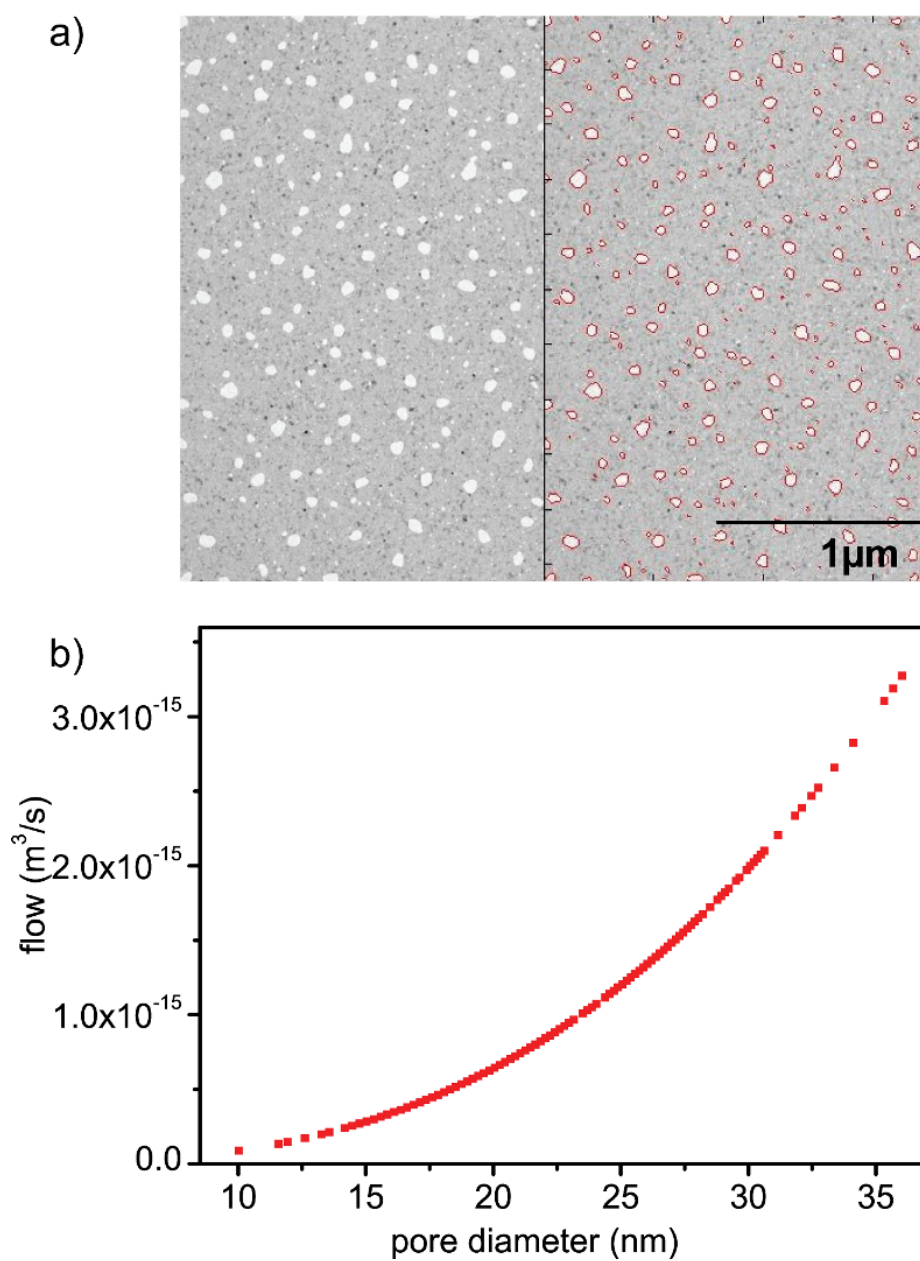


Figure 3.5: Theoretical permeance pore-by-pore calculation: a) TEM image of pnc-Si membrane and the same image with outlined pore edges to find pore statistics, including pore diameters, porosity and pore areas. The image processing is done in MATLAB [57]; b) Pore-by-pore calculation of theoretical gas flow rate through a typical membrane using Equation 3.6 is used to calculate the theoretical permeance of the membrane.

permeance values of the individual tested pnc-Si membranes for N₂, He or CO₂. The linear behavior on the log-log scale shows the power law dependence with an exponent of -0.5 in agreement with the Knudsen scaling prediction.

We also compare the theoretical gas transport selectivity coefficients $\alpha = \sqrt{\frac{M_{gas2}}{M_{gas1}}}$ (0.798 for CO₂/N₂ pair, 0.378 for N₂/He, 0.302 for CO₂/He) to the experimental selectivity α expressed as the ratio of single gas permeances [81, 82] measured under identical conditions for each of the three gas pairs for different pnc-Si membranes. The experimental selectivity is 0.84 ± 0.1 for CO₂/N₂, 0.41 ± 0.05 for N₂/He and 0.35 ± 0.05 for CO₂/He gas pairs. The comparison is illustrated in Figure 3.7(b). The

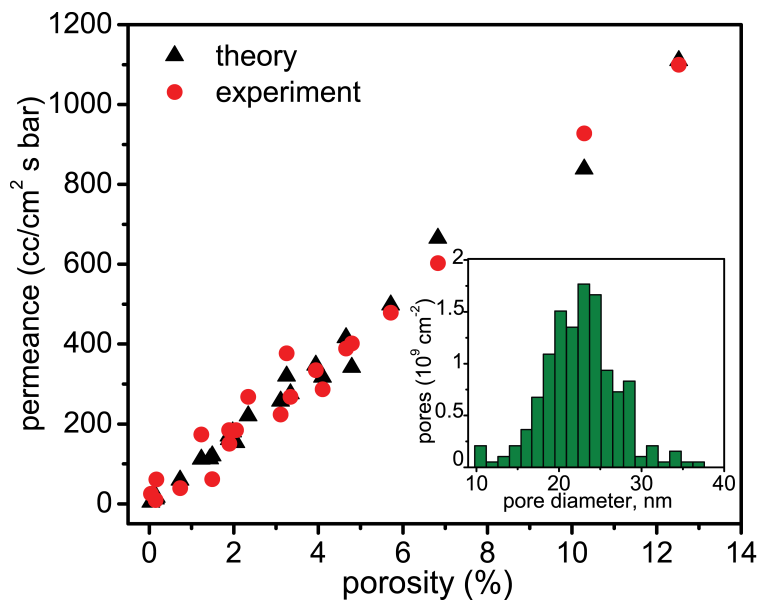


Figure 3.6: Experimental and theoretical N₂ permeance of pnc-Si membranes with different porosities and pore size distributions. The theoretical value for each membrane is calculated by summing the flow rates through individual pores and using the pore distribution histogram. The inset is a typical pore size distribution histogram obtained from TEM measurements.

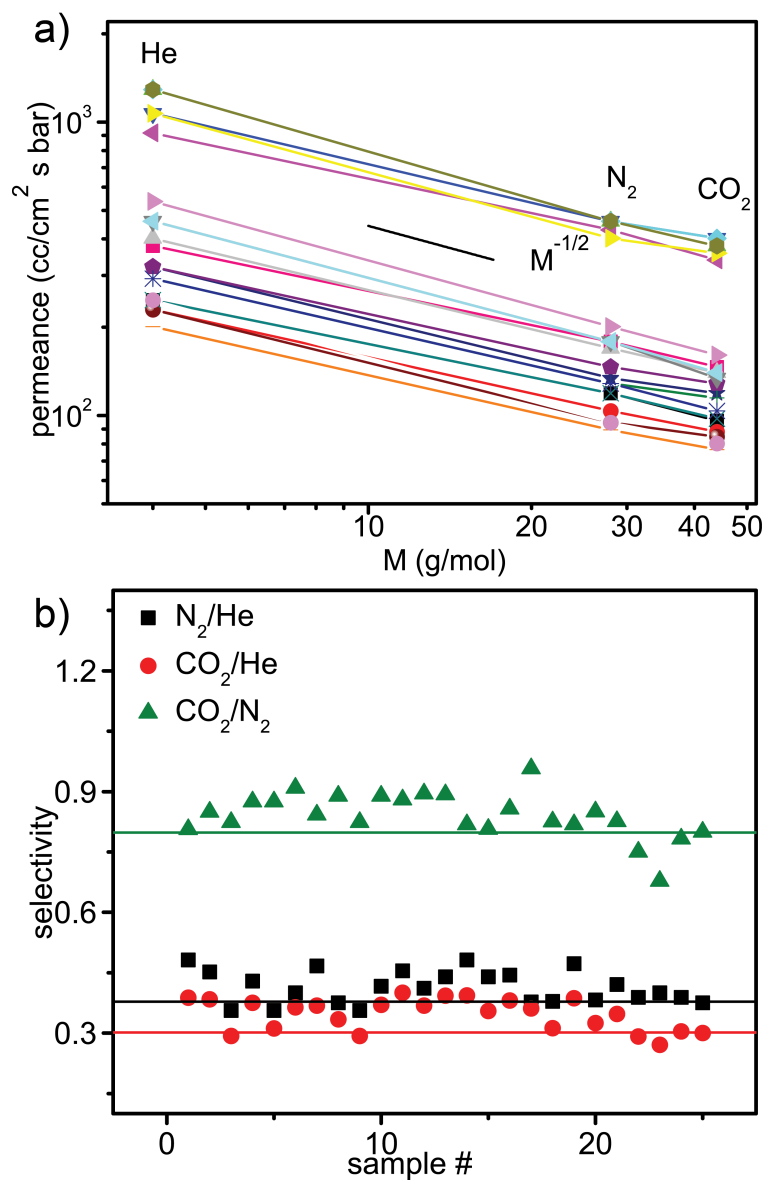


Figure 3.7: a) Measured N₂, He and CO₂ permeance as a function of molar mass M . Lines represent measurements on 22 different pnc-Si membranes, the average slope of fitted lines is -0.45 ± 0.05 . The line of slope $-1/2$ is a guide for the eye. b) The experimental selectivity α of 22 membranes expressed as the ratio of single gas permeances measured under identical conditions for each of the three gas pairs, compared to the theoretical selectivity coefficients $\alpha = \sqrt{\frac{M_{gas2}}{M_{gas1}}}$ (0.798 for CO₂/N₂ pair, 0.378 for N₂/He, 0.302 for CO₂/He).

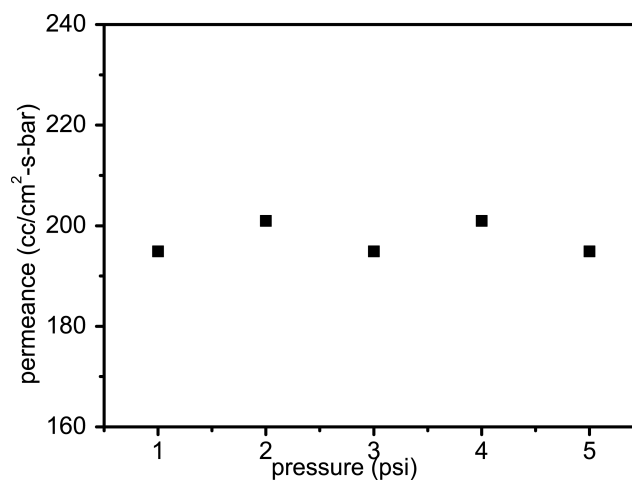


Figure 3.8: N₂ permeance of the same pnc-Si membrane measured at different pressures. Permeance is independent of the pressure suggesting a negligible contribution of viscous flow.

calculated and predicted selectivity values are in agreement within 5-15%.

Finally, the measured permeance is independent of feed pressure, which demonstrated that the contribution of the viscous flow is negligible (Figure 3.8) [81, 83]. The Knudsen selectivity for single gas and mixed gas experiments is identical [34]. It is for this reason that the mixed gas measurements were not performed in this study. The good agreement between the transport experiments and the theory indicates that Knudsen diffusion accurately describes transport through pnc-Si, thus meaning that the molecular collisions with pnc-Si pore walls are diffusive [31, 84, 85].

3.5 Ballistic and Non-Ballistic Gas Flow

In Knudsen regime, the transmission probability of a cylindrical tube of length L is [62, 63]:

$$W = W_{ss}(L) + \int_0^L W_{sr}(x)w(x)dx, \quad (3.7)$$

where the function W_{ss} is the probability of the molecule passing the tube without colliding with the wall (i.e. the ballistic component). The second term in Equation 3.7 (the wall component W_{wall}) represents the probability that a molecule will pass through the pore after colliding with the wall. The function $w(x)$ is defined by the Clausing integral equation

$$w(x) = W_{rs}(L - x) + \int_0^L W_{rr}(x' - x)w(x')dx', \quad (3.8)$$

and equals the flux density striking the wall at position x . The functions $W_{sr}(x)$, $W_{rs}(L - x)$, $W_{rr}(x' - x)$ in Equations 3.7 and 3.8 represent the probabilities that a molecule reflected from the wall at different positions will exit the pore. In detail, $W_{sr}(x)$ is the probability that a molecule after entering the pore will strike it at position x ; $W_{rs}(L - x)$ is a probability that a molecule reflected from the wall at position x directly exits the pore; $W_{rr}(x' - x)$ - probability that a molecule reflected from position x on the pore wall will strike it at another position x' . Letters s and r in the subscripts historically mean *section* and *ring* of the channel, which here refer

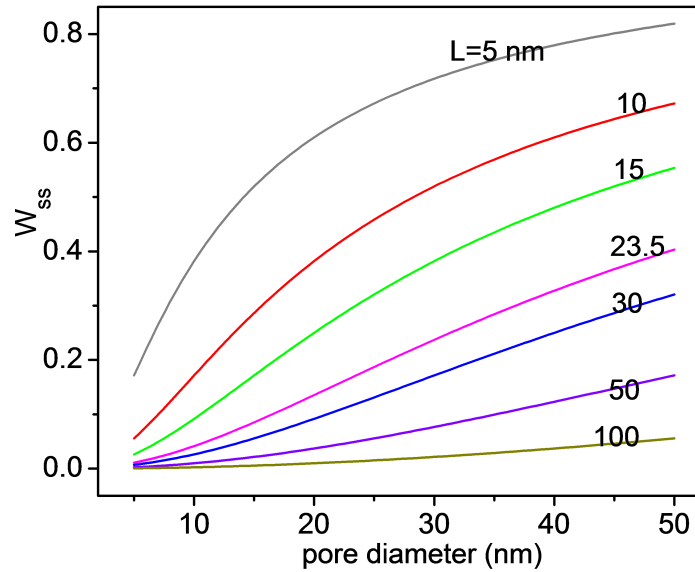


Figure 3.9: Ballistic flow component W_{ss} for pores of different diameters and lengths (Equation 3.9).

to the entrance or exit opening of the pore and the position on the wall, respectively.

The ballistic component $W_{ss}(L)$ is given by a geometric factor [62, 63, 86]

$$W_{ss} = \left(L^2 - L\sqrt{L^2 + 4r^2} + 2r^2 \right) / 2r^2. \quad (3.9)$$

The dependence of the ballistic component W_{ss} on length L and diameter d is plotted in Figure 3.9. The fraction of flow due to molecules with ballistic trajectories increases significantly as pores become wider and shorter. For 15 nm thick membranes, 40 nm pores give $W_{ss} = 0.48$ whereas 10 nm pores give $W_{ss} = 0.09$ [62]. The ballistic component for membranes thicker than 50 nm becomes negligible unless the pores are significantly larger than the membrane thickness. When either the pore size or

thickness approaches the mean free path λ , molecular collisions become more likely and the assumption of molecular flow upon which the Clausing formulations are based is no longer valid.

In order to experimentally determine the W_{ss} and W_{wall} components, we examined the measured flow through pnc-Si and carbonized pnc-Si membranes. C-pnc-Si membranes are formed by depositing a high quality carbon layer on pnc-Si membranes, as described in Section 2.3. The thickness of c-pnc-Si membranes determined by cross-sectional SEM images (details in Section 2.5.2) is 23.5 nm. In Figure 3.10 the experimental and theoretical permeances for five membranes before and after carbonization are compared. The details of the membranes' initial porosities and average pore diameters, and how they changed after carbonization are in the caption of Figure 3.10. The measured permeance values for pnc-Si agree with the theory. While a decrease in porosity and increase in thickness after pnc-Si carbonization result in lower permeance, the experimental results for c-pnc-Si are significantly larger than predicted by Knudsen diffusion, assuming diffusive reflections.

To extract the impact of pore diameter in membranes of different porosities, we divided experimental permeance values by porosity to create a normalized permeance P_{norm} . Porosity of pnc-Si membranes is defined as the percent open area. The P_{norm} values for 15 nm thick membranes with different average pore diameters are

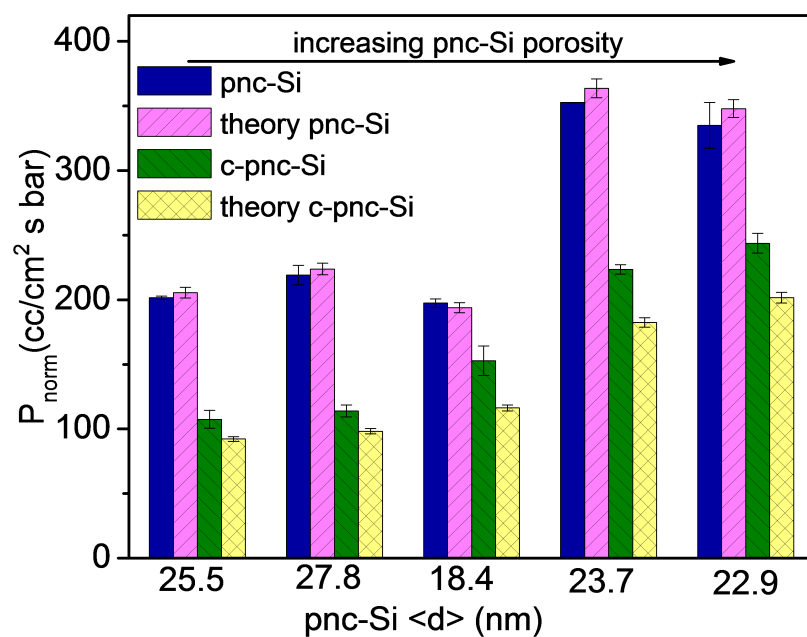


Figure 3.10: Experimental P of pnc-Si membranes from five different wafers before and after carbonization compared to theoretical Knudsen predictions. Initial wafer porosities and average pore diameters from left to right are: 1) 2.5% (25.5 nm); 2) 2.87% (27.8 nm); 3) 3.25% (18.4 nm); 4) 4.97% (23.7 nm); 5) 5.09% (22.9 nm). The corresponding porosities and average pore diameters after the membranes were carbonized are: 1) 1.34% (20.5 nm); 2) 1.3% (21.3 nm); 3) 1.91% (17.1 nm); 4) 2.86% (18.5 nm); 5) 2.87% (20.7 nm).

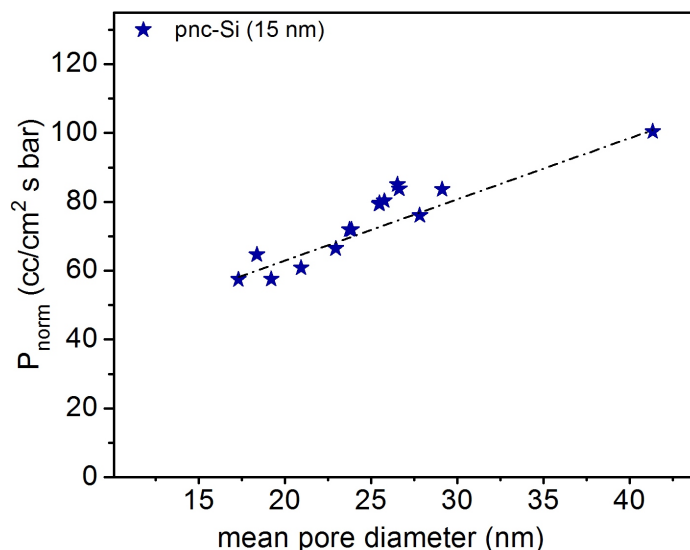


Figure 3.11: Experimental P_{norm} of 15 nm thick pnc-Si membranes plotted against mean pore diameter. The dashed line is added to guide the eye.

plotted in Figure 3.11. In Figure 3.12, to allow the direct comparison of coated c-pnc-Si (solid squares) and non-coated pnc-Si (solid circles) membranes, P_{norm} values for 23.5 nm thick pnc-Si were extrapolated from results obtained for 15 nm pnc-Si using the Clausing factor $W = (1 + L/2r)^{-1}$ [7, 58, 61, 62], which lowered P_{norm} by 12 cc/cm²-s-bar on average. For both pnc-Si and c-pnc-Si, the increase in P_{norm} as a function of average pore diameter seen in Figures 3.11 and 3.12 is due to the increasing contribution of ballistic flow at larger pore sizes as shown in Figure 3.9. To the best of our knowledge this is the first time the ballistic component of the gas flow has been explicitly observed.

3.6 Flow Enhancement in Carbonized Pnc-Si

Flow enhancement at all pore diameters is clearly observed in the carbonized membranes in Figure 3.12. The permeances due to W_{wall} is calculated by subtracting the ballistic component for the corresponding mean pore diameter from the total measured flow. To extract ballistic permeance from the total measured permeance value for pnc-Si the Clausing approximation of transmission probability for a short tube-shaped pore $W = (1 + L/2r)^{-1}$ (Equation 3.2) and the Equation 3.9 for the ballistic component for the corresponding mean pore diameter and thickness of the particular membrane are used. As the flow through c-pnc-Si is not predicted by Knudsen diffusion (Figure 3.10), the W for c-pnc-Si was found by comparing the measured permeance to the theoretical permeance through the same open area in a wall of infinitesimal thickness ($W=1$) [60, 81].

It is found, that the wall component accounts for all the enhancement in the c-pnc-Si flow (open squares in Figure 3.12). The analysis of flow components provides strong evidence that carbonization enhances gas flow by changing the nature of the molecule-pore wall interactions from diffusive to more specular, consistent with the high quality and graphene-like structure observed after high temperature carbonization [11, 48, 49, 51, 52, 79], and with reported flow enhancements in CNTs.

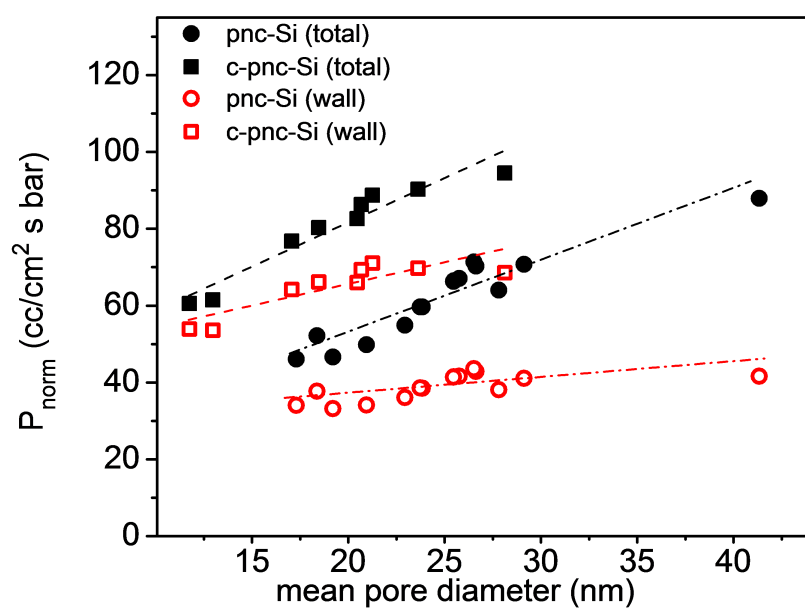


Figure 3.12: Experimental P_{norm} of 23.5 nm thick pnc-Si and c-pnc-Si membranes plotted against mean pore diameter. The wall component of P_{norm} is found by subtracting the calculated W_{ss} component from the total measured P_{norm} . The error in the wall components of P_{norm} due to the pore size distribution is less than 0.5%. The dashed lines are least squares fits.

3.7 Conclusions

In this chapter the gas flow through ultrathin pnc-Si membranes was studied and Knudsen diffusion was identified as the dominant transport mechanism. The demonstrated pnc-Si gas permeance is orders of magnitude higher than in membranes which have similar pore sizes. Two aspects of molecular flow through pores whose diameters and lengths are less than the mean free path of gas molecules were directly observed. First, the significant contribution of the ballistic component to the total permeance of pnc-Si due to the unique geometry of pnc-Si membrane was found. Second, an enhancement in permeance caused by changing the pore wall surface from one that scatters diffusely to one that scatters in a more specular fashion was demonstrated. This enhancement occurred after high temperature carbonization was used to deposit carbon inside the pores of pnc-Si and is consistent with the molecular flow enhancement reported in carbon nanotubes.

Chapter 4

Chemical Capacitive Sensing Using Pnc-Si Membrane

The integration of nanoscale materials into electronic devices such as sensors adds important functionality. Examples include using conductive nanoparticle agglomerates [87, 88] and carbon nanotubes [89, 90] as electrodes in electrical sensor devices to enhance mass transport characteristics [91, 92]. The study of nanopore transport mechanisms [6, 37, 41] and comparisons to ionic channels in the cell membranes have led to interesting chemical and biosensing applications, including single molecule detection [18, 93, 94] and DNA sequencing [17, 19].

Using ultrathin pnc-Si membranes metallized with gold as flexible conductive electrodes in chemical capacitive vapor sensor simplifies the conventional parallel-plate design. The highly permeable porous membrane allows fast analyte vapor permeation to the underlying chemically sensitive layer. The basic principles of electrical sensors used for chemical detection are presented in Section 4.1. In Section 4.2, the

fabrication of a hybrid polymer/pnc-Si capacitive sensor is discussed. The mechanical stability and elasticity of pnc-Si are discussed in Section 4.3. The optical and electrical detection of solvent vapor permeation by the sensor are described in Sections 4.4 and 4.5, respectively. Finally, the conclusions are highlighted in Section 4.6.

4.1 Electrical Sensors Background

Chemical sensors are measurement devices that use chemical reactions to detect and quantify specific analytes [95]. The basic components of the sensor are a transducer element and a sensing or receptor layer. Sensors that convert information about chemical changes inside materials during analyte absorption to electronic signals are based on several electrical transduction principles. Among the different types of electrical transducers are capacitance-based transducers that detect changes in dielectric properties or thickness of the receptor material [96, 97, 98], resistance-based transducers that monitor changes in resistance [99], and mechanical oscillators that respond to changes in mass [100]. Capacitive sensors are preferred over other transducers because of their high sensitivity, low power consumption, lack of mechanical parts, and relative ease of fabrication [96, 101, 102].

Polymers are widely used as receptor materials in chemical capacitive sensors since they are low cost, mechanically and chemically stable, have a great variety of physical and chemical properties, and chemical diversity for the selective detection of

gas and vapor molecules [95, 103, 104]. Polymer properties can be tuned for specific applications by making chemical modifications to the side groups attached to the polymer backbone. Polymeric film can be prepared either by direct polymerization on the substrate surface or by coating the surface with the prepared polymer. Common polymer deposition and coating methods include spin coating, drop coating, spray deposition, and deposition from a vapor phase [95].

The selective absorption of the analyte vapor molecules by the polymer results in reversible swelling or a change in electrical properties, which alters the sensor capacitance as a function of analyte concentration. The capacitance of the sensor increases (decreases) as the analyte is absorbed into the polymer to change its permittivity (thickness). The sensing principle of a capacitive sensor is based on the capacitance relationship of a parallel-plate capacitor, which is

$$C = \frac{\epsilon_0 \epsilon_r A}{d}, \quad (4.1)$$

where ϵ_0 is the permittivity of vacuum, ϵ_r is relative dielectric constant of the dielectric layer, A is the overlap area between two plates, and d is the separation between the plates. The capacitance changes in response to ϵ_r or d . The effects of polymer swelling ($d + \Delta d$) and change of dielectric constant ($\epsilon_r + \Delta \epsilon_r$) may cancel each other. To maximize the capacitive response, the polymer and solvent are chosen so that one of these mechanisms is dominant.

When analyte vapor is brought into contact with a polymeric material, it will be partially absorbed by the polymer until a concentration equilibrium in both phases is reached. The key parameter describing this absorption process is the partition coefficient K_c , defined as the ratio of the concentration of the vapor in the polymer C_p to its concentration in the gas phase C_g at equilibrium, and is given by [102]

$$K_c = \frac{C_p}{C_g}. \quad (4.2)$$

The amount of the vapor absorbed in the polymer is proportional to the vapor concentration in the gas, similarly to the Henry's law that describes gas absorption by liquids. Partition coefficients for the specific polymer/analyte pairs are determined experimentally, using linear sensor responses obtained by quartz crystal microbalance (QCM) or surface acoustic wave sensors (SAW). Also, K_c and the interactions between absorbing polymer and analyte can be modeled using linear solvation energy relationships (LSERs). Another approach is K_c calculation using Hilderband solubility parameters [102, 105, 106].

The absorption process depends on the ambient conditions and the physical state of the polymer. Polymers change their state from rubbery to glassy depending on the temperature relative to the glass transition temperature T_g of a particular polymer. Below T_g , polymers are in glassy state, and in a rubbery state above the T_g value. The absorbed molecules change the T_g value. The diffusion of absorbed molecules

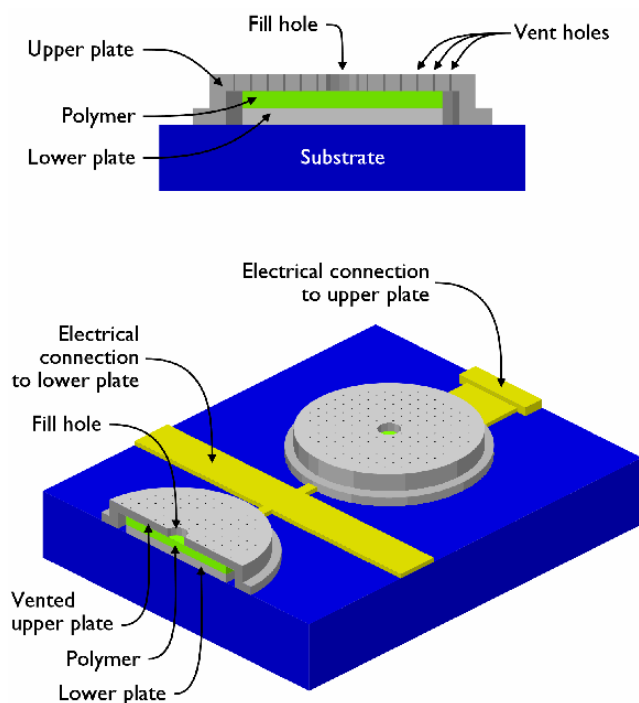


Figure 4.1: Cross-sectional and top schematics of the parallel-plate capacitive sensor geometry [108].

into the polymers is different for polymers in glassy and rubbery states, and is faster in the latter [107]. The rubbery polymers are therefore preferred in chemical sensing.

The degree of interaction between materials is characterized by the Hildebrand solubility parameter $\delta = \sqrt{c}$, where c is the cohesive energy density. The cohesive energy density of the polymer is the amount of energy required to break all attractive interactions between chains in a unit volume of the material [109]. The swelling behavior of the polymer in a particular solvent can be predicted by comparing the solubility parameters of the polymer δ_p and solvent δ_s . The swelling of the polymer in the solvent is maximized as $(\delta_p - \delta_s)^2$ approaches 0, meaning that the solvent

molecules can penetrate through the polymer chains by overcoming the attraction between them [110].

Capacitive sensors have two typical geometries: parallel-plate electrodes and interdigitated electrodes (IDE). The parallel-plate sensor has a polymer layer sandwiched between two electrodes. The top electrode in the parallel-plate geometry must be porous in order for the analyte to reach to the underlying receptor layer during sensor operation. Etching voids in a top metal layer is challenging because the metal etchants can destroy the polymer deposited under the metal layer. One solution is to create a parallel-plate MEMs structure with an etched porous electrode on top of the silicon wafer, and then infiltrate the polymer later as depicted in Figure 4.1. Such a process, however, requires sophisticated fabrication steps [96, 108, 111, 112].

The IDE sensor consists of two comb-shaped metal electrodes on a substrate and a sensitive polymer layer deposited on top of them as illustrated in Figure 4.2 [101, 102, 113]. The majority of the electric field lines between electrodes in the IDE sensor is contained within the polymer layer with thickness equal to half of the center-to-center spacing between the IDEs. To improve sensitivity of IDE sensors to changes in dielectric properties and to increase the number of electric field lines within the polymer layer, the electrodes can be built on two different metal layers of the CMOS process [114].

IDE sensors are easier to fabricate but they suffer from lower sensitivity because

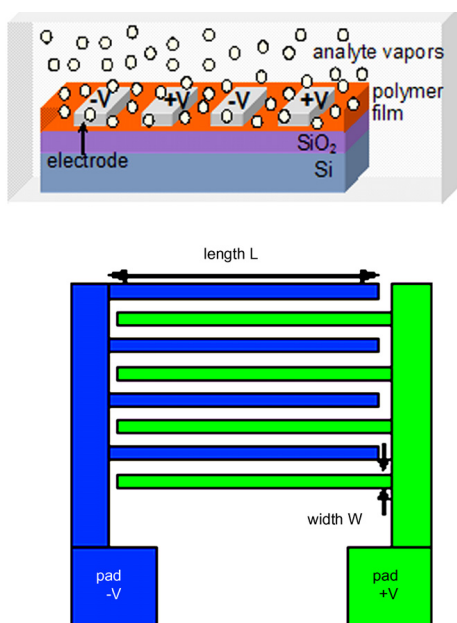


Figure 4.2: Cross-sectional and top images of interdigitated electrodes based capacitive sensor [101].

only a fraction of the polymer layer on top of the electrodes contributes to the sensing signal, while the entire polymer layer contributes to the signal sensitivity in parallel-plate sensors. The parallel-plate sensors, on the other hand, have longer response time associated with slower vapor exchange. In such sensors, the vapor molecules have to penetrate through the openings in the metal electrode to reach the polymer, and the amount of polymer surface area for vapor adsorption is less [96].

4.2 Pnc-Si Membrane Capacitive Sensor

The use of a molecularly thin nanoporous pnc-Si membrane as an analyte-permeable electrode in capacitive sensing, and metallization influence on the pore characteristics are discussed in Section 4.2.1. Capacitive sensor fabrication is described in Section 4.2.2.

4.2.1 Pnc-Si Membrane as a Porous Electrode

To overcome the existing difficulties and in making a parallel-plate sensor structure, a capacitance sensor that uses a metallized ultrathin porous nanocrystalline silicon membrane as a permeable electrode was designed [12, 39]. The use of pnc-Si membrane as analyte-permeable sensor electrode adds the ability for selective access of the analyte molecules to the receptor, and gives control over the mass transport between receptor and sensor environment. The high gas permeation rates through

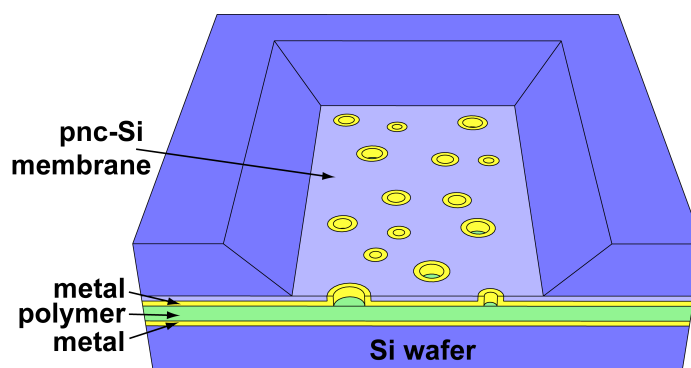


Figure 4.3: Schematic of the pnc-Si membrane based chemical capacitive sensor.

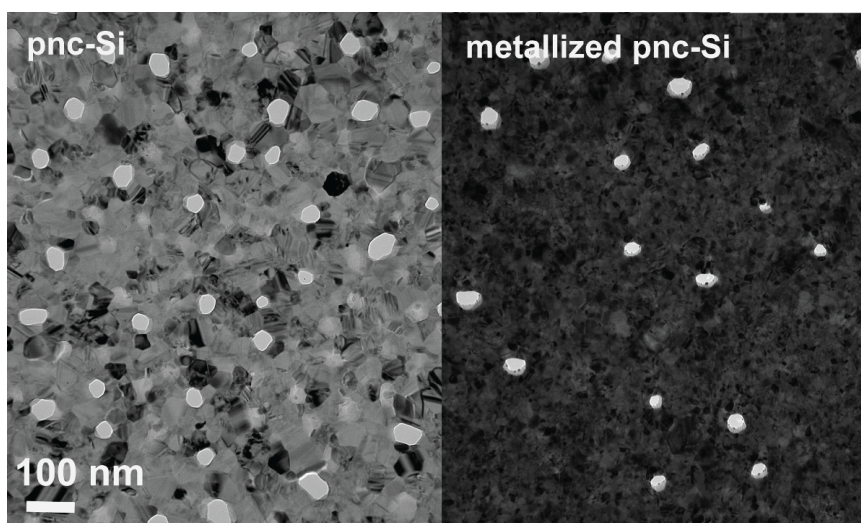


Figure 4.4: TEM images of the same 15 nm thick pnc-Si membrane before and after metallization with 15 nm Ti/Au bilayer demonstrate that pores have not been occluded.

pnc-Si membrane discussed in Chapter 3 and high membrane porosity address the vapor exchange problem in parallel-plate capacitive sensors. In addition, the silicon platform also provides for convenient chemical modifications [52]. The schematic of the sensor with metallized pnc-Si electrodes is illustrated in Figure 4.3.

The metallization of pnc-Si is performed by e-beam evaporation of titanium and gold described earlier in Section 2.4. TEM images of a pnc-Si membrane before and after 15 nm thick metal deposition shown in Figure 4.4 demonstrate that Au/Ti bilayer deposition closes small pores and reduces the diameters of the larger pores. For example, deposition of a 13 nm metal bilayer on two different 15 nm thick pnc-Si membranes caused the porosity to drop from 4.8 to 3.3 % and from 13.4 to 6.2 %. The corresponding average pore size reductions were from 19 nm to 15.5 nm and from

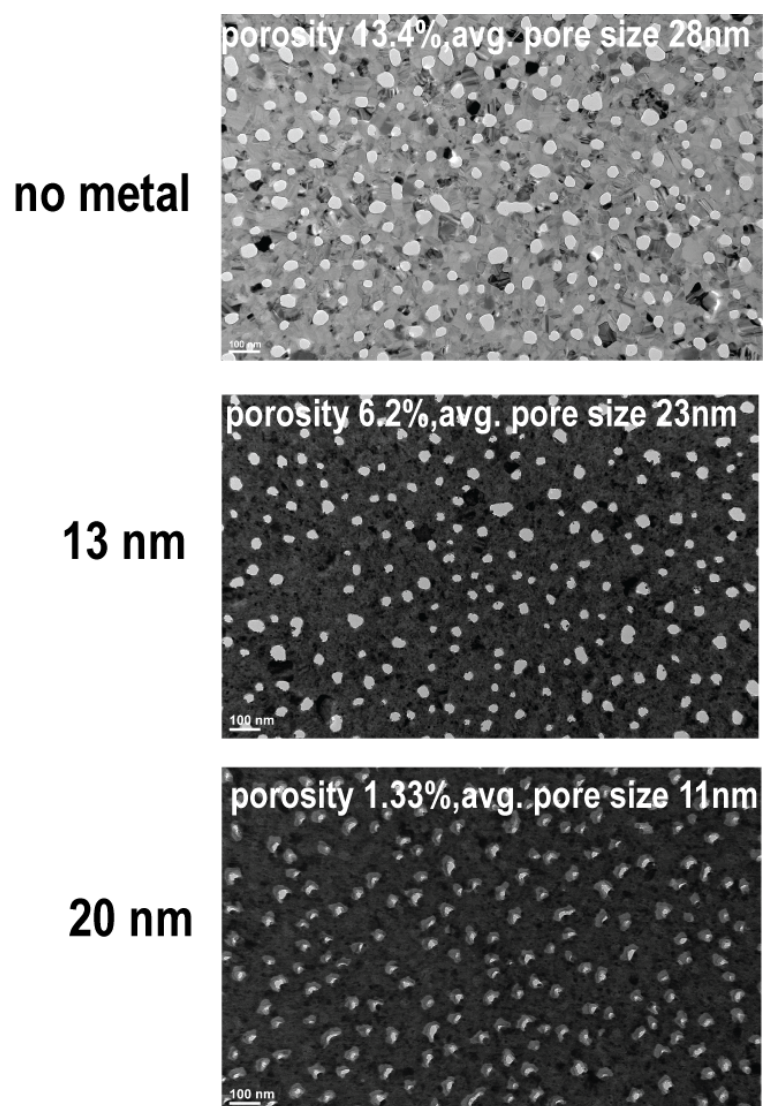
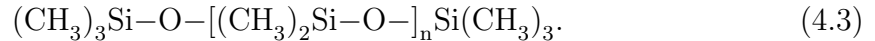


Figure 4.5: TEM images of the same 15 nm pnc-Si membrane with no metal, 13 nm, and 20 nm metal layers deposited on top. The image shows how porosity and average pore diameter of pnc-Si membranes change with the deposited metal thickness.

28 nm to 23 nm. The porosity and pore size distribution of pnc-Si membranes change with the deposited metal thickness, as shown in Figure 4.5.

4.2.2 Pnc-Si Membrane Capacitive Sensor Fabrication

Sensor fabrication begins with metal deposition on top of both the pnc-Si membrane and the silicon wafer chip, followed by sensing polymer deposition [12, 39]. In this work, polydimethylsiloxane (PDMS), which is a silicon-based polymer also known as silicone, is used as a sensing material. The chemical formula of PDMS is [115]



A fundamental property of silicones is the presence of a Si–O backbone with functional groups attached to the silicon atom. In PDMS the functional groups are methyl groups (Si–CH₃), which make the material hydrophobic. Methyl groups are converted into silanol groups (Si–OH) by using O₂ plasma treatment. The plasma treatment makes the PDMS surface temporarily hydrophilic and facilitates strong adhesion between the PDMS and glass substrates when the bonding is done immediately after the treatment. This technique is often used in microfluidic technology for PDMS based devices fabrication [115]. PDMS is a nontoxic, easy to process and widely available polymer with many attractive physical properties including transparency, electrical insulation and inertness [116].

The polydimethylsiloxane (PDMS) layer was created using a Sylgard 184 silicone elastomer kit obtained from Dow Corning, which contains a pre-polymer base and

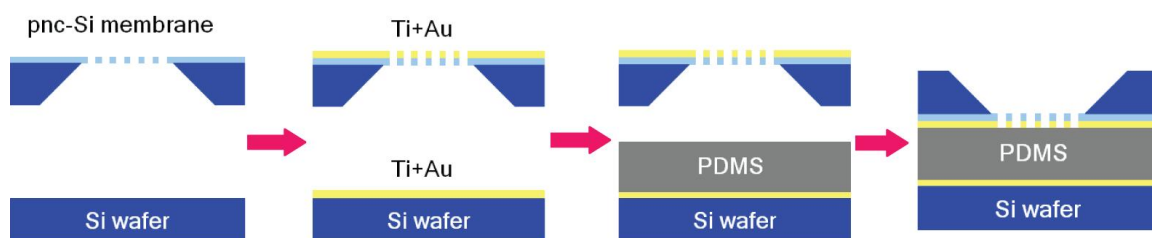


Figure 4.6: Fabrication steps of chemical capacitive sensor based on pnc-Si membrane: metal deposition, PDMS spin-coating, bonding and PDMS curing.

a curing agent. The pre-polymer was first mixed with its curing agent in a 10:1 ratio by weight, and then placed in a desiccator to remove the bubbles created while mixing. The vinyl-terminated pre-polymer base and methyl-terminated curing agent are crosslinked during mixing and a final high temperature curing step. The mix ratio of the base and curing agent was shown to influence the degree of PDMS swelling in chloroform as a result of the different crosslinking densities. Higher crosslinking density restricts swelling of the polymer network [117].

The PDMS layer was created by spin-coating the prepared mixture on the silicon chip. After the mixture of the pre-polymer base and curing agent was poured on the silicon chip, it was spun at 4000-6000 rpm for 1-4 min. As a result of spinning, the polymer solution spread on the surface and formed a uniform thin film. The thickness of the resulting PDMS film ranged from 5 to 10 μm depending on the spin rate and duration. The pnc-Si membrane chip and PDMS covered silicon chip were then bonded together to form the sensor (Figure 4.3). Lastly, the resulting sensor structure is cured at 95 $^{\circ}\text{C}$ for 2 hours to finalize the crosslinking process [12, 39].

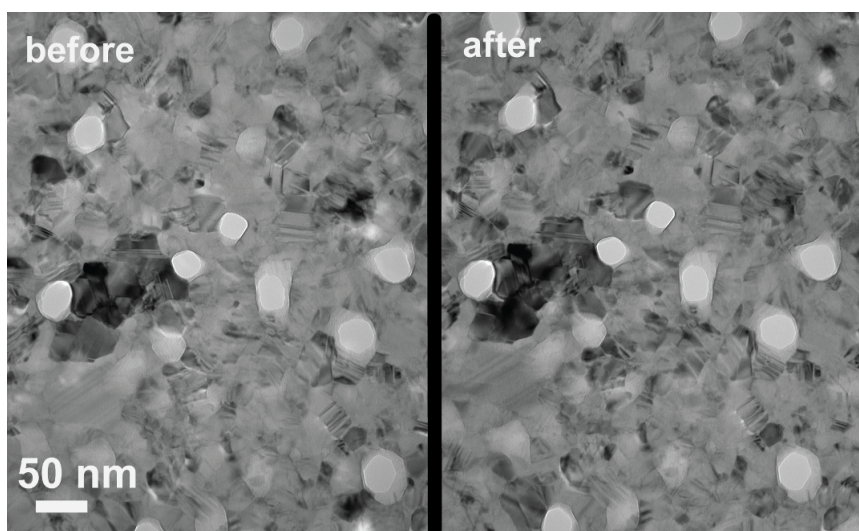


Figure 4.7: TEM images of the same pnc-Si membrane before and after repeatable stretching at 15 psi. After the imaging, the membrane burst pressure was measured to be 16 psi. The images show that the positions of the nanocrystals and the pores stay unchanged after stretching.

Sensor fabrication steps are illustrated in Figure 4.6. Following fabrication, conductive silver epoxy obtained from MG Chemicals was used to connect wires to the sensor electrodes. The epoxy was air dried for approximately 24 hours.

4.3 Mechanical Stability of Pnc-Si Membrane

Unlike in nanocrystalline metals where the mechanical properties are observed using *in situ* imaging techniques, the mechanical properties of nanocrystalline covalently bonded materials, such as nanocrystalline silicon (nc-Si), has not been extensively studied. Computer simulations are typically used to explain the mechanical behavior and plasticity of nc-Si [118, 119].

Mechanical stability and flexibility are important electrode properties for swelling-induced sensors. Using a custom pressure cell to seal pnc-Si membranes with an O-ring described in Section 3.2, the burst pressure of the pnc-Si membranes was tested. Nitrogen was used to pressurize the system upstream of the membrane and a gauge pressure sensor monitored the increasing pressure throughout the experiment. The average burst pressures of the pnc-Si membranes strongly depended on their fabrication conditions. The measured average burst pressures range from a few psi up to 25 psi.

The mechanical stability of pnc-Si membranes was previously studied by applying pressure to one side of the membrane, and observing the deformation during pressure application using an optical microscope. It was reported that pnc-Si membranes elastically and reversibly deform when pressurized [9]. To confirm this result at the nanoscale level, we applied pressures just below the burst pressure across pnc-Si for 30 min, and examined the membranes using TEM. The pores in pnc-Si serve as markers, making it possible to image the same areas of the membrane before and after mechanical testing. TEM images of the same area in the middle of the $200\ \mu\text{m} \times 200\ \mu\text{m}$ pnc-Si membrane before and after repeatable stretching under 15 psi are shown in Figure 4.7. As seen in the TEM images, the positions of the nanocrystals and the pores are unchanged, meaning that pnc-Si membranes do not exhibit plastic deformation under extreme pressures for the material. The burst pressure of the membrane illustrated in Figure 4.7 measured after the TEM imaging is 16 psi [12].

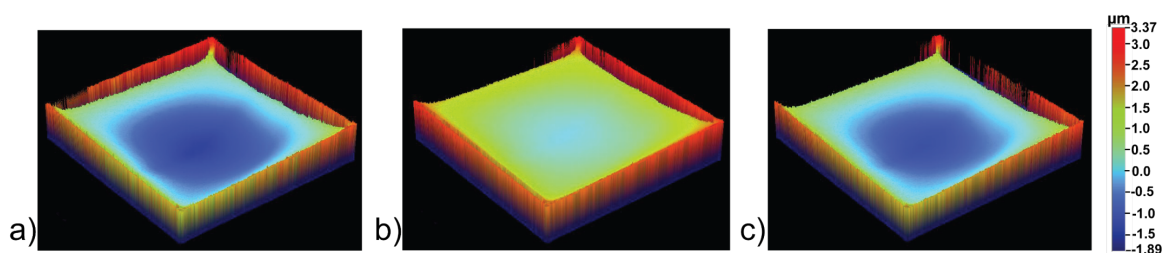


Figure 4.8: 3D optical profilometry images of a pnc-Si/PDMS/Si structure taken from well-side of the pnc-Si membrane: a) before exposure to xylene vapor; b) immediately after exposure to xylene vapor; c) approximately 2 minutes after the xylene vapor is removed. The wall-like area around the membrane window is an artifact of the imaging as the optical profiler picks up the signal reflected not only from the square membrane area but also from the walls of the silicon well which was etched to expose the freestanding pnc-Si membrane. The results show that xylene vapor permeates through the membrane and reversibly changes PDMS thickness.

4.4 Pnc-Si deflection during PDMS swelling

Because pnc-Si membranes are very thin, their resistance to flow is very small as shown by the high measured permeability values in Chapter 3. To determine if the analyte vapor above the membrane permeates through the membrane and reaches the polymer beneath it, we conducted an experiment on the pnc-Si/PDMS/Si wafer structure to monitor reversible changes in the PDMS thickness in xylene vapor [12, 39]. The sensor was exposed to xylene vapor and the change in the surface height before and after exposure was measured. The technique used to measure the induced swelling of the pnc-Si/PDMS/Si structure is optical profilometry and has been described in Section 2.5.3.

The deflection of a pnc-Si/PDMS/Si structure was observed before, during and after exposure to xylene vapor. The 3D optical profilometry images of the structure

taken from the well-side of the pnc-Si membrane are shown in Figure 4.8. The square window area in these images is the pnc-Si membrane covering the PDMS layer. The surface height is represented by the color scale. Xylene vapor permeation through the pores induced PDMS swelling under the pnc-Si membrane. A $0.38\ \mu\text{m}$ increase in the thickness of the initial PDMS layer was measured when vapor was introduced into the system. The swelling was reversible: after the vapor source was removed the membrane came back to its initial state as shown in Figure 4.8c [12, 39].

4.5 Chemical Capacitive Sensing

The electrical characterization of the pnc-Si-based sensor is presented in this section. Capacitance measurement setup is described in Section 4.5.1. The capacitive responses of the sensor to three solvent vapors (hexane, toluene, acetone) and to controlled concentrations of the xylene vapor are presented in Sections 4.5.2 and 4.5.3, respectively.

4.5.1 Capacitance Measurement Setup

A schematic of the setup used to measure the sensor response is illustrated in Figure 4.9. A HP4275A multifrequency LCR meter controlled by Labview was used to measure the capacitance of the completed sensor. The sensor capacitance was

continuously sampled using a National Instruments GPIB-USB interface. All measurements were done in the parallel capacitive mode, with an AC signal of 10 kHz and voltage amplitude of 100 mV. The sensor chip was connected to the LCR meter with the backside well facing up to ensure vapor permeation through the porous membrane. The sensors were then placed in a sealed 3.8 L glass container. Real-time data was collected during solvent introduction. A pipette was used to inject a known concentration (parts per million, ppm) of liquid solvent (hexane, toluene, acetone, xylene) into the glass container which was then allowed to evaporate. An immediate change in capacitance was observed. The sensor was then taken out or flushed with air for few minutes to allow the capacitance to regain its original value, and then exposed to solvent vapor again. This procedure was repeated several times.

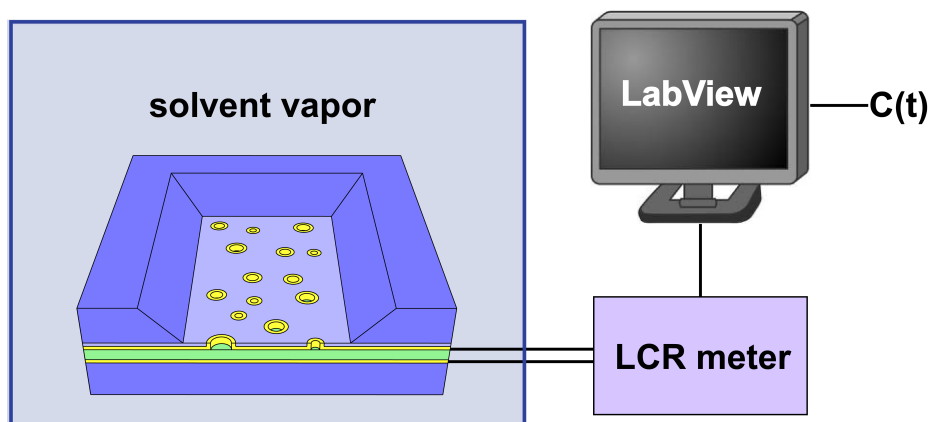


Figure 4.9: Capacitance measurement setup.

4.5.2 Detection of Different Solvent Vapors

As mentioned before, the sensing principle of a capacitive sensor is based on the relationship $C = \epsilon_0 \epsilon_r A/d$ (Equation 4.1), which shows that the effects of polymer swelling ($d + \Delta d$) and the change of the dielectric constant ($\epsilon_r + \Delta \epsilon_r$) detected by the sensor may cancel each other. Test solvents, including hexane, toluene, and acetone, were selected for this experiment as they are readily available, quick to evaporate and induce only one of these two changes in PDMS. For hexane and toluene the polymer swelling dominates, while for acetone vapor the dielectric constant change dominates [110]. The solubility parameters of PDMS and test solvents used in experiments are $\delta_{PDMS}=7.3 \text{ cal}^{1/2}\text{cm}^{-3/2}$, $\delta_{hexane}=7.3 \text{ cal}^{1/2}\text{cm}^{-3/2}$, $\delta_{toluene}=8.9 \text{ cal}^{1/2}\text{cm}^{-3/2}$, $\delta_{acetone}=9.9 \text{ cal}^{1/2}\text{cm}^{-3/2}$. The dielectric constants of PDMS and solvents are $\epsilon_r_{PDMS}=2.75$, $\epsilon_r_{hexane}=1.89$, $\epsilon_r_{toluene}=2.34$, $\epsilon_r_{acetone}=21$ at T=293-296 K [120].

The experimental capacitance data upon exposure of the same sensor to different vapors is shown in Figure 4.10. The sensor was repeatedly exposed to hexane and then toluene vapor at the 800 ppm and 1000 ppm levels respectively. During exposure, the sensor capacitance was allowed to reach a stable value. Between exposures the sensor was removed from the container and allowed to recover. Both solvents swelled the PDMS leading to an increase in plate separation and capacitance decrease. Hexane swells PDMS more than toluene, which is expected given their different solubility

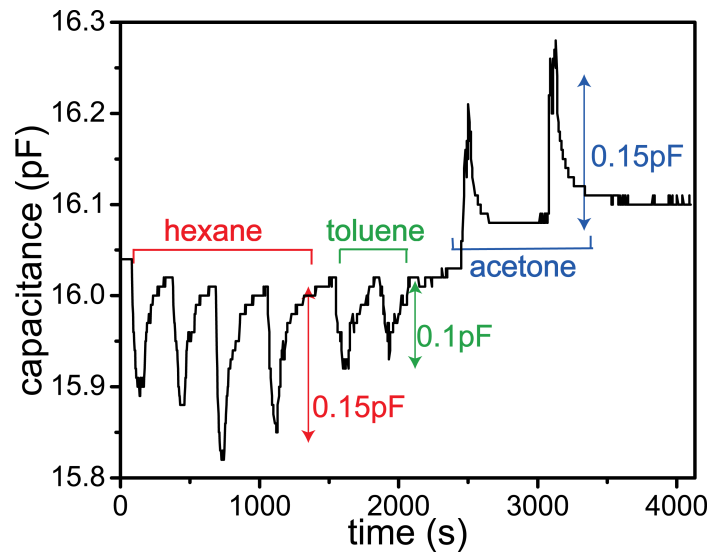


Figure 4.10: Capacitive response of the sensor upon exposure to hexane, toluene and acetone vapors.

parameters δ ($\delta_{PDMS} = \delta_{hexane} < \delta_{toluene}$) and measured swelling ratios [110]. The ϵ_r of hexane and toluene are close to that of PDMS and the net change in ϵ_r is negligible. The measured changes in capacitance induced by hexane and toluene were 0.15 pF and 0.1 pF, respectively [12, 39].

To explore the sensor response to changes in dielectric constant of the sensing layer, the sensor was exposed to acetone vapor. For acetone ϵ_r is much higher than for PDMS resulting in an increase of the sensor capacitance by 0.15 pF upon acetone exposure and absorption. By contrast, PDMS swelling induced by acetone is negligible with the swelling ratio equal to 1.06, although other solvents with very similar solubility parameters as acetone swell PDMS much more. This observation is explained by the solvent polarity [110].

4.5.3 Solvent Vapor Concentration Detection

Figure 4.11 shows a typical sensor response upon exposure to different xylene vapor concentrations (100, 200, 300, 400 ppm). After each exposure the sensor was brought to its original value by exposure to air. The response and recovery times of the sensor are functions of pore size and porosity, and decrease with increasing pores size, as bigger pores facilitate vapor molecule diffusion into and out of the sensor [121].

These chemical sensing results suggest that our sensor performance is comparable to similar polymer-based capacitive sensors, and that it can detect solvent vapor concentrations well below 100 ppm within seconds [96, 101, 102, 111, 112]. With

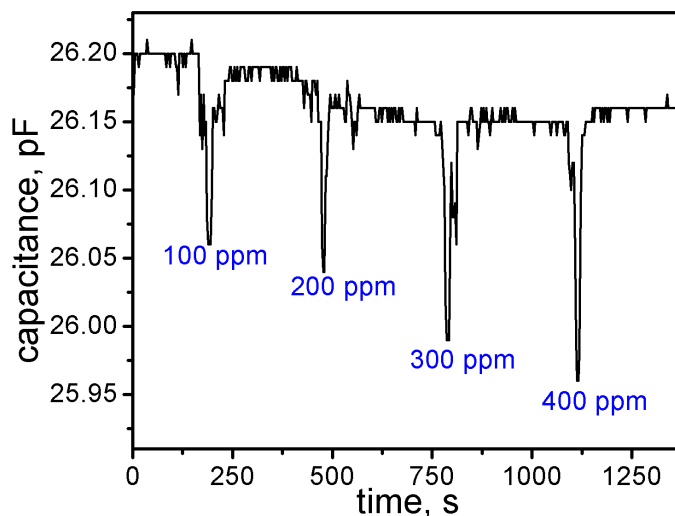


Figure 4.11: Capacitive response of the sensor upon exposure to 100, 200, 300, 400 ppm xylene concentrations.

further optimization our sensor platform is expected to exhibit better performance than existing technologies.

4.6 Conclusions

A new approach to the fabrication of an electrical sensor for organic vapor detection employing an ultrathin flexible pnc-Si membrane as a porous electrode was demonstrated. Using a porous electrode simplifies the fabrication of conventional capacitive parallel-plate sensors traditionally constructed with etch-through electrodes. The mechanical strength and elasticity of pnc-Si were tested and no measurable plastic deformation was observed. Devices were built and successfully operated in solvent vapor environments. The swelling caused by vapor permeation was measured by optical profilometry. Reversible real-time capacitance response of the sensor was obtained for three solvents that use different mechanisms for capacitance changes, as well as for different concentrations of the same vapor.

Chapter 5

Pnc-Si Membrane in Low Voltage Electroosmosis

Electroosmotic (EO) pumps are used in a variety of microfluidics applications which include drug delivery and biomedical applications [122], fuel cells [14, 123], microelectronics cooling, and biological and chemical analysis [124]. The applied voltage used in EO pumping ranges from a few volts to kilovolts. Such a high voltage is required since in most of the EO pumps, the electrodes are placed within the fluid, which increases the distance between electrodes and, therefore, the resistance. A significant reduction in the applied voltage, while keeping the same high electric field required for pumping, can be achieved by reducing the spacing between electrodes. In principle, the electrode spacing can be reduced to the thickness of the pnc-Si membrane (15-30 nm) by developing a technique for depositing isolated metal electrodes on both sides of this porous material.

This chapter is organized as follows. The theoretical background behind electroosmotic pumping and a review of the existing devices are presented in Section 5.1. The method used for depositing metal electrodes on the pnc-Si membrane, as well as the fabrication of the pnc-Si based EO pump, are described in detail in Section 5.2. The experimental setup used to measure the flow rate of the pnc-Si based EO pump and the preliminary performance evaluation are discussed in Sections 5.4 and 5.3. The chapter is concluded in Section 5.5.

5.1 Background of Electroosmotic Pumps

The origins of the electrokinetic transport and the principle of the electroosmotic pumping are presented in Section 5.1.1. The existing electroosmotic pumps and their key performance requirements are reviewed in Section 5.1.2.

5.1.1 Fundamentals of Electroosmotic Flow

Most materials acquire a surface charge when brought into contact with an aqueous solution. The origins of this charge include ionization of surface groups (deprotonation or protonation), specific ion adsorption, or charged crystal surface [125, 126]. The surface groups ionization in oxides results in negatively or positively charged surfaces depending on pH levels. The surface of silicon dioxide (SiO_2) is terminated

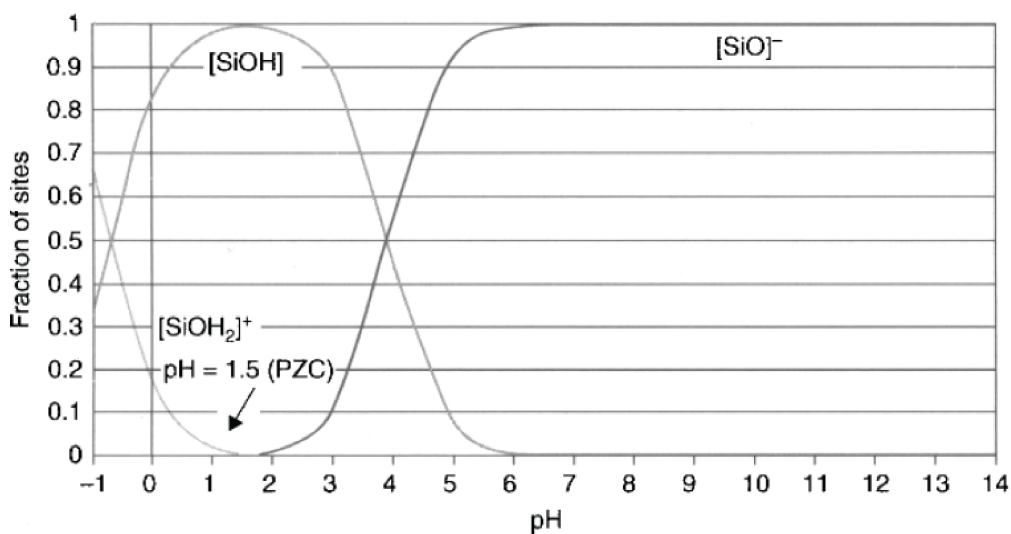


Figure 5.1: Fraction of positive, negative and neutral sites on SiO_2 surface in water at different pH values [127].

with silanol groups (SiOH), and is negatively charged at neutral pH due to their deprotonation (SiO^-). At very low pH values, the SiO_2 surface charge due to silanol protonation (SiOH_2^+) becomes positive, and is equal to zero at $\text{pH}=1.5$. The pH value at which the surface charge is equal to zero due to suppression of the surface ionization is called the point of zero charge (PZC). Figure 5.1 shows the fraction of positive, negative and neutral sites on SiO_2 surface in water at different pH values [127].

The charged surface influences the distribution of the nearby ions in the aqueous solution. Ions of the opposite polarity are attracted to the surface to balance the charge on the charged surface, and ions of the same polarity are repelled. The liquid layer with balancing counterions and the charged surface form an electrical double

layer (EDL) [10]. The layer of strongly attracted ions close to the surface is called the Stern layer (or Helmholtz layer) and is immobilized near the charged surface. The thickness of the Stern layer is dictated by the size of the ions and is several Å. The layer between the Stern layer and the bulk liquid is called the diffuse layer, and in this layer ions are less effected by electrostatic interaction with the charged surface and are mobile. The ion concentration near the charged surface in the diffuse layer obeys the Boltzmann distribution. The thickness of this layer depends on the electrolyte concentration and can be predicted by the Debye length λ_D in electrolytes [125]

$$\lambda_D = \sqrt{\frac{\epsilon k_B T}{2e^2 z^2 n_\infty}}, \quad (5.1)$$

where ϵ is dielectric permittivity of the solvent, k_B is the Boltzmann constant, T is the temperature, e is electron charge, z is the valence and n_∞ is the bulk concentration of the ions. As an example, the values of the Debye length λ_D for 10 mM, 100 μ M and 1 μ M electrolyte concentrations for $z = 1$ are 3, 30 and 300 nm respectively [10, 126]. The diffuse layer is responsible for the electrokinetic phenomena.

The ion distribution in EDL can be described by an electrokinetic potential ψ , which exponentially decreases away from the surface to the bulk fluid. The EDL structure and potential distribution are illustrated in Figure 5.2 [10]. The electrokinetic potential ψ at the shear plane, which is the boundary between the Stern and diffuse layers, is called the zeta potential ζ . The zeta potential ζ is used instead of

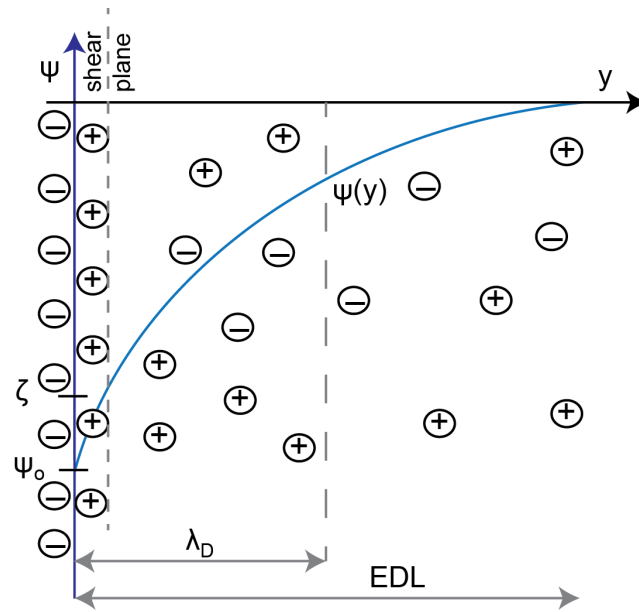


Figure 5.2: Schematic of the electrical double layer (EDL) formed by a negatively charged surface and electrokinetic potential ψ distribution. ψ_0 is surface potential, ζ is zeta potential, y is distance from the surface, λ_D is the Debye length.

the wall potential ψ_0 to describe electrokinetic phenomena and can be on the order of 50 mV. Zeta potential is a property of the interface between the solid and solution.

Electrokinetic effects are based on the presence of the electric double layer (EDL) and include electroosmosis, electrophoresis, streaming potential and sedimentation potential. Electroosmotic flow (EO) is the movement of the electrolyte solution relative to the charged surface due to a tangentially applied electric field. When a tangential electric field is applied, the mobile ions in the diffuse layer migrate towards the oppositely charged electrode, dragging the viscous liquid with them. The velocity profile of the EO flow in a channel is uniformly flat as shown in Figure 5.3, which is a major advantage over the pressure-driven flow [128].

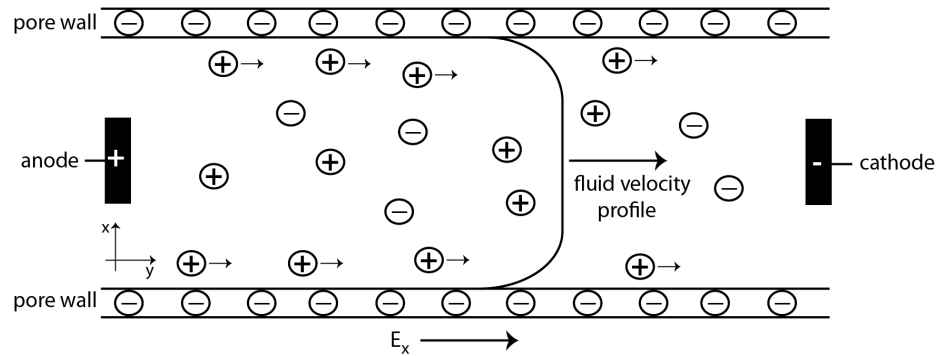


Figure 5.3: Velocity profile of the electroosmotic flow in a channel with negatively charged surface.

The EO flow velocity under the influence of the applied electric field E is given by the Helmholtz-Smoluchowski relation:

$$\nu = -\frac{\zeta \varepsilon}{\mu} E, \quad (5.2)$$

where $\varepsilon = \varepsilon_0 \varepsilon_r$ is the permittivity of the solution, μ is its viscosity, and ζ is the zeta potential [10, 125]. The minus sign indicates the flow direction and is due to the ζ potential. After being negatively charged by deprotonation, the SiO_2 surface ($\zeta < 0$) attracts positive ions, and this results in a positively charged EDL and causes EO flow towards the negative electrode. Equation 5.2 shows that the EO flow velocity is linearly proportional to the applied electric field strength and zeta potential.

5.1.2 Electroosmotic Pumps

Various types of micropumps have been designed for use in microfluidic devices to precisely control the liquid flow from one part of the device to the other. Complex devices require multiple pumps and other microfluidic components to operate simultaneously, and it is for this reason that pumps must be easy to fabricate and integrate into the system. Micropumps are typically classified into mechanical and non-mechanical. Mechanical pumps usually contain moving parts to perform pumping, and include electrostatic, piezoelectric, electromagnetic and other types. Non-mechanical pumps control liquids by converting non-mechanical energy (electrical or magnetic) into the kinetic energy of the fluid. These include electrohydrodynamic (EHD), magnetohydrodynamic (MHD), electroosmotic (EO), electrowetting, electrochemical and other types of non-mechanical micropumps [14, 15]. The only disadvantage of non-mechanical pumps versus mechanical pumps at the microscale is that non-mechanical pumps can operate with a limited variety of fluid. The type of liquid (low conductivity, high conductivity, with magnetic particles, etc.) depends on the pumping mechanism, while mechanical pumps can pump all types of liquids. In most cases, the non-mechanical pumps are preferred due to the absence of moving mechanical parts and their compact size.

The most popular non-mechanical micropumps are electroosmotic (EO) pumps, which employ electric field-induced drag forces generated by mobile ions in EDL as

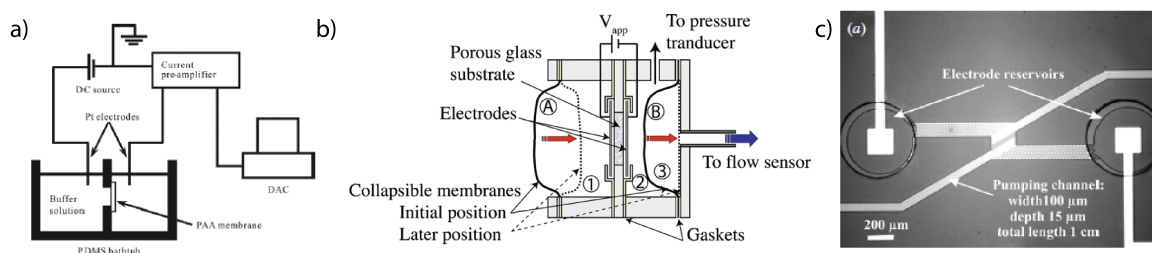


Figure 5.4: Examples of pump geometries: a) porous anodic alumina membrane pump [129]; b) pump based on porous glass substrate composed of silica and borosilicate particles [130]; c) microfabricated pump [131].

the driving pumping mechanism. Conventional EO pumps consist of a porous substrate or planar microchannels sealed between reservoirs with liquid, two electrodes inserted in reservoirs and a power source. The electrodes create an electric field that influences mobile ions in the EDL, and thus moves the liquid from one side of the porous substrate to the other. The porous materials used for EO pump fabrication include porous silicon [132], porous polymeric membranes [133], carbon nanotube based membranes [134, 135], silica particles [130], and anodized alumina (AAO) membranes [129, 136, 137, 138, 139]. Planar pumps are fabricated using standard semiconductor fabrication and chemical etching techniques [140]. Examples of pump geometries are shown in Figure 5.4. The key features that influence the performance of the EO pump are the magnitude of the applied electric field, the microchannel dimensions, the microchannel surface charge and the ionic concentration of the liquid [14, 124]. High flow rates and low applied voltage are a key performance requirements for an efficiently operating EO pump.

5.2 Pnc-Si Membranes as Electroosmotic Pumps

A major shortcoming of currently available EO pumps is that achieving sufficient flow rates requires high operating voltages (10-10000 V), which are not compatible with integrated microfluidic devices and prevent easy device handling [141, 142]. By reducing the spacing between the electrodes, the same electric field strength can be achieved at lower voltage. One approach for achieving this reduction is to use thin porous membranes (10-100 μm) as substrate materials in EO pumps [136, 129, 132]. In conventionally designed EO pumps, metal wire or mesh electrodes are placed in reservoirs at distances ranging from a few millimeters to a few centimeters from the porous material. Such an electrode placement introduces a significant resistive component from the solution and thus fluid pumping requires higher voltages (20-100 V). To further reduce the voltage, electrodes can be coated on both surfaces of the porous membrane [137, 138]. The best example of this idea involves 50 nm thin platinum electrodes sputtered on a 60 μm thick AAO membrane which achieved 1-5 V operating voltages with a maximum flow rate of 0.074 ml/min-V-cm² [139].

Depositing electrodes on the opposite sides of an ultrathin pnc-Si membrane would reduce the spacing between electrodes by several orders of magnitude compared to all existing EO pumps. If the spacing between electrodes is equal to the thickness of the pnc-Si membrane (15-30 nm), a field as high as 3-7 MV/m can be generated using only 100 mV. A schematic of the EO pump using metallized pnc-Si as a substrate

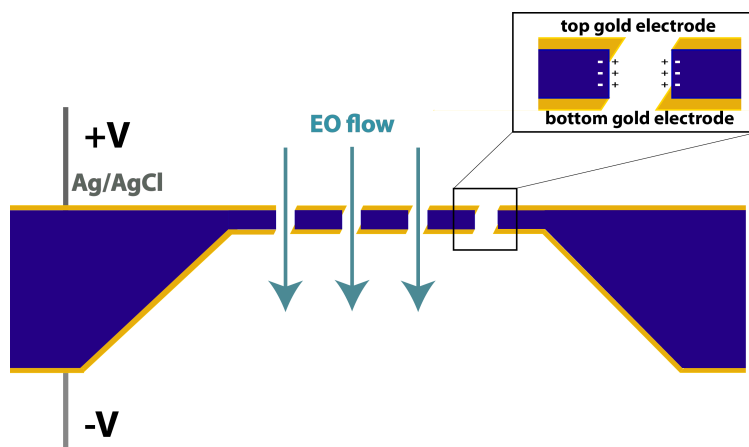


Figure 5.5: Schematic of the pnc-Si membrane based electroosmotic pump.

membrane material is given in Figure 5.5. The main fabrication challenge for the pnc-Si EO pump is developing a metallization process that creates electrically isolated electrodes across the porous ultrathin membrane.

5.2.1 Pnc-Si Electrodes Fabrication by Glancing Angle Deposition

A procedure for pnc-Si metallization using e-beam evaporation is described in detail in Sections 2.4 and 4.2.1. Since the material deposition during evaporation happens in the line of sight, shadowing can occur due to the substrate surface geometry and the placement of the substrate relative to the source. The shadowing effect results in a nonuniform film thickness, undesirable morphology, step coverage and void formation, and is usually problematic for microfabrication. This effect is minimized by heating the substrate to enhance surface diffusion, and by rotating it to

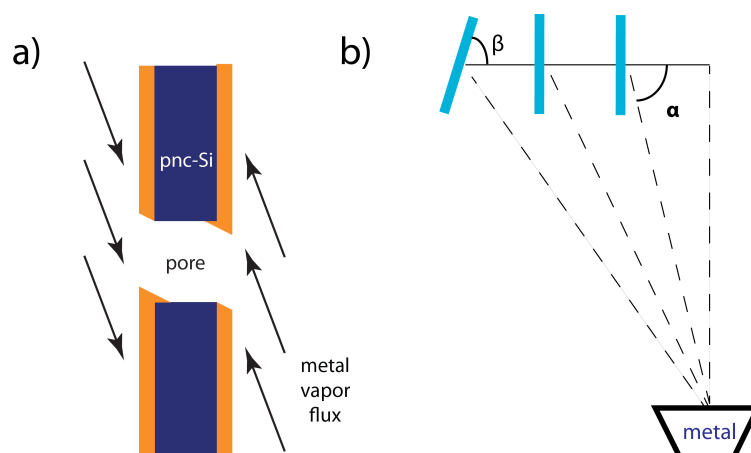


Figure 5.6: a) Schematic of the glancing angle deposition technique showing the partial pnc-Si pore coverage due to directional metal vapor flux; b) wafer positioning during glancing angle deposition.

reduce shadowing and to create a layer of uniform thickness. In contrast, the nonuniform distribution of the vapor incident particles can be used as a control in thin film deposition. The technique known as glancing angle deposition (GLAD) employs oblique angle deposition and substrate motion, and is primarily used for sculpturing thin films [143, 144]. In this technique, the substrate on which the thin film is deposited is positioned at an oblique angle to the incident vapor, which is close to a 90° angle to the normal of the substrate.

The directional nature of the evaporation is used to deposit isolated electrodes on different sides of the pnc-Si membrane. By controlling the orientation of the membrane relative to the impinging metal vapor flux, the amount of metal penetration inside the pores can be controlled. By positioning the stationary pnc-Si membrane at a glancing angle relative to the metal source, a metal layer is deposited only on

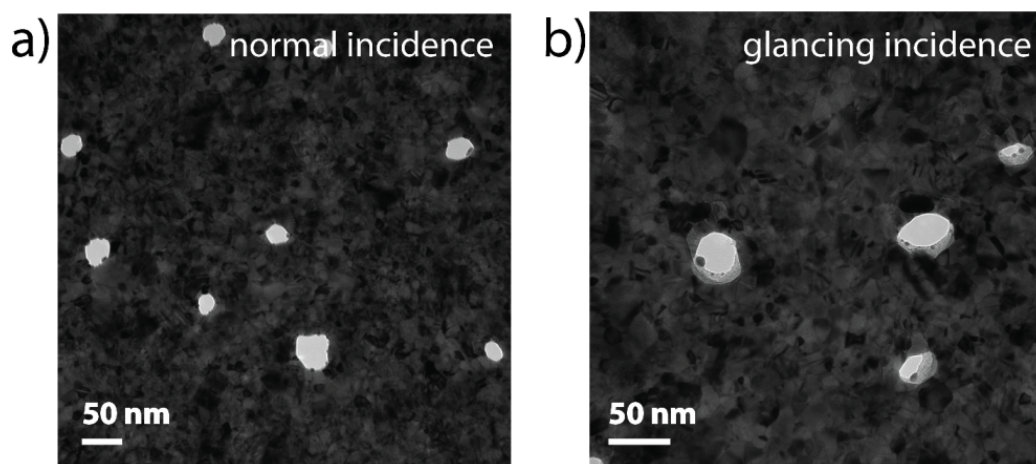


Figure 5.7: TEM images of pnc-Si with gold deposited on one side at: a) normal incidence and b) glancing incidence. The metal film deposited at the normal incidence conformally coats the pores, as seen in TEM image of (a). The gold film deposited at glancing incidence coats only one side of the pores as seen in TEM image of (b).

the membrane surface and, as a result of shadowing, on the side of the pores facing the vapor flux. This evaporation process is schematically illustrated in Figure 5.6(a). By rotating the membrane chip after the first deposition, the second metal layer is deposited on the back of the membrane and the opposite wall of the pore as shown.

To evaporate thin gold films and a titanium adhesion layer on the pnc-Si membrane at glancing incidence, the chips are positioned in the chamber at varying angles α and β relative to the position of the crucible containing gold as shown in Figure 5.6(b). TEM images of the pnc-Si with metal deposited on one side at normal incidence and at glancing incidence are compared in Figure 5.7.

5.2.2 Optimization of Electrode Deposition Parameters

The gold electrodes deposited on the pnc-Si membrane must be thin enough to keep the pores open, and yet thick enough to ensure good conductivity. The parameters can be optimized by choosing the appropriate deposition conditions, including the deposition angles α and β (Figure 5.6(b)) and the film thickness that yields a continuous layer.

Material evaporation is carried out at low pressure so that the vapor transport from the source to the wafer is free molecular, meaning that the vapor particles are traveling in straight lines to the wafer. The material sources can be classified as point or surface sources, as illustrated in Figure 5.8. The sources used in the evaporation method are considered surface sources, except when the deposition occurs at a high rate. In this case, a virtual point source can be created directly above the crucible due to the high vapor pressure, which creates viscous flow regime conditions [59].

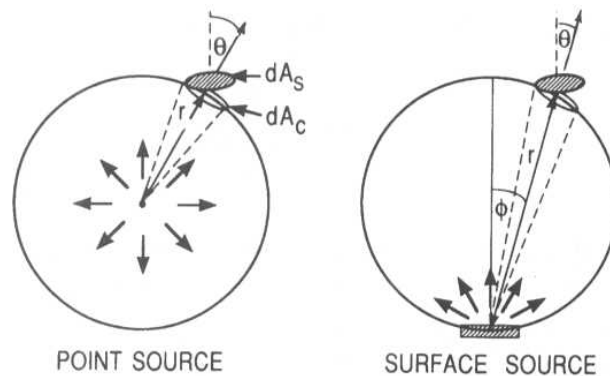


Figure 5.8: Schematic of material evaporation from point source and surface source [59].

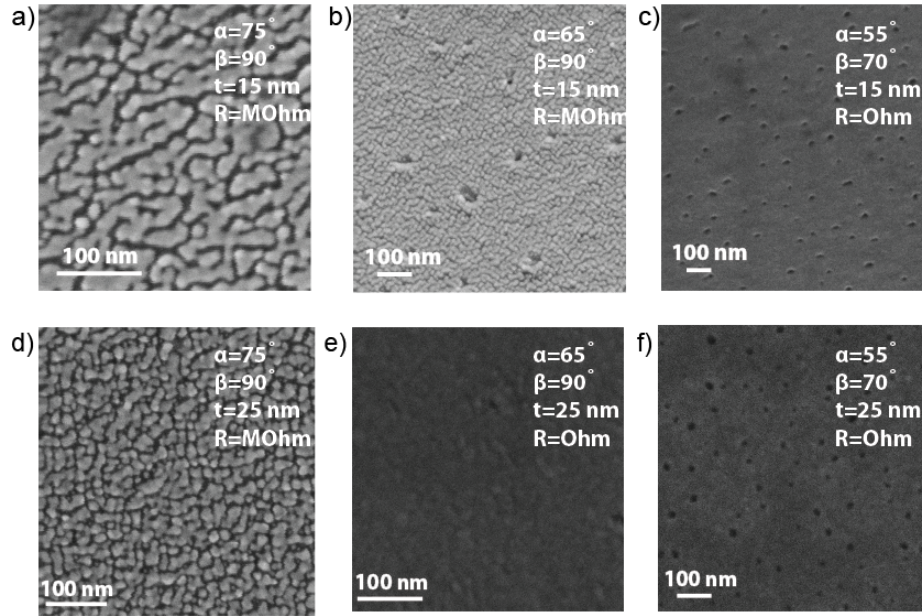


Figure 5.9: SEM images of the 15 nm and 25 nm metal films deposited on 30 nm thick pnc-Si membrane at different angles α and β . The corresponding angles, metal film thickness t and measured resistance R magnitude are inserted in the images.

The thickness distribution of the evaporated films from the surface source reflects the angular dependence of the vapor flux according to the cosine distribution law. The material mass deposited per unit area of the wafer is

$$\frac{dM_s}{dA_s} = \frac{M_e \cos\phi \cos\theta}{\pi r^2}, \quad (5.3)$$

where dM_s is mass deposited on the substrate area dA_s , M_e is total evaporated mass, and r is the distance between the wafer and source surfaces. The emission angle θ and the receiving angle ϕ are the angles between r and the surface normals of the source surface and the wafer surface, as defined in Figure 5.8 [59, 145].

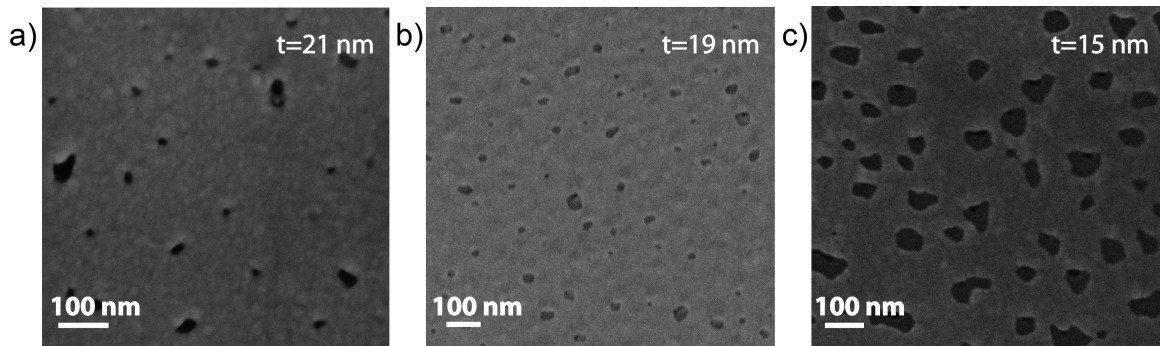


Figure 5.10: SEM images of gold films of different thicknesses deposited on 30 nm thick pnc-Si membrane at $\alpha=65^\circ$ and $\beta=90^\circ$: a) 21 nm; b) 19 nm; c) 15 nm. Some of the dark areas in (b) and (c) are bare pnc-Si membrane areas with pores, which are not covered with metal.

Gold films with a titanium adhesion layer (3 nm) of total thicknesses 15 nm and 25 nm were deposited on 30 nm thick pnc-Si membrane chips at three different positions as shown in Figure 5.6. Gold and titanium are deposited in the same run without breaking the vacuum. The chip placement is defined by the following angles α and β : 1) $\alpha=75^\circ$, $\beta=90^\circ$; 2) $\alpha=65^\circ$, $\beta=90^\circ$; 3) $\alpha=55^\circ$, $\beta=70^\circ$. The corresponding SEM images of the deposited films are illustrated in Figure 5.9. The thinner films and the films metallized at higher angles α are granular and discontinuous, because there is not enough material to form a continuous film. The resistance of the deposited metal films was measured by a two-point probe method, and ranges from several Ohms to MOhms.

To determine the thickness of the conductive metal electrode that minimizes the pore clogging, gold films of different thicknesses (21 nm, 19 nm, and 15 nm) were deposited at $\alpha=65^\circ$ and $\beta=90^\circ$. SEM images of these films are shown in Figure 5.10.

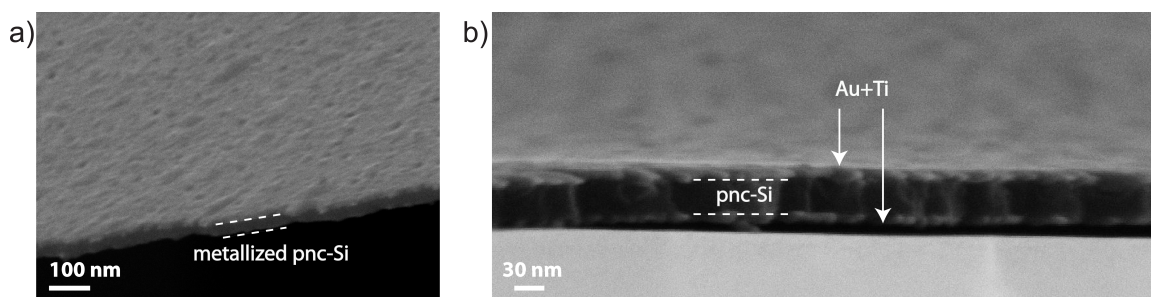


Figure 5.11: Cross-sectional SEM images of the 30 nm thick pnc-Si with metal layers deposited at the glancing angle on both sides.

The measured resistances of these films are on the order of a few Ohms. The discrepancy between 15 nm films in Figure 5.9(b) and Figure 5.10(c) is due to different base pressures during evaporation. The optimal thickness of the gold/titanium bilayer film is 15-17 nm.

The 13-15 nm thick backside metal electrode is deposited on the pnc-Si membrane at $\alpha=55^\circ$ and $\beta=70^\circ$ to overcome shadowing introduced by the silicon well on the backside of the chip. Also, a shadow mask with holes slightly smaller than the dimensions of the membrane chips was placed in front of the samples during backside deposition. This was done to prevent metal deposition of the silicon chip edges, which would short the top and the bottom metal layers. The measured resistance of the bottom electrodes is a few Ohms.

The cross-sectional SEM images in Figure 5.11 confirm that gold electrodes deposited on the pnc-Si at the optimal conditions are separated. Resistances measured between the top and bottom electrodes deposited on the pnc-Si membrane at these

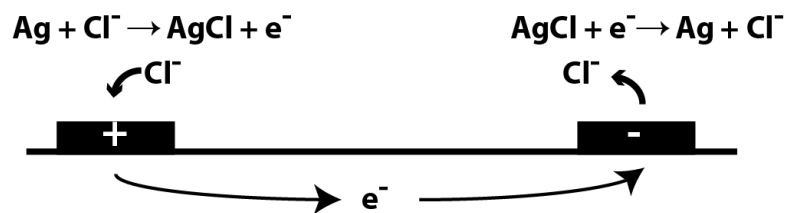


Figure 5.12: Charge transfer reactions occurring at silver-silver chloride electrodes.

conditions range from 0.4 to 10 kOhm and correspond to calculated resistivity values for pnc-Si on the order of 10^6 - 10^7 Ohm-cm. These resistivities are similar to the values measured for nanocrystalline silicon films [146, 147, 148].

5.2.3 Silver-Silver Chloride Electrodes

To maintain the electrical field in the solution and achieve continuous pumping, an electrochemical reaction at the electrodes of the EO pump is essential. Without the charge transfer reactions the electrodes in the ionic solution will act as charged plates of a capacitor and this will result in no flow. In aqueous solutions, electrode potentials higher than 1.2 V cause electrolysis of water leading to the formation of H_2 and O_2 bubbles [149]. Most electrodes are made of platinum or gold, and the charge transfer reaction with the lowest potential that occurs at these electrodes is the electrolysis of water. The formation of bubbles requires special attention and introduces limitations when designing a pump. Changing the chemical composition of the electrolyte, using polymer electrodes and other methods of suppressing and reducing bubble formation during electrolysis have been extensively studied [150, 151, 152].

Silver-silver chloride (Ag/AgCl) electrodes avoid gas formation by inducing an electrochemical reaction at voltages lower than the water electrolysis voltage. The electrochemical reactions responsible for the charge transfer across the interface between metal and solution transform silver into silver chloride and back, and require approximately 0.2 V (Figure 5.12) [149]. The special features of the Ag/AgCl electrodes include consumption of the coated AgCl layer during reactions, and presence of chlorine ions in the solution required for these reactions. Ag/AgCl electrodes are well understood and have been used as reference electrodes in chemical and biological measurements [128].

Following the deposition of gold electrodes on the pnc-Si membrane, silver wires were connected to the top and the bottom gold electrodes (or silicon surface in some cases explained later in the chapter) by a conductive silver epoxy obtained from MG Chemicals. The epoxy was air dried for 24 hours. Silver chloride ink was used to create silver chloride layer on the silver electrodes. The ink was dried in the oven at 80 °C for 15-20 minutes.

5.3 Volumetric Flow Rate Measurement Setup

The experimental setup to test the performance of the pnc-Si based EO pump is illustrated in Figure 5.13. In these experiments, the change of the liquid droplet volume on the front side of the membrane due to EO pumping from/into the liquid

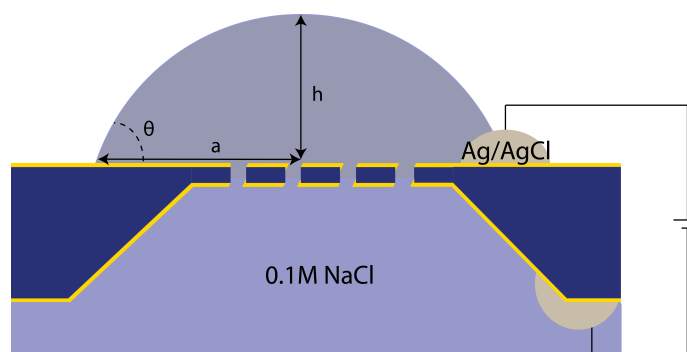


Figure 5.13: Schematic of the experimental setup used to test pnc-Si EO pump.

reservoir on the other side of membrane was observed. The edges of the chip were sealed into a square (2 cm x 2 cm) 300 μm thick silicone gasket cut out of the silicone sheet with an opening for the chip. Before the sealing, the silicone and pnc-Si (as-prepared or metallized) surfaces were treated in oxygen plasma to increase the adhesion strength as described in Section 4.2.2 [153]. Ag/AgCl electrodes were attached after the chips were sealed into silicone. The prepared pnc-Si chip was placed on top of the container with a 0.1 M NaCl aqueous solution in order to ensure that the backside of the membrane and the bottom Ag/AgCl electrode are immersed in liquid. A droplet of NaCl with a volume of 1-5 μl , placed on top of the floating sample, partially covered the pnc-Si membrane slits and top Ag/AgCl electrode. The droplet volume change due to EO is observed with a microscope when a voltage is applied. A DC voltage of 0.2-2 V was applied using an Agilent Function / Arbitrary Waveform Generator. The current was measured by an Agilent 34410A digital multimeter. The lower voltages (0.05-0.15 mV) were applied to the membrane using a voltage divider

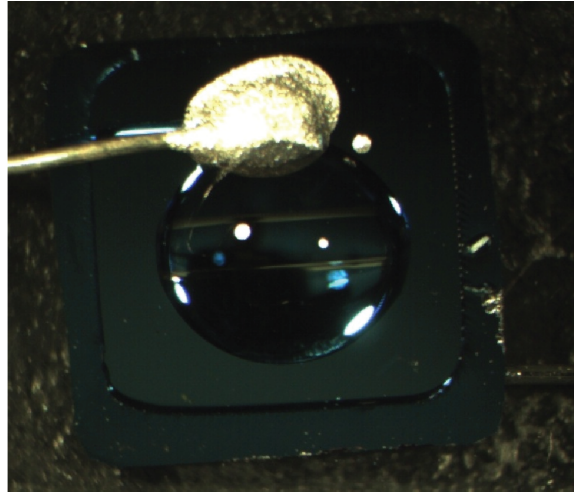


Figure 5.14: Image of the NaCl solution droplet on top of the bare pnc-Si membrane pump with attached Ag/AgCl electrodes. The silicone seal can be seen around the edges of the pnc-Si membrane.

circuit with resistors 10 MOhm and 4.5 MOhm, and an input voltage of 1-2 V.

The droplet forms a spherical cap and its volume is expressed as a function of the radius of the contact area a and the contact angle θ (Figure 5.13) [154]

$$V = \frac{\pi a^3}{3} \frac{(2 + \cos\theta)(1 - \cos\theta)^3}{\sin^3\theta}. \quad (5.4)$$

A camera installed above the sample (topview) was used to monitor droplet volume changes as the voltage was applied. The electrode polarity was alternated and the droplet volume was observed to increase or decrease in response. Digital images extracted from the video data at different times during pumping were analyzed and the radius a changes were extracted with the aid of ImageJ software [155]. Under the assumption of a constant contact angle θ , the volume change was determined

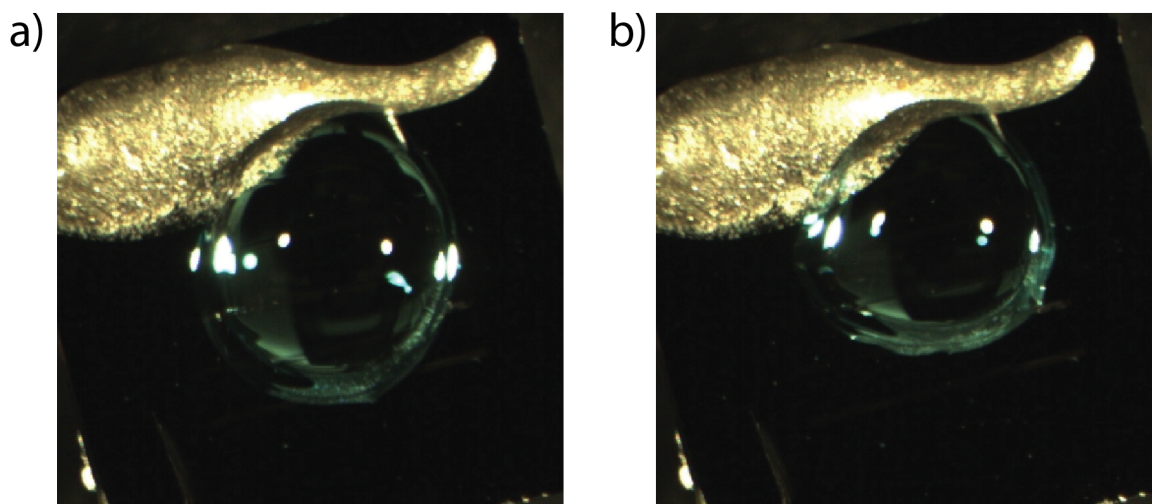


Figure 5.15: Images of the NaCl solution droplet on top of the metallized with gold on both sides pnc-Si membrane pump with attached Ag/AgCl electrodes: a) before pumping; b) after pumping.

using Equation 5.4 and the known droplet volume before the pumping. Examples of the droplets on a non-metallized pnc-Si pump and a pnc-Si pump metallized at glancing incidence are illustrated in Figures 5.14 and 5.15. The volumetric flow rate was calculated as the change in the droplet volume per pumping time.

After several pumping cycles we noticed the discoloration of the metallized surfaces, and suspected deposition of silver chloride ink and silver epoxy constituents. However, an energy-dispersive X-ray spectroscopy (EDS) analysis of these surfaces did not reveal silver or other unexpected material present.

To eliminate the possible influence of contact angle changes on the flow calculation due to discoloration mentioned above, a second method to calculate the volume was used. An additional sideview camera was added to monitor the droplet changes during

pumping [137]. In order to avoid obscuring the camera view by the container walls, the NaCl solution droplet was placed on the bottom of the sample instead of placing the whole sample into the container. The images taken from the side and the top of the droplet on the top surface of the pnc-Si were used to extract the height h and radius a before and after voltage application. Assuming a perfect spherical cap, the volume of the droplet was then calculated using the following equation

$$V = \frac{\pi h}{6}(3a^2 + h^2). \quad (5.5)$$

The side view images of the droplet height change are shown in the Figure 5.16.

The calculated volumetric flow rates are in good agreement for both calculation methods using Equations 5.4 and 5.5 for 2-3 pumping cycles before the surface discoloration occurred.

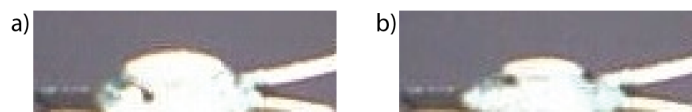


Figure 5.16: Side view images of the NaCl droplet on a metallized pnc-Si pump before (a) and after (b) pumping, showing the droplet height change.

5.4 Pnc-Si EO Pump Performance Evaluation

Previously, a pnc-Si membrane based pump with platinum and silver-silver chloride wire electrodes inserted in solution on different sides of the membrane was studied. The flow rate achieved with 15 nm thick as-prepared pnc-Si membrane was 8 $\mu\text{l}/\text{min}$ at applied voltage 20 V using Pt electrodes, and 0.6 $\mu\text{l}/\text{min}$ at 1 V using Ag/AgCl wire electrodes [156, 157]. The power consumption of these pumps is 20 mW and 0.3 mW, respectively, which is much higher than the amount needed for an ultrathin pump operation. Most of the power in their designs is dissipated by the resistance associated with the electrode to pump spacing [156, 157]. Reducing this spacing is expected to drastically decrease power consumption.

The performance of EO pumps built on pnc-Si membranes with electrodes directly deposited on the surfaces was tested for electrode placed on bare pnc-Si membranes, pnc-Si membranes with only top surface covered with gold, and pnc-Si membranes with both surfaces covered with gold. Each pump has Ag/AgCl electrodes attached to the back and the front surfaces as shown in the Figure 5.17. Ag/AgCl electrodes are attached to the silicon surfaces in Figure 5.17(a), to the top gold layer and the bottom silicon surface in Figure 5.17(b) and (d), to the top and the bottom gold surfaces in Figure 5.17(c). The pnc-Si membranes used in these experiments are 30 nm thick with an initial porosity of 7.4 % and total active area 1.5 mm². The porosity of the pnc-Si pumps with one gold deposited layer is 0.4 %, and with two gold layers is 0.1

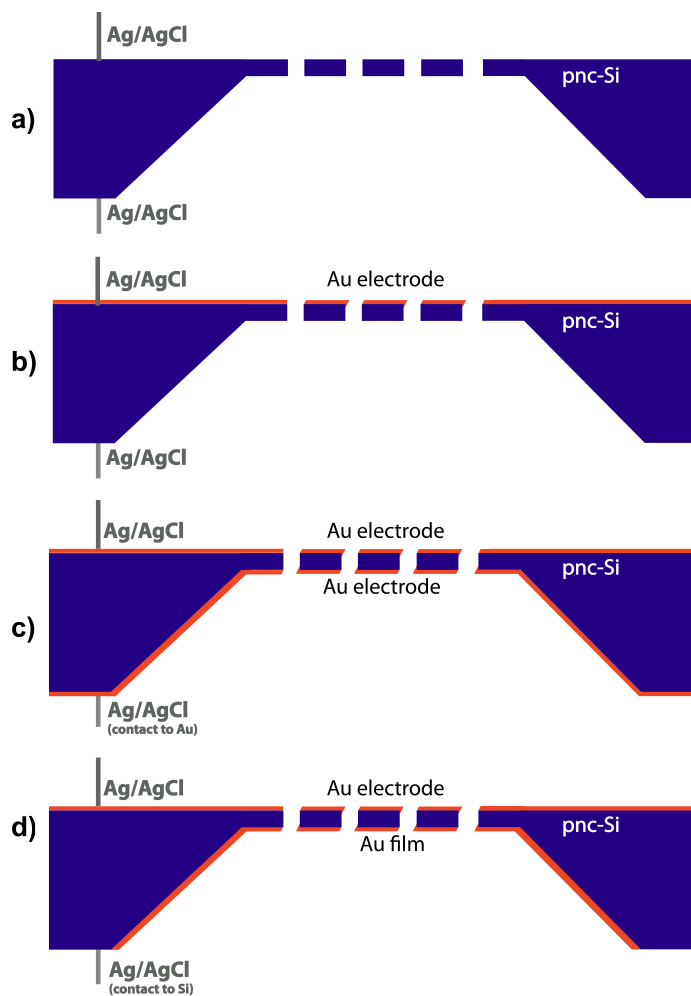


Figure 5.17: Four types of EO pumps built on as-prepared and metallized pnc-Si membranes: a) bare pnc-Si membrane, Ag/AgCl electrodes attached to silicon surfaces; b) pnc-Si with top surface covered with gold, Ag/AgCl electrodes attached to gold and bottom silicon surface; c) both pnc-Si membrane surfaces covered with gold, Ag/AgCl electrodes attached to gold surfaces; d) both pnc-Si membrane surfaces covered with gold, Ag/AgCl electrodes attached to the top gold and bottom silicon surface.

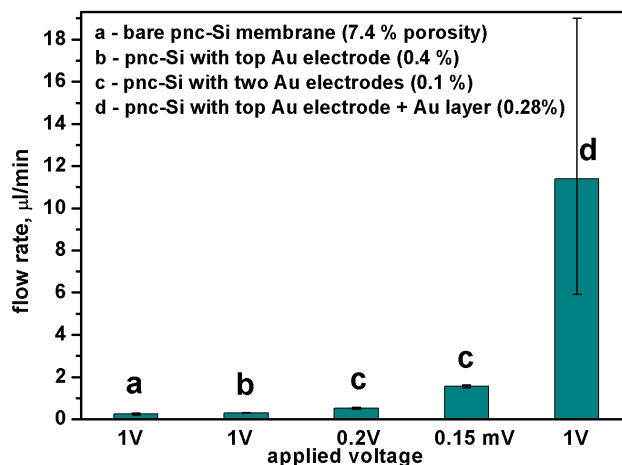


Figure 5.18: Average volumetric flow rates of different pnc-Si EO pumps at different voltages. The samples include a bare pnc-Si membrane, a pnc-Si membrane with only the top surface metallized with gold and a pnc-Si membrane with both surfaces metallized with gold. Each of the pumps has Ag/AgCl electrodes attached to both sides as shown in Figure 5.17. The error bars indicate the maximum and minimum values measured.

or 0.28 %. The decrease in porosity compared to as-prepared membrane is a result of the deposition at glancing incidence.

Volumetric flow rates measured at different voltages for these four pump types are presented in the Figure 5.18. To allow for easier comparison, the average measured flow rates were normalized by porosity and these normalized values are shown in Figure 5.19. The flow rate of the non-metallized pnc-Si pump with Ag/AgCl electrodes attached to it is comparable the flow rate of previously measured pnc-Si pump with electrodes inserted in the fluid described above [156, 157]. The performance of the pumps metallized with gold (Figure 5.17(b-d)) is considerably higher than

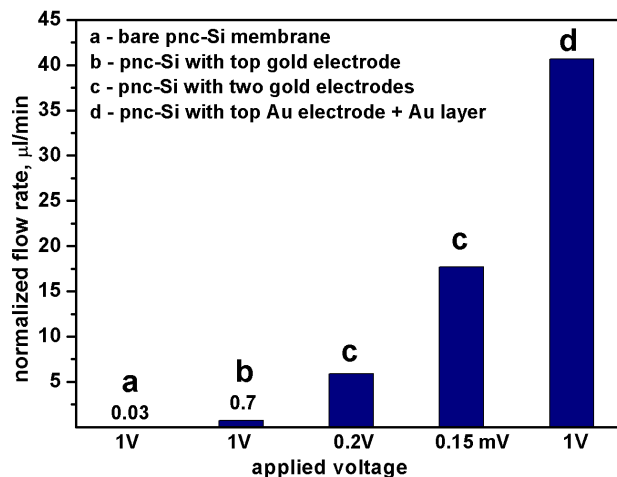


Figure 5.19: Average volumetric flow rates (shown in Figure 5.18) normalized by porosity for different pnc-Si EO pumps at different voltages.

non-metallized. The flow rates of the two double-side metallized pumps are separately discussed below.

The origins of such high flow rates and nonlinearity of the flow with an applied electric field for the pnc-Si pump with voltage applied across gold electrodes (Figure 5.17(c)), are not well understood and need to be further investigated. In classical electroosmosis the flow is a linear function of the applied electric field. The calculated electric field values that correspond to the voltages in Figures 5.18 and 5.19 are approximately on the order of 10^3 V/m for all applied voltages, except 0.2 V when it is on the order of 10^7 V/m. A possible explanation of the low flow rate for the high field strength values is that they are close to the electrical breakdown in aqueous solutions [158]. The breakdown field for deionized water in bulk is 70 MV/m. At micro- and

nanoscale distances the electrical breakdown field of water is not well studied, but strongly depends on the electrode material, electrode geometry, distance between the electrodes, and is considered to be around 10 MV/m [159, 160, 161]. Also, it is possible that the nonlinear electrokinetic phenomena arising from a complicated pnc-Si pore structure after metallization at glancing angles plays a role in the observed high flow rates of these pumps at low applied voltages. The non-uniform electric field inside the pores due to sharp edges, as well as possible concentration polarization effects near the electrodes can result in non-equilibrium electroosmotic flow [162, 163]. The flow rates associated with such phenomena often exceed the classical EO flow rates by a factor of 10-100 for the same electric field strength [164]. Another effect associated with the pump in Figure 5.17(c), which cannot be explained satisfactorily at this moment, is that the applied voltages are lower than required to drive electrochemical reactions on Ag/AgCl electrodes

The highest flow rates are obtained with the pump structure in Figure 5.17(d), that incorporates a non-electrode gold layer on the bottom of the pnc-Si chip. A possible explanation of the high flow rate is that this flow might be due to a combination of two electrokinetic effects - the classical electroosmosis due to the electric field acting on the double layer inside the pores, and induced charge electroosmosis (ICEO). ICEO is a recently discovered phenomena, similar to standard electroosmosis, except that an externally applied electric field acts on its own induced bipolar electrical

double layer at a polarizable electrically conducting surface in the electrolyte solution [165]. ICEO at a non-electrode metal surface has been theoretically predicted and experimentally observed on metal wires and particles in applied field [166]. Standard electroosmotic velocity is linear in the applied field, and ICEO flow velocity has a quadratic dependence of the electric field. ICEO flows can occur at any polarizable surface in the presence DC or AC field (an AC electroosmosis is a subcase of ICEO), and are composed of vortex-like flows [165, 167, 168]. The ICEO flow was shown to combine with the EO flow by introducing gold strips into a dielectric (PDMS, glass) microfluidic channel in DC field for particle manipulation [169, 170], and combining linear electrokinetic effects with ICEO was proposed for pumping and mixing [167].

The measured flow of this pnc-Si pump (Figure 5.17(d)) is higher in one direction (when the liquid volume on top pnc-Si surface increases) than in the other by approximately two orders of magnitude. The higher flow rate is plotted in the Figures 5.18 and 5.19. This asymmetry in flow, which might be attributed to the asymmetrical geometry of the pump structure and the gold layer being on the bottom of it, supports the proposed influence of the ICEO flow during pumping, as it is usually associated with nonuniform surface properties [171, 172]. The only fact that contradicts the ICEO influence, is that ICEO velocity was shown to significantly decrease at ionic concentrations higher than 10 mM, but this effect is not well understood [173].

The power consumption values of the membranes in Figures 5.18 and 5.19 are

approximately 30-300 μW for a , b , c (at 0.2 V) and d pumps, and less than 0.1 nW for the metallized c (at 0.15 mV) pump. This considerable power reduction can be attributed to the fact, that the voltage is applied directly across the 30 nm thickness of the pnc-Si membrane, instead of across 200 μm thick wafer or across the solution millimeters away from the membrane.

5.5 Conclusions

A method, relying on the directional nature of the e-beam evaporation technique, was successfully developed for depositing electrically isolated gold electrodes on different sides of the ultrathin porous membrane. The appropriate deposition parameters that yield a continuous gold film of minimal thickness were determined. Using this glancing angle deposition technique, a pnc-Si membrane based electroosmotic pump was fabricated. It was shown that the pnc-Si membrane based pump can be used to achieve high flow rates when low voltages are applied directly across the membrane. These pumps are characterized by an extremely low power consumption. The results indicate that pnc-Si membranes are promising for the fabrication of effective EO pumps. However, a complete understanding of the pnc-Si pump performance requires further investigation. To the best of our knowledge, our experimental results are the first to put interesting questions related to the pumping mechanisms that arise due to the complicated nanostructure of an ultrathin metallized pump into focus.

Chapter 6

Conclusions and Future Outlook

In this thesis, an ultrathin porous nanocrystalline silicon membrane, fabricated using standard semiconductor techniques, was demonstrated to benefit electrical sensing and nanofluidics applications. In addition, we showed how the membrane can be used as a novel platform to experimentally investigate gas transport phenomena. The molecularly thin nature and unique pore distribution of the membranes were shown to permit the gas flow separation into components based on the interactions of gas molecules with the pore wall surface, and demonstrated the flow enhancement resulted from the change in the nature of these interactions. We also integrated the pnc-Si membrane into a capacitive sensor for organic vapor detection, which allowed fast vapor permeation to the underlying sensing layer and significantly simplified the conventional sensor geometry. A novel method developed for fabricating electrodes directly on pnc-Si enabled the fabrication of an ultrathin electroosmotic pump which was demonstrated to operate under low applied voltages. In future work, we feel

confident that pnc-Si will continue to be an interesting tool for both fundamental research and specific nanoscale device applications.

6.1 Gas Flow through Carbonized Pnc-Si Membranes

In Chapter 3, the gas flow enhancement in carbonized pnc-Si membranes due to the change in the nature of molecule-pore wall interactions was demonstrated. Future studies of this effect will help to bring to light more specific details about the influence of the material structure on the gas flow. It was previously shown in our research group, that high temperature carbonization of the pnc-Si membranes prior coated with aluminum oxide using atomic layer deposition leads to the formation of ordered carbon layers [53]. This ordering happens inside the pores at a much smaller carbon thickness than during carbonization without alumina. Such membranes can be used to investigate the influence of the degree of crystallinity of the carbon layer on the gas flow since their average pore sizes are comparable to untreated pnc-Si.

6.2 Pnc-Si Based Capacitive Sensor Performance

The results described in Section 4 demonstrated the advantages of using pnc-Si as a permeable plate in a capacitive sensor for chemical sensing applications. Further

characterization of the sensor performance can improve this work. Specifically, such important characteristics as the response and recovery times, and their dependency on the average pore diameter in the pnc-Si membrane, and polymer thickness influence on the sensor sensitivity need to be addressed. The sensor geometry can be optimized, as higher active area and porosity of the pnc-Si membrane in the sensor will further improve its characteristics. Additionally, pnc-Si membrane can be used to fabricate a flow-through capacitive sensor using two membranes as permeable plates of the capacitor. Since membrane and sensor fabrication are compatible with standard microfabrication processes, there is the potential for an entire detection system to ultimately be integrated on a single silicon chip.

6.3 Pnc-Si Electroosmotic Pump Optimization

In the Chapter 5, we have shown that efficient EO pumps can be built using the pnc-Si membrane and that they exhibit a major advantage over other pumps because of their extreme thinness. Our work also provided the insight into challenges in building pnc-Si pumps that have to be overcome.

Two directions for further research of the ultrathin metallized pnc-Si EO pumps should be explored. First, the deposition method for fabricating isolated electrodes on the pnc-Si membrane, relying on the directional nature of the evaporation technique, can be further improved to minimize pore clogging. To do this, the quantification

of the pore diameter reduction as a function of initial pore diameter and evaporated metal thickness at different glancing angles needs to be performed. Also, a modification of the deposition technique described in this thesis, that relies on the smaller amounts of metal being deposited on the pore walls than on the pnc-Si surface during deposition at normal incidence, can be explored for electrodes deposition. By optimizing the metal thickness and its evaporation rate, the minimal metal thickness that yields a conductive layer on the pnc-Si surface and results in a non-conductive discontinuous metal layer inside pores, can be found [18].

The second direction for the future research on this topic is to study the pumping mechanisms behind the pump with such a complicated nanostructure. This could be undertaken with a series of flow measurements at various applied voltages for different pump geometries.

Finally, the technique employed for isolated electrodes deposition and the pump structure can be envisioned to study the electrical breakdown of liquids in nanogaps.

Bibliography

- [1] S. P. Adiga, *et al.*, “Nanoporous membranes for medical and biological applications,” *Wiley Interdiscip. Rev. Nanomed. Nanobiotechnol.*, Vol. 1, p. 568, 2009.
- [2] C. J. M. van Rijn, *Nano and micro engineered membrane technology*. Membrane Science and Technology Series, 10, Elsevier, The Netherlands, 2004.
- [3] <http://www.sterlitech.com>.
- [4] A. Belwalkar, *et al.*, “Effect of processing parameters on pore structure and thickness of anodic aluminum oxide (AAO) tubular membranes,” *J. Membr. Sci.*, Vol. 319, p. 192, 2008.
- [5] B. Hinds, *et al.*, “Aligned multiwalled carbon nanotube membranes,” *Science*, Vol. 303, p. 62, 2004.
- [6] H. Tong, *et al.*, “Silicon nitride nanosieve membrane,” *Nano Lett.*, Vol. 4, p. 283, 2004.
- [7] S. Unnikrishnan, *et al.*, “Transition flow through an ultra-thin nanosieve,” *Nanotechnology*, Vol. 20, p. 305304, 2009.
- [8] A. den Berg and M. Wessling, “Silicon for the Perfect Membrane,” *Nature*, Vol. 445, p. 15, 2007.
- [9] C. Striemer, T. Gaborski, J. McGrath, and P. Fauchet, “Charge- and size-based separation of macromolecules using ultrathin silicon membranes,” *Nature*, Vol. 445, p. 749, 2007.
- [10] G. Karniadakis, A. Beskok, and N. Aluru, *Microflows and Nanoflows: Fundamentals and Simulation*. Springer, New York, 2005.

- [11] M. Whitby and N. Quirke, "Fluid flow in carbon nanotubes and nanopipes," *Nat. Nanotechnol.*, Vol. 2, p. 87, 2007.
- [12] M. N. Kavalenka, *et al.*, "Chemical capacitive sensing using ultrathin flexible nanoporous electrodes," *Sens. Actuators, B*, Vol. 162, p. 22, 2012.
- [13] O. Krushinitskaya, T. I. Tonnessen, H. Jakobsen, and E. A. Johannessen, "Characterization of nanoporous membranes for implementation in an osmotic glucose sensor based on the concanavalin Adextran affinity assay," *Adv. Colloid Interface Sci.*, Vol. 376, p. 153, 2011.
- [14] A. Nisar, N. Afzulpurkar, B. Mahaisavariya, and A. Tuantranont, "MEMS-based micropumps in drug delivery and biomedical applications," *Microfluid Nanofluid*, Vol. 130, p. 917, 2008.
- [15] X. Wang, C. Cheng, S. Wang, and S. Liu, "Electroosmotic pumps and their applications in microfluidic systems," *Microfluid Nanofluid*, Vol. 6, p. 145, 2009.
- [16] S.-W. Nam, M. J. Rooks, K.-B. Kim, and S. M. Rossnagel, "Ionic field effect transistors with sub-10 nm multiple nanopores," *Nano Lett.*, Vol. 9, p. 2044, 2009.
- [17] E. C. Yusko, *et al.*, "Controlling protein translocation through nanopores with bio-inspired fluid walls," *Nat. Nanotechnol.*, Vol. 6, p. 253, 2011.
- [18] R. Wei, *et al.*, "Fabrication of metallized nanopores in silicon nitride membranes for single-molecule sensing," *Small*, Vol. 6, p. 1406, 2010.
- [19] A. Singer, *et al.*, "Nanopore based sequence specific detection of duplex DNA for genomic profiling," *Nano Lett.*, Vol. 10, p. 738, 2010.
- [20] M. S. Sander and L.-S. Tan, "Nanoparticle arrays on surfaces fabricated using anodic alumina films as templates," *Adv. Func. Mat*, Vol. 13, p. 393, 2003.
- [21] A. Saxena, B. P. Tripathi, M. Kumar, and V. K. Shahi, "Membrane-based techniques for the separation and purification of proteins: An overview," *Adv. Colloid Interface Sci.*, Vol. 145, p. 1, 2009.

- [22] R. J. Gilbert, *et al.*, “Computational and functional evaluation of a microfluidic blood flow device,” *ASAIIO J.*, Vol. 53, p. 447, 2007.
- [23] W. H. Fissell, *et al.*, “High-performance silicon nanopore hemofiltration membranes,” *J. Membr. Sci.*, Vol. 1, p. 58, 2009.
- [24] A. C. Attaluri, *et al.*, “Evaluation of nano-porous alumina membranes for hemodialysis application,” *ASAIIO J.*, Vol. 55, p. 217, 2009.
- [25] S. P. Nunes and K.-V. Peinemann, *Membrane Technology in Chemical Industry*. Wiley-VCH, Weinheim, 2006.
- [26] P. Y. Apel and S. N. Dmitriev, “Micro- and nanoporous materials produced using accelerated heavy ion beams,” *Adv. Nat. Sci.: Nanosci. Nanotechnol.*, Vol. 2, p. 013002, 2011.
- [27] <http://www.whatman.com/TrackEtchedPolycarbonateandPolyesterMembranes.aspx>.
- [28] I. Vlassiuk, *et al.*, “Versatile ultrathin nanoporous silicon nitride membranes,” *PNAS*, Vol. 106, p. 21039, 2009.
- [29] K. Schwirn, *et al.*, “Self-Ordered Anodic Aluminum Oxide Formed by H₂SO₄ Hard Anodization,” *ACS Nano*, Vol. 2, p. 302, 2008.
- [30] H. U. Osmanbeyoglu, T. Hur, and H. K. Kim, “Thin alumina nanoporous membranes for similar size biomolecule separation,” *J. of Membr. Sci.*, Vol. 343, p. 1, 2009.
- [31] J. Holt, *et al.*, “Fast mass transport through sub2-nanometer carbon nanotubes,” *Science*, Vol. 312, p. 1034, 2006.
- [32] M. Yu, H. Funke, J. Falconer, and R. Noble, “High density, vertically-aligned carbon nanotube membranes,” *Nano Lett.*, Vol. 9, p. 225, 2009.
- [33] S. Iijima, “Helical microtubules of graphitic carbon,” *Nature*, Vol. 354, p. 56, 1991.

- [34] S. Kim, *et al.*, “Scalable fabrication of carbon nanotube/polymer nanocomposite membranes for high flux gas transport,” *Nano Lett.*, Vol. 7, p. 2806, 2008.
- [35] A. J. Storm, *et al.*, “Fabrication of solid-state nanopores with single-nanometre precision,” *Nat. Mat.*, Vol. 2, p. 537, 2003.
- [36] D. Krapf, *et al.*, “Fabrication and characterization of nanopore-based electrodes with radii down to 2 nm,” *Nano Lett.*, Vol. 6, p. 105, 2006.
- [37] T. R. Gaborski, *et al.*, “High-performance separation of nanoparticles with ultrathin porous nanocrystalline silicon membranes,” *ACS Nano*, Vol. 4, p. 6973, 2010.
- [38] J. L. Snyder, *et al.*, “An experimental and theoretical analysis of molecular separations by diffusion through ultrathin nanoporous membranes,” *J. of Membr. Sci.*, Vol. 369, p. 119, 2010.
- [39] M. N. Kavalenka, *et al.*, “Hybrid polymer/ultrathin porous nanocrystalline silicon membranes system for flow-through chemical vapor and gas detection,” *Active polymers, Mater. Res. Soc. Symp. Proc., San Francisco, CA, 2009*, Vol. 1190, 2009.
- [40] A. A. Agrawal, *et al.*, “Porous nanocrystalline silicon membranes as highly permeable and molecularly thin substrates for cell culture,” *Biomaterials*, Vol. 31, p. 5408, 2010.
- [41] M. N. Kavalenka, *et al.*, “Ballistic and Non-ballistic Flow through Ultrathin Nanopores,” *Nanotechnology*, Vol. 23, p. 145706, 2012.
- [42] D. Z. Fang, *et al.*, “Methods for controlling the pore properties of ultra-thin nanocrystalline silicon membranes,” *J. Phys.: Condens. Matter*, Vol. 22, p. 454134, 2010.
- [43] H. Geng, *Semiconductor manufacturing handbook*. The McGraw-Hill, 2005.
- [44] <http://www.directvacuum.com/sputter.asp>.
- [45] J. W. Gardner, V. K. Varadan, and O. O. Awadelkarim, *Microsensors, MEMs and smart devices*. Wiley, England, 2001.

- [46] M. J. Madou, *Fundamentals of microfabrication: the science of miniaturization*. CRC Press, 2002.
- [47] Z. Ma, *et al.*, "Very high surface area microporous carbon with a three-dimensional nano-array structure: synthesis and its molecular structure," *Chem. Mater.*, Vol. 13, p. 4413, 2001.
- [48] S. Miller, V. Young, and C. Martin, "Electroosmotic flow in template-prepared carbon nanotube membranes," *J. Am. Chem. Soc.*, Vol. 123, p. 12335, 2001.
- [49] G. Che, B. Lakshmi, E. Fisher, and C. Martin, "Carbon nanotubule membranes for electrochemical energy storage and production," *Nature*, Vol. 393, p. 346, 1998.
- [50] G. Che, *et al.*, "Carbon nanotubule membranes for electrochemical energy storage and production," *Chem. Mater.*, Vol. 10, p. 260, 1998.
- [51] D. Mattia, *et al.*, "Effect of graphitization on the wettability and electrical conductivity of CVD-carbon nanotubes and films," *J. Phys. Chem. B*, Vol. 110, p. 9850, 2006.
- [52] D. Z. Fang, *et al.*, "Pore size control of ultrathin silicon membranes by rapid thermal carbonization," *Nano Lett.*, Vol. 10, p. 3904, 2010.
- [53] D. Z. Fang, *Fabrication, Characterization, and Functionalization of Porous Nanocrystalline Silicon Membranes*, PhD Thesis, 2010.
- [54] A. A. Elshabini-Riad and F. D. Barlow, *Thin Film Technology Handbook*. McGraw-Hill, 1997.
- [55] L. Reimer and H. Kohl, *Transmission electron microscopy*. Springer, New York, 2008.
- [56] W. Osten, *Optical inspection of microsystems*. CRC Press, 2007.
- [57] MATLAB code available for download at <http://www.nanomembranes.org/software.html>.

- [58] S. Dushman and J. Lafferty, *Scientific Foundations of Vacuum Technique*. Wiley, New York, 1962.
- [59] M. Ohring, *Materials Science of Thin Films: Deposition and Structure*. Academic Press, 2001.
- [60] M. Elwenspoek and H. Jansen, *Silicon Micromachining*. Cambridge University Press, 1998.
- [61] W. Steckelmacher, “Knudsen flow 75 years on: the current state of the art for flow of rarefied gases in tubes and systems,” *Rep. Prog. Phys.*, Vol. 49, p. 1083, 1986.
- [62] P. Clausing, “The flow of highly rarefied gases through tubes of arbitrary length,” *Ann. Phys.*, Vol. 12, p. 961, 1932.
- [63] J. Helmer, “Applications of an approximation to molecular flow in cylindrical tubes,” *J. Vacuum Sci. Technol.*, Vol. 4, p. 179, 1967.
- [64] M. Knudsen, “The laws of molecular flow and of inner friction flow of gases through tubes,” *Ann. Phys.*, Vol. 28, p. 75, 1909.
- [65] R. Feres and G. Yablonsky, “Knudsen’s cosine law and random billiards,” *Chem. Eng. Sci.*, Vol. 59, p. 1541, 2004.
- [66] J. C. Maxwell, “On Stress in Rarified Gases Arising from Inequalities of Temperature,” *Philos. Trans. R. Soc.*, Vol. 170, p. 231, 1879.
- [67] S. Albo, L. Broadbelt, and R. Snurr, “Transmission probabilities and particle-wall contact for Knudsen diffusion in pores of variable diameter,” *AIChE J.*, Vol. 11, p. 3679, 2006.
- [68] S. Bhatia, H. Chen, and D.S.Sholl, “Comparisons of diffusive and viscous contributions to transport coefficients of light gases in single-walled carbon nanotubes,” *Molecular Simulation*, Vol. 9, p. 643, 2005.
- [69] V. Sokhan and N. Quirke, “Slip coefficient in nanoscale pore flow,” *Phys. Rev. E*, Vol. 78, p. 01530, 2008.

- [70] G. Arya, H.-C. Chang, and E. Maginn, "Molecular simulations of Knudsen wall-slip: effect of wall morphology," *Mol. Simulat.*, Vol. 29, p. 697, 2003.
- [71] A. Agrawal and S. V. Prabhu, "Survey on measurement of tangential momentum accommodation coefficient," *J. Vac. Sci. Technol.*, Vol. 26, p. 634, 2008.
- [72] E. B. Arkilic, K. S. Breuer, and M. A. Schmidt, "Mass flow and tangential momentum accommodation in silicon micromachined channels," *J. Fluid Mech.*, Vol. 437, p. 29, 2001.
- [73] T. Graham, "On the motion of gases," *Phil. Trans. R. Soc. Lond.*, Vol. 136, p. 573, 1846.
- [74] S. Gruener and P. Huber, "Knudsen Diffusion in Silicon Nanochannels," *Phys. Rev. Lett.*, Vol. 100, p. 064502, 2008.
- [75] M. Savard, C. Tremblay-Darveau, and G. Gervais, "Flow conductance of a single nanohole," *Phys. Rev. Lett.*, Vol. 103, p. 104502, 2009.
- [76] A. Skoulidas, D. Ackerman, J. Johnson, and D. Sholl, "Rapid transport of gases in carbon nanotubes," *Phys. Rev. Lett.*, Vol. 89, p. 185901, 2002.
- [77] H. Chen and D. Sholl, "Predictions of selectivity and flux for CH_4/H_2 separations using single walled carbon nanotubes as membranes," *J. Membr. Sci.*, Vol. 269, p. 152, 2006.
- [78] V. Sokhan, D. Nicholson, and N. Quirke, "Fluid flow in nanopores: accurate boundary conditions for carbon nanotubes," *J. Chem. Phys.*, Vol. 117, p. 8531, 2002.
- [79] S. Cooper, B. Cruden, and M. Meyyappan, "Gas transport characteristics through a carbon nanotubule," *Nano Lett.*, Vol. 4, p. 377, 2004.
- [80] A. Noy, *et al.*, "Nanofluidics in carbon nanotubes," *Nano today*, Vol. 2, p. 22, 2007.
- [81] H. Verweij, M. Schillo, and J. Li, "Fast mass transport through carbon nanotube membranes," *Small*, Vol. 3, p. 1996, 2007.

- [82] C. Martin, M. Nishizawa, K. Jirage, and M. Kang, "Investigations of the transport properties of gold Nanotubule membranes," *J. Phys. Chem. B*, Vol. 105, p. 1925, 2001.
- [83] X. Pages, *et al.*, "Gas permeation of PECVD membranes inside alumina substrate tubes," *Sep. and Purif. Tech.*, Vol. 25, p. 399, 2001.
- [84] D. M. Ruthven, W. J. DeSisto, and S. Higgins, "Diffusion through porous media: ultrafiltration, membrane permeation and molecular sieving," *Chem. Eng. Sci.*, Vol. 64, p. 3201, 2009.
- [85] C. Leger, H. D. L. Lira, and R. Paterson, "Preparation and properties of surface modified ceramic membranes. Part III. Gas permeation of 5 nm alumina membranes modified by trichloro-octadecylsilane," *J. Membr. Sci.*, Vol. 120, p. 135, 1996.
- [86] G. Levi, M. Simon, and J. Helmer, "Use of the Clausing's equation to evaluate the pumping action of molecular Gaede pumps," *Vacuum*, Vol. 46, p. 357, 1995.
- [87] E. Dovgolevsky, U. Tisch, and H. Haick, "Chemically sensitive resistors based on monolayer-capped cubic nanoparticles: towards configurable nanoporous sensors," *Small*, Vol. 5, p. 1158, 2009.
- [88] A. Tricoli and S. Pratsinis, "Dispersed nanoelectrode devices," *Nat. Nanotechnol.*, Vol. 5, p. 54, 2010.
- [89] Y. Lin, F. Lu, Y. Tu, and Z. Ren, "Glucose biosensors based on carbon nanotube nanoelectrode ensembles," *Nano Lett.*, Vol. 4, p. 190, 2004.
- [90] T. Kang, *et al.*, "Ultra-thin and conductive nanomembrane arrays for nanomechanical transducers," *Adv. Mater.*, Vol. 20, p. 3131, 2008.
- [91] G. S. Attard, *et al.*, "Mesoporous Platinum Films from Lyotropic Liquid Crystalline Phases," *Science*, Vol. 278, p. 838, 1997.
- [92] D. W. Arrigan, "Nanoelectrodes, nanoelectrode arrays and their applications," *Analyst*, Vol. 129, p. 1157, 2004.
- [93] C. Dekker, "Solid-state nanopores," *Nat. Nanotechnol.*, Vol. 2, p. 209, 2007.

- [94] R. Smeets, *et al.*, "Translocation of RecA-coated double-stranded DNA through solid-state nanopores," *Nano Lett.*, Vol. 9, p. 3089, 2009.
- [95] R. F. Taylor and J. S. Schultz, *Handbook of chemical and biological sensors*. IOP Publishing Ltd., 1996.
- [96] S. Patel, *et al.*, "Chemicapacitive microsensors for volatile organic compound detection," *Sens. Actuators, B*, Vol. 96, p. 541, 2003.
- [97] S. Satyanarayana, D. McCormick, and A. Majumdar, "Parylene micro membrane capacitive sensor array for chemical and biological sensing," *Sens. Actuators, B*, Vol. 115, p. 494, 2006.
- [98] K. Park, *et al.*, "Capacitive micromachined ultrasonic transducers for chemical detection in nitrogen," *Appl. Phys. Lett.*, Vol. 91, p. 094102, 2007.
- [99] J. Li, J. Xu, M. Zhang, and M. Rong, "Carbon black/polystyrene composites as candidates for gas sensing materials," *Carbon*, Vol. 41, p. 2353, 2003.
- [100] J. Adams, *et al.*, "Nanowatt chemical vapor detection with a self-sensing, piezoelectric microcantilever array," *Appl. Phys. Lett.*, Vol. 83, p. 3428, 2003.
- [101] M. Kitsara, *et al.*, "Single chip interdigitated electrode capacitive chemical sensor arrays," *Sens. Actuators, B*, Vol. 127, p. 186, 2007.
- [102] A. Kummer, A. Hierlemann, and H. Baltes, "Tuning Sensitivity and Selectivity of Complementary Metal Oxide Semiconductor-Based Capacitive Chemical Microsensors," *Anal. Chem.*, Vol. 76, p. 2470, 2004.
- [103] B. Adhikari and S. Majumdar, "Polymers in Sensor Applications," *Prog. Polym. Sci.*, Vol. 29, p. 699, 2004.
- [104] M. C. Stuart, *et al.*, "Emerging applications of stimuli-responsive polymer materials," *Nat. Mat.*, Vol. 9, p. 101, 2010.
- [105] Y. Osada and D. E. DeRossi, *Polymer sensors and actuators*. Springer, New York, 1999.

- [106] J. W. Grate, S. N. Kaganove, and V. R. Bhethanabotla, "Examination of mass and modulus contributions to thickness shear mode and surface acoustic wave vapour sensor responses using partition coefficients," *Faraday Discuss.*, Vol. 107, p. 259, 1997.
- [107] R. W. Baker, *Membrane technology and applications*. McGraw Hill, 2000.
- [108] T. E. Mlsna, *et al.*, "Chemicapacitive microsensors for chemical warfare agent and toxic industrial chemical detection," *Sens. Actuators, B*, Vol. 116, p. 192, 2006.
- [109] S.-J. Park and M.-K. Seo, *Interface science and composites*. Elsevier, 2011.
- [110] J. N. Lee, C. Park, and G. M. Whitesides, "Solvent compatibility of polydimethylsiloxane-based microfluidic devices," *An. Chem.*, Vol. 75, p. 6544, 2003.
- [111] S. Patel, S. Hobson, S. Cemalovic, and T. Mlsna, "Detection of methyl salicylate using polymer-filled chemicapacitors," *Talanta*, Vol. 76, p. 872, 2008.
- [112] D. McCorkle, *et al.*, "Ethanol vapor detection in aqueous environments using micro-capacitors and dielectric polymers," *Sens. Actuators, B*, Vol. 107, p. 892, 2005.
- [113] A. Hierlemann, *et al.*, "Application-specific sensor systems based on CMOS chemical microsensors," *Sens. Actuators, B*, Vol. 70, p. 2, 2000.
- [114] A. Hierlemann, *et al.*, "Application-specific sensor systems based on CMOS chemical microsensors," *Sens. Actuators, B*, Vol. 70, p. 2, 1995.
- [115] K. E. Herold and A. Rasooly, *Lab on a Chip technology: Biomolecular separation and analysis*. Caister Academic Press, 2009.
- [116] Y. F. L. P. Lee, D. Psaltis, and C. Yang, *Optofluidics: fundamentals, devices, and applications*. McGraw-Hill, 2010.
- [117] K. Yu and Y. Han, "A stable PEO-tethered PDMS surface having controllable wetting property by a swelling-deswelling process," *Soft Matter*, Vol. 2, p. 705, 2006.

- [118] M. J. Demkowicz and A. S. Argon, "High-density liquid-like component facilitates plastic flow in a model amorphous silicon system," *Phys. Rev. Lett.*, Vol. 93, p. 025505, 2004.
- [119] M. J. Demkowicz, A. S. Argon, D. Farkas, and M. Frary, "Simulation of plasticity in nanocrystalline silicon," *Phil. Magazine*, Vol. 87, p. 4253, 2007.
- [120] D. R. Lide, *CRC handbook of chemistry and physics, ed.48*. Taylor and Francis, Boca Raton, FL, 2006.
- [121] E. Dickey, *et al.*, "Room Temperature Ammonia and Humidity Sensing Using Highly Ordered Nanoporous Alumina Films," *Sensors*, Vol. 2, p. 91, 2002.
- [122] W. Shin, *et al.*, "A miniature, single use, skin-adhered, low-voltage, electroosmotic pumping-based subcutaneous infusion system," *Drug Deliv. and Transl. Res.*, Vol. 1, p. 342, 2011.
- [123] S. Litster, C. R. Buie, and J. G. Santiago, "Engineering model for coupling wicks and electroosmotic pumps with proton exchange membrane fuel cells for active water management," *Electrochimica Acta*, Vol. 54, p. 6223, 2009.
- [124] D. J. Laser and J. G. Santiago, "A review of micropumps," *J. Micromech. Microeng.*, Vol. 14, p. R35, 2004.
- [125] D. Li, *Electrokinetics in Microfluidics*. Elsevier, The Netherlands, 2004.
- [126] J. H. Masliyah and S. Bhattacharjee, *Electrokinetic and colloid transport phenomena*. Wiley and Sons, Inc, 2006.
- [127] K. A. Reinhardt and R. F. Reidy, *Handbook for cleaning for semiconductor manufacturing: Fundamentals and Applications*. Wiley and Sons, Inc, 2011.
- [128] A. J. Bard and L. R. Faulkner, *Electrochemical Methods: Fundamentals and Applications*. Wiley and Sons, Inc, 2001.
- [129] S. K. Vajandar, *et al.*, "SiO₂-coated porous anodic alumina membranes for high flow rate electroosmotic pumping," *Nanotechnology*, Vol. 18, p. 275705, 2007.

- [130] S. Litster, M. E. Suss, and J. G. Santiago, "A two-liquid electroosmotic pump using low applied voltage and power," *Sens. Actuators, A*, Vol. 163, p. 311, 2010.
- [131] K. Seibel, L. Scholer, H. Schafer, and M. Bohm, "A programmable planar electroosmotic micropump for lab-on-a-chip applications," *J. Micromech. Microeng.*, Vol. 18, p. 025008, 2008.
- [132] S. Yao, *et al.*, "Electroosmotic pumps fabricated from porous silicon membranes," *J. Microelectromech. Syst.*, Vol. 15, p. 717, 2006.
- [133] C. Wang, L. Wang, and J. Xue, "Low-voltage electroosmotic pumping using polyethylene terephthalate track-etched membrane," *Nucl. Instr. Meth. B*, p. in press, 2012.
- [134] S. A. Miller and C. R. Martin, "Redox modulation of electroosmotic flow in a carbon nanotube membrane," *J. Am. Chem. Soc.*, Vol. 126, p. 6226, 2004.
- [135] J. Wu, *et al.*, "Highly efficient electroosmotic flow through functionalized carbon nanotube membranes," *Nanoscale*, Vol. 3, p. 3321, 2011.
- [136] Y.-F. Chen, *et al.*, "Surface modification of nano-porous anodic alumina membranes and its use in electroosmotic flow," *Sens. Actuators, B*, Vol. 145, p. 575, 2010.
- [137] A. Gupta, *et al.*, "Localized, low-voltage electro-osmotic pumping across nanoporous membranes," *Appl. Phys. Lett.*, Vol. 91, p. 094101, 2007.
- [138] J. Miao, *et al.*, "Micropumps based on the enhanced electroosmotic effect of aluminum oxide membranes," *Adv. Mater.*, Vol. 19, p. 4234, 2007.
- [139] Y. Ai, *et al.*, "A low-voltage nano-porous electroosmotic pump," *J. Colloid Interface Sci.*, Vol. 350, p. 465, 2010.
- [140] Y. Takamura, *et al.*, "Low-voltage electroosmosis pump for stand-alone microfluidics devices," *Electrophoresis*, Vol. 24, p. 185, 2003.

- [141] S. L. Zeng, C. H. Chen, J. C. Mikkelsen, and J. G. Santiago, "Fabrication and characterization of electroosmotic micropumps," *Sens. Actuators, B*, Vol. 79, p. 107, 2003.
- [142] D. S. Reichmuth, G. S. Chirica, and B. J. Kirby, "Increasing the performance of high-pressure, high-efficiency electrokinetic micropumps using zwitterionic solute additives," *Sens. Actuators, B*, Vol. 92, p. 37, 2003.
- [143] K. Robbie, J. C. Sit, and M. J. Brett, "Advanced techniques for glancing angle deposition," *J. Vac. Sci. Technol. B*, Vol. 16, p. 1115, 1998.
- [144] R. Messier, V. C. Venugopal, and P. D. Sunal, "Origin and evolution of sculptured thin films," *J. Vac. Sci. Technol. A*, Vol. 18, p. 1538, 2000.
- [145] S. Campbell, *The science and engineering of microelectronic fabrication*. Oxford University Press, Inc., 2001.
- [146] K. D. Sattler, *Handbook of nanophysics: nanoparticles and quantum dots*. CRC Press, 2011.
- [147] T. B. Elliot, *Leading-edge semiconductor research*. Nova Science Publishers, Inc., 2005.
- [148] S. Wagner, H. Gleskova, I.-C. Cheng, and M. Wu, "Silicon for thin-film transistors," *Thin Solid Films*, Vol. 430, p. 15, 2003.
- [149] K. A. D. Guzman, R. N. Karnik, J. S. Newman, and A. Majumdar, "Spatially controlled microfluidics using low-voltage electrokinetics," *J. Microelectromech. Syst.*, Vol. 15, p. 237, 2006.
- [150] M. Moini, P. Cao, and A. J. Bard, "Hydroquinone as a buffer additive for suppression of bubbles formed by electrochemical oxidation of the CE Buffer at the outlet electrode in capillary electrophoresis/electrospray ionization-mass spectrometry," *Anal. Chem.*, Vol. 71, p. 1658, 1999.
- [151] P. Selvaganapathy, Y. L. Ki, P. Renaud, and C. H. Mastrangelo, "Bubble-free electrokinetic pumping," *J. Microelectromech. Syst.*, Vol. 11, p. 448, 2002.

- [152] P. G. Erlandsson and N. D. Robinson, "Electrolysis-reducing electrodes for electrokinetic devices," *Electrophoresis*, Vol. 32, p. 784, 2011.
- [153] H.-L. Gou, J.-J. Xu, X.-H. Xia, and H.-Y. Chen, "Air plasma assisting micro-contact deprinting and printing for gold thin film and PDMS patterns," *ACS Appl. Mater. Interfaces*, Vol. 2, p. 1324, 2010.
- [154] D. Quere, M.-J. Azzopardi, and L. Delattre, "Drops at rest on a tilted plane," *Langmuir*, Vol. 14, p. 2213, 1998.
- [155] <http://rsbweb.nih.gov/ij/>.
- [156] J. L. Snyder, *et al.*, "High performance, low voltage electroosmotic pumps with molecularly thin nanoporous silicon membranes," 2011, PNAS (submitted).
- [157] J. L. Snyder, *Porous Nanocrystalline Silicon Membranes as Sieves and Pumps*, PhD Thesis, 2011.
- [158] S. Yao, *et al.*, "Porous glass electroosmotic pumps: design and experiments," *J. Colloid Interface Sci.*, Vol. 268, p. 143, 2003.
- [159] H. M. Jones and E. E. Kunhardt, "Pulsed dielectric breakdown of pressurized water and salt solutions," *J. Appl. Phys.*, Vol. 77, p. 795, 1995.
- [160] B. D. Storey, L. R. Edwards, M. S. Kilic, and M. Z. Bazant, "Steric effects on ac electro-osmosis in dilute electrolytes," *Phys. Rev. E*, Vol. 77, p. 036317, 2008.
- [161] K. Schoenbach, *et al.*, "Electrical breakdown of water in microgaps," *Plasma Sources Sci. Technol.*, Vol. 17, p. 024010, 2008.
- [162] D. G. Strickland, M. E. Suss, T. A. Zangle, and J. G. Santiago, "Evidence shows concentration polarization and its propagation can be key factors determining electroosmotic pump performance," *Sens. Actuators, B*, Vol. 143, p. 795, 2010.
- [163] J.-Y. Jung, P. Joshi, L. P. T. J. Thornton, and J. D. Posner, "Electromigration current rectification in a cylindrical nanopore due to asymmetric concentration polarization," *Anal. Chem.*, Vol. 81, p. 3128, 2009.

- [164] N. A. Mishchuk, *et al.*, “Microfluidic pump based on the phenomenon of electroosmosis of the second kind,” *Microfluid Nanofluid*, Vol. 11, p. 675, 2011.
- [165] M. Z. Bazant, “Induced-charge electrokinetic phenomena,” *Colloids and Surfaces A: Physicochem. Eng. Aspects*, Vol. 267, p. 122, 2005.
- [166] J. A. Levitan, *et al.*, “Experimental observation of induced-charge electroosmosis around a metal wire in a microchannel,” *Colloids and Surfaces A: Physicochem. Eng. Aspects*, Vol. 267, p. 122, 2005.
- [167] M. Z. Bazant and T. M. Squires, “Induced-charge electrokinetic phenomena: theory and microfluidic applications,” *Phys. Rev. Lett.*, Vol. 92, pp. 066101-1, 2004.
- [168] C. K. Harnett, *et al.*, “Model based design of a microfluidic mixer driven by induced charge electroosmosis,” *Lab Chip*, Vol. 8, p. 565, 2008.
- [169] S. E. Yalcin, *et al.*, “On-demand particle enrichment in a microfluidic channel by a locally controlled floating electrode,” *Sens. Actuators, B*, Vol. 153, p. 277, 2011.
- [170] S. E. Yalcin, *et al.*, “Manipulating particles in microfluidics by floating electrodes,” *Electrophoresis*, Vol. 31, p. 3711, 2010.
- [171] T. M. Squires and M. Z. Bazant, “Breaking symmetries in induced-charge electro-osmosis and electrophoresis,” *J. Fluid Mech.*, Vol. 560, p. 65, 2006.
- [172] H. Sugioka, “Asymmetrical reverse vortex flow due to induced-charge electroosmosis around carbon stacking structures,” *Phys. Rev. E: Stat. Nonlinear Soft Matter Phys.*, Vol. 83, p. 056321, 2011.
- [173] M. Z. Bazant, M. S. Kilic, B. D. Storey, and A. Ajdari, “Towards an understanding of induced-charge electrokinetics at large applied voltages in concentrated solutions,” *Adv. Colloid Interface Sci.*, Vol. 152, p. 48, 2009.